


<b>AD-A242 577</b> 		<b>GE</b>		Form Approved OMB No. 0704-0188	
Public reporting burr gathering and maint. collection of informa Davis Highway, Suite		sponse, including the time for reviewing instructions, searching existing data sources, ormation. Send comments regarding this burden estimate or any other aspect of this uarters Services, Directorate for Information Operations and Reports, 1215 Jefferson idget, Paperwork Reduction Project (0704-0188), Washington, DC 20503.			
<b>1. AGENCY USE</b> 11-14-91		<b>3. REPORT TYPE AND DATES COVERED</b> Annual 10/1/90 - 9/30/91			
<b>4. TITLE AND SUBTITLE</b> Three Dimensional Transient Analysis of Microstrip Microstrip Circuits in Multilayered Anisotropic Media			<b>5. FUNDING NUMBERS</b>		
<b>6. AUTHOR(S)</b> Prof. J.A. Kong			<b>7. PERFORMING ORGANIZATION NAME(S) AND ADDRESS(ES)</b> Research Laboratory of Electronics Massachusetts Institute of Technology 77 Massachusetts Avenue Cambridge, MA 02139		
<b>9. SPONSORING / MONITORING AGENCY NAME(S) AND ADDRESS(ES)</b> Office of Naval Research 800 North Quincy Street Arlington, VA 22217			<b>10. SPONSORING / MONITORING AGENCY REPORT NUMBER</b>		
<b>11. SUPPLEMENTARY NOTES</b> The view, opinions and/or findings contained in this report are those of the author(s) and should not be construed as an official Department of the Army position, policy, or decision, unless so designated by other documentation.					
<b>12a. DISTRIBUTION / AVAILABILITY STATEMENT</b> Approved for public release; distribution unlimited.			<b>12b. DISTRIBUTION CODE</b>		
<b>13. ABSTRACT (Maximum 200 words)</b> Work by Prof. Kong and his collaborators is summarized here					
<b>14. SUBJECT TERMS</b>				<b>15. NUMBER OF PAGES</b>	
				<b>16. PRICE CODE</b>	
<b>17. SECURITY CLASSIFICATION OF REPORT</b> UNCLASSIFIED		<b>18. SECURITY CLASSIFICATION OF THIS PAGE</b> UNCLASSIFIED		<b>19. SECURITY CLASSIFICATION OF ABSTRACT</b> UNCLASSIFIED	
				<b>20. LIMITATION OF ABSTRACT</b> UL	

## **ANNUAL REPORT**

**Title: THREE DIMENSIONAL TRANSIENT ANALYSIS OF MICROSTRIP CIRCUITS IN  
MULTILAYERED ANISOTROPIC MEDIA**

**Sponsor by: Department of the Navy/Office of Naval Research**


**Contract number: N00014-90-J-1002**

**Research Organization: Center for Electromagnetic Theory and Applications  
Research Laboratory of Electronics  
Massachusetts Institute of Technology**

**OSP number: 72943**

**Principal Investigator: J. A. Kong**

**Period covered: October 1, 1990 — September 30, 1991**

**91-15775**  


## Three Dimensional Transient Analysis of Microstrip Circuits in Multilayered Anisotropic Media

Under the sponsorship of the ONR contract N00014-90-J-1002 we have published 9 refereed journal and conference papers.

The coupled-wave theory is generalized to analyze the diffraction of waves by chiral gratings for arbitrary angles of incidence and polarizations. Numerical results for the Stokes parameters of diffracted Floquet modes versus the thickness of chiral gratings with various chiralities are calculated. Both horizontal and vertical incidences are considered for illustration. The diffracted waves from chiral gratings are in general elliptically polarized; and in some particular instances, it is possible for chiral gratings to convert a linearly polarized incident field into two nearly circularly polarized Floquet modes propagating in different directions.

A general spectral domain formulation to the problem of radiation of arbitrary distribution of sources embedded in a horizontally stratified arbitrary magnetized linear plasma is developed. The fields are obtained in terms of electric and magnetic type dyadic Green's functions. The formulation is considerably simplified by using the kDB system of coordinates in conjunction with the Fourier transform. The distributional singular behavior of the various dyadic Green's functions in the source region is investigated and taken into account by extracting the delta function singularities. Finally, the fields in any arbitrary layer are obtained in terms of appropriately defined global upward and downward reflection and transmission matrices.

We investigated a method for the calculation of the current distribution, resistance, and inductance matrices for a system of coupled superconducting transmission lines having finite rectangular cross section. These calculations allow accurate characterization of both

high- $T_c$  and low- $T_c$  superconducting strip transmission lines. For a single stripline geometry with finite ground planes, the current distribution, resistance, inductance, and kinetic inductance are calculated as a function of the penetration depth for various film thickness. These calculations are then used to determine the penetration depth for  $Nb$ ,  $NbN$ , and  $YBa_2Cu_3O_{7-x}$  superconducting thin films from the measured temperature dependence of the resonant frequency of a stripline resonator. The calculations are also used to convert measured temperature dependence of the quality factor to the intrinsic surface resistance as a function of temperature for a  $Nb$  stripline resonator.

The electromagnetic radiation from a VLSI chip package and heatsink structure is analysed by means of the finite-difference time-domain (FD-TD) method. The FD-TD algorithm implemented incorporates a multi-zone gridding scheme to accommodate fine grid cells in the vicinity of the heatsink and package cavity and sparse gridding in the remainder of the computational domain. The issues pertaining to the effects of the heatsink in influencing the overall radiating capacity of the configuration are addressed. Analyses are facilitated by using simplified heatsink models and by using dipole elements as sources of electromagnetic energy to model the VLSI chip. The potential for enhancement of spurious emissions by the heatsink structure is examined. For heatsinks of typical dimensions, resonance is possible within the low gigahertz frequency range.

Because the effects of diffraction during proximity-print x-ray lithography are of critical importance, a number of previous researchers have attempted to calculate the diffraction patterns and minimum achievable feature sizes as a function of wavelength and gap. Work to date has assumed that scalar diffraction theory is applicable—as calculated, for example, by the Rayleigh-Sommerfeld formulation—and that Kirchhoff boundary conditions can be applied. Kirchhoff boundary conditions assume that the fields (amplitude and phase) are constant in the open regions between absorbers, and a different constant in regions just under the absorbers (i.e., that there are no fringing fields). An x-ray absorber

is, however, best described as a lossy dielectric that is tens or hundreds of wavelengths tall, and hence Kirchhoff boundary conditions are unsuitable. We have instead used two numerical techniques to calculate accurate diffracted fields from gold absorbers for two cases: a 30 nm-wide line at  $\lambda = 4.5$  nm, and a 100 nm-wide line at  $\lambda = 1.3$  nm. We show that the use of Kirchhoff boundary conditions introduces unphysically high spatial frequencies into the diffracted fields. The suppression of these frequencies—which occurs naturally without the need to introduce an extended source or broad spectrum—improves exposure latitude for mask features near  $0.1\ \mu\text{m}$  and below.

In order to understand the physical meaning of rational reflection coefficients in one-dimensional inverse scattering theory for optical waveguide design, we have studied the relation between the poles of the transverse reflection coefficient and the modes in inhomogeneous dielectrics. By using a stratified medium model it is shown that these poles of the reflection coefficient have a one-to-one correspondence to the discrete modes, which are the guided and leaky modes. The radiation modes have continuous real values of transverse wave numbers and are not represented by the poles of the reflection coefficient. Based on these results, applications of the Gel'fand-Levitan-Marchenko theory to optical waveguide synthesis with the rational function representation of the transverse reflection coefficient are investigated.

In compact modules of high performance computers, signal transmission lines between integrated circuit chips are embedded in multilayered dielectric medium. These signal lines are usually placed in different layers and run perpendicular to each other. The interaction between the orthogonal crossing lines and the signal line affects its propagation characteristics and may cause considerable signal distortion.

The interaction of a pair of crossing lines in isotropic medium has been studied using a time-domain approach, where coupling is described qualitatively. This method becomes computationally expensive when the number of crossing lines increases. With many identical crossing strips uniformly distributed above the signal line, the transmission properties are characterized by stopbands due to the periodicity of the structure. Periodic structure have been investigated using frequency-domain methods. Periodically nonuniform microstrip lines in an enclosure are analyzed on the basis of a numerical field calculation. A technique based on the network-analytical formulism of electromagnetic fields has been used to analyze striplines and finlines with periodic stubs. The propagation characteristics of waves along a periodic array of parallel signal lines in a multilayered isotropic structure in the presence of a periodically perforated ground plane and that in a mesh-plane environment have been studied. More recently, the effect of the geometrical properties on the propagation characteristics of strip lines with periodic crossing strips embedded in a shielded one-layer isotropic medium have been investigated. Both open and closed multilayered uniaxially anisotropic structures are considered. A full-wave analysis is used to study the propagation characteristics of a microstrip line in the presence of crossing strips. The signal line and the crossing strips are assumed to be located in two arbitrary layers of a stratified uniaxially anisotropic medium. An integral equation formulation using dyadic Green's functions in the periodically loaded structure is derived. Galerkin's method is then used to obtain the eigenvalue equation for the propagation constant. The effects of anisotropy on the stopband properties are investigated. Numerical results for open and shielded three-layer uniaxially anisotropic media are presented.

For microwave integrated circuit applications, the characteristics of interconnects have been investigated for the propagation modes, time response, crosstalk, coupling, delay, etc. In these analyses, it is assumed that quasi-TEM modes are guided along the multiconductor transmission lines. The analysis were performed for arbitrary number of transmission lines where the load and the source conditions were presented in terms of the

modal reflection and transmission coefficient matrices.

To perform the quasi-TEM analysis, the capacitance matrix for the multiconductor transmission line has to be obtained first. Both the spectral and the spatial domain methods have been proposed to calculate the capacitance matrix. In the spectral domain methods, two side walls are used to enclose the whole transmission line structure, and the thickness of the strip lines has not been considered. In using the spatial domain method, the structure has to be truncated to a finite extent to make the numerical implementation feasible. The infinite extent of the structure was also incorporated, but only a two-layer medium was considered.

In practical microwave integrated circuits, the dielectric loss due to the substrate and the conductor loss due to the metallic strips are also studied in the analysis of circuit performances.

Based on the scalar Green's function, a set of coupled integral equations is obtained for the charge distribution on the strip surfaces. Pulse basis functions and a point-matching scheme is used to solve numerically the set of integral equations for the charge distribution, and hence the capacitance matrix. The duality between the electrostatic formulation and the magnetostatic one is applied to calculate the inductance matrix. The conductance matrix is obtained by using the duality between the electrostatic problem and the current field problem. A perturbation method is used to calculate the resistance matrix.

Finally, a transmission line analysis is derived to obtain the transfer matrix for multiconductor uniform lines, which significantly reduces the effort in treating the load and the source conditions. Transient responses are obtained by using the Fourier transform. The results for two coupled lines are obtained.

With the ever increasing speed and density of modern integrated circuits, the need for electromagnetic wave analysis of phenomena such as the propagation of transient sig-

nals, especially the distortion of signal pulses, becomes crucial. One of the most important causes of pulse distortion is the frequency dependence of conductor loss, which is caused by the "skin effect", and which can be incorporated into the circuit models for transmission lines as frequency-dependent resistance and inductance per unit length. Efficient and accurate algorithms for calculating these parameters are increasingly important.

We have developed a hybrid cross-section finite element/coupled integral equation method. The technique is a combination of a cross-section finite element method, which is best for high frequencies. An interpolation between the results of these two methods gives very good results over the entire frequency range, even when few basis functions are used.

In the cross-section method, we divide each conductor into triangular patches and choose one of the patches from the return conductor to be our reference. We then calculate the resistance and inductance matrices for the patches. Using two conditions on the system, that the total current in each wire is the sum of the currents in the patches, and that the voltage on each patch in a wire must be the same (no transverse currents), we can reduce the matrices for the patches to the matrices for the wires. In the Weeks method, the patches are rectangles, and the quadruple integral is done quite easily in closed form. However, it is also possible to evaluate the quadruple integral in closed form for triangular patches, although the mathematics leading to this result is quite involved, and the final form of the answer is complicated. We therefore use triangular patches as the most flexible means of modelling conductors with arbitrary cross-sections; polygons are covered exactly, and we are able to model quite closely other shapes, such as circles.

As frequency increases, the need to keep the uniform current approximation valid in the patches requires either the addition of many more patches as the skin depth decreases, or a redistribution of the existing patches to the surface, where the current is. However, changing the distribution of patches makes it necessary to recalculate the resistance and inductance matrices of the patches, thus increasing the computation time. Since we use a



surface integral equation method for high frequencies, we do not change the distribution of the triangular patches for the cross-section method as we increase the frequency.

For high frequencies, we use a coupled surface integral equation technique. Under the quasi-TEM assumption, the frequency-dependent resistance and inductance result from the power dissipation and magnetic stored energy, which can be calculated by solving a magnetoquasistatic problem, with the vector potential satisfying Laplace's equation in the region outside all the conductors. The resistance and inductance are usually given by integrals of these field quantities over the cross-sections of the wires, but by using some vector identities it is possible to convert these expressions to integrals only over the surfaces of the wires. These expressions contain only the current at the surface of each conductor, the derivative of that current normal to the surface, and constants of the vector potential. A coupled integral equation is then derived to relate these quantities through Laplace's equation and its Green's function outside the conductors and the diffusion equation and its Green's function inside the conductors. The method of moments with pulse basis functions is used to solve the integral equations. This method differs from previous work in that the calculation of resistance and inductance is based on power dissipation and stored magnetic energy, rather than on impedance ratios. It will therefore be more easily extended to structures where non-TEM propagation can occur.

For the intermediate frequency range, where the conductors are on the order of the skin depth, we found it very efficient to interpolate between the results of the cross-section and surface methods. The interpolation function was based on the average size of the conductors, measured in skin depths, and was of the form  $1/(1 + 0.16a^2/\delta^4)$ , where  $a$  is the average cross-section of the conductors, and  $\delta$  is the skin depth.

## **PUBLICATIONS SUPPORTED BY ONR CONTRACT N00014-90-J-1002**

Analysis of diffraction from chiral gratings (S. H. Yueh and J. A. Kong), *Journal of Electromagnetic Waves and Applications*, Vol. 5, No. 7, 701-714, 1991.

Dyadic Green's functions in a planar stratified, arbitrarily magnetized linear plasma (T. M. Habashy, S. M. Ali, J. A. Kong, and M. D. Grossi), *Radio Science*, Vol. 26, No. 3, 701-716, May - June, 1991.

Current distribution, resistance, and inductance for superconducting strip transmission lines (D. M. Sheen, S. M. Ali, D. E. Oates, R. S. Withers, and J. A. Kong), *IEEE Trans. on Applied Superconductivity*, Vol. 1, No. 2, 108-115, June, 1991.

Electromagnetic radiation from a VLSI package and heatskin configuration (S. Y. Poh, C. F. Lee, K. Li, R. T. Shin, and J. A. Kong), submitted to *IEEE 1991 International Symposium on Electromagnetic Compatibility*, Hyatt Cherry Hill, Cherry Hill, NJ, August 13 - 15, 393-398, 1991.

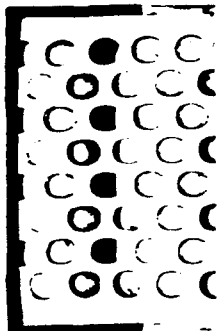
Electromagnetic calculation of soft x-ray diffraction from 01.  $\mu$ m-scale gold structures (M. L. Schattenburg, K. Li, R. T. Shin, J. A. Kong, D. B. Olster, and H. I. Smith), *Journal of Vacuum Science and Technology* as part of the proceedings of the 35th International Symposium on Electron, Ion, and Photon Beams (paper E84), Seattle, Washington, 1-8, May 28-31, 1991.

An inverse scattering view of modal structures in stratified Media (J. Xia, A. K. Jordan, and J. A. Kong), submitted for publication in *Journal of Optical Society of America, A*, March 1991.

The propagation characteristics of signal lines with crossing strips in multilayered anisotropic media (C. M. Lam, S. M. Ali, and J. A. Kong), *Journal of Electromagnetic Waves and Application*, Vol. 4, No. 10, 1005-1021, 1990.

Modelling of lossy microstrip lines with finite thickness (J. F. Kiang, S. M. Ali and J. A. Kong), *Progress in Electromagnetics Research*, No. 4, 85-116, Elsevier Publishing Company, 1991.

A hybrid method for the calculation of resistance and inductance of transmission lines with arbitrary cross section (M. J. Tsuk and J. A. Kong), *IEEE Transactions on Microwave Theory and Techniques*, Vol. 39, No. 8, 1338-1347, 1991.



## The Propagation Characteristics of Signal Lines with Crossing Strips in Multilayered Anisotropic Media

C. W. Lam, S. M. Ali, and J. A. Kong

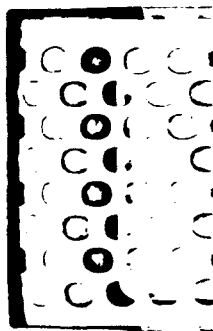
Department of Electrical Engineering and Computer Science  
and Research Laboratory of Electronics  
Massachusetts Institute of Technology  
Cambridge, MA 02139, USA

**Abstract**— In this paper, full modal analysis is used to study the dispersion characteristics of microstrip lines periodically loaded with crossing strips in a stratified uniaxially anisotropic medium. Dyadic Green's functions in the spectral domain for the multilayered medium in conjunction with the vector Fourier transform (VFT) are used to formulate a coupled set of vector integral equations for the current distribution on the signal line and the crossing strips. Galerkin's procedure is applied to derive the eigenvalue equation for the propagation constant. The effect of anisotropy for both open and shielded structures on the stopband properties is investigated.

### I. INTRODUCTION

In compact modules of high performance computers, signal transmission lines between integrated circuit chips are embedded in multilayered dielectric media. These signal lines are usually placed in different layers and run perpendicular to each other. The interaction between the orthogonal crossing lines and the signal line affects its propagation characteristics and may cause considerable signal distortion.

The interaction of a pair of crossing lines in an isotropic medium has been studied using a time-domain approach [1], where coupling is described qualitatively. This method becomes computationally expensive when the number of crossing lines increases. With many identical crossing strips uniformly distributed above the signal line, the transmission properties are characterized by stopbands due to the periodicity of the structure. Periodic structures have been investigated using frequency-domain methods. In [2], periodically nonuniform microstrip lines in an enclosure are analyzed on the basis of a numerical field calculation. A technique based on the network-analytical formalism of electromagnetic fields has been used to analyze striplines and finlines with periodic stubs [3]. The propagation characteristics of waves along a periodic array of parallel signal lines in a multilayered isotropic structure in the presence of a periodically perforated ground plane is studied in [4] and that in a mesh-plane environment is studied in [5]. More recently, the effect of the geometrical properties on the propagation characteristics of strip lines with periodic crossing strips embedded in a shielded one-layer isotropic medium have been investigated [6].



In this paper, both open and closed multilayered uniaxially anisotropic structures are considered. A full-wave analysis is used to study the propagation characteristics of a microstrip line in the presence of crossing strips. The signal line and the crossing strips are assumed to be located in two arbitrary layers of a stratified uniaxially anisotropic medium. An integral equation formulation using dyadic Green's functions in the periodically loaded structure is derived. Galerkin's method is then used to obtain the eigenvalue equation for the propagation constant. The effects of anisotropy on the stopband properties are investigated. Numerical results for open and shielded three-layer uniaxially anisotropic media are presented.

## II. FORMULATION OF THE PROBLEM

In this section, we present a dyadic Green's function formulation of the problem shown in Fig. 1(a) where the microstrip line and the crossing strips are placed at two different interfaces of a uniaxially anisotropic multilayered medium. The crossing strips are assumed to be placed in a layer ( $i$ ) and the signal line to be in a layer ( $j$ ). The crossing strips are considered to be periodic with period  $p$  as shown in Fig. 1(b). In general, the permittivity and permeability tensors of an arbitrary layer ( $l$ ) are assumed to be given by

$$\bar{\bar{\epsilon}}_l = \begin{pmatrix} \epsilon_l & 0 & 0 \\ 0 & \epsilon_l & 0 \\ 0 & 0 & \epsilon_{lz} \end{pmatrix} \quad (1)$$

and

$$\bar{\bar{\mu}}_l = \begin{pmatrix} \mu_l & 0 & 0 \\ 0 & \mu_l & 0 \\ 0 & 0 & \mu_{lz} \end{pmatrix} \quad (2)$$

where  $l = 0, 1, 2, \dots, n, \dots, t$ .

For the stratified medium, the electric fields in layers ( $i$ ) and ( $j$ ) due to current distributions  $\bar{J}_i(\bar{r}')$  and  $\bar{J}_j(\bar{r}')$  may be expressed as

$$\bar{E}_i(\bar{r}) = i\omega \iiint_V dV' \bar{G}_{ii}(\bar{r}, \bar{r}') \cdot \bar{J}_i(\bar{r}') + i\omega \iiint_V dV' \bar{G}_{ij}(\bar{r}, \bar{r}') \cdot \bar{J}_j(\bar{r}') \quad (3a)$$

$$\bar{E}_j(\bar{r}) = i\omega \iiint_V dV' \bar{G}_{ji}(\bar{r}, \bar{r}') \cdot \bar{J}_i(\bar{r}') + i\omega \iiint_V dV' \bar{G}_{jj}(\bar{r}, \bar{r}') \cdot \bar{J}_j(\bar{r}') \quad (3a)$$

where  $\bar{G}_{lm}(\bar{r}, \bar{r}')$  is the dyadic Green's function in layer ( $l$ ) due to current sources in layer ( $m$ ).

For the multilayered structure shown in Fig. 1(a), the current distributions on the conducting strips are assumed to be surface currents lying on planes transverse to  $z$ . Thus, if we are interested in the transverse electric fields  $\bar{E}_i^{(s)}$  and  $\bar{E}_j^{(s)}$  in layers ( $i$ ) and ( $j$ ), respectively, we can write

$$\bar{E}_i^{(s)}(\bar{r}) = \bar{E}_{ii}^{(s)}(\bar{r}) + \bar{E}_{ij}^{(s)}(\bar{r}) \quad (4a)$$

$$\bar{E}_j^{(s)}(\bar{r}) = \bar{E}_{ji}^{(s)}(\bar{r}) + \bar{E}_{jj}^{(s)}(\bar{r}) \quad (4b)$$

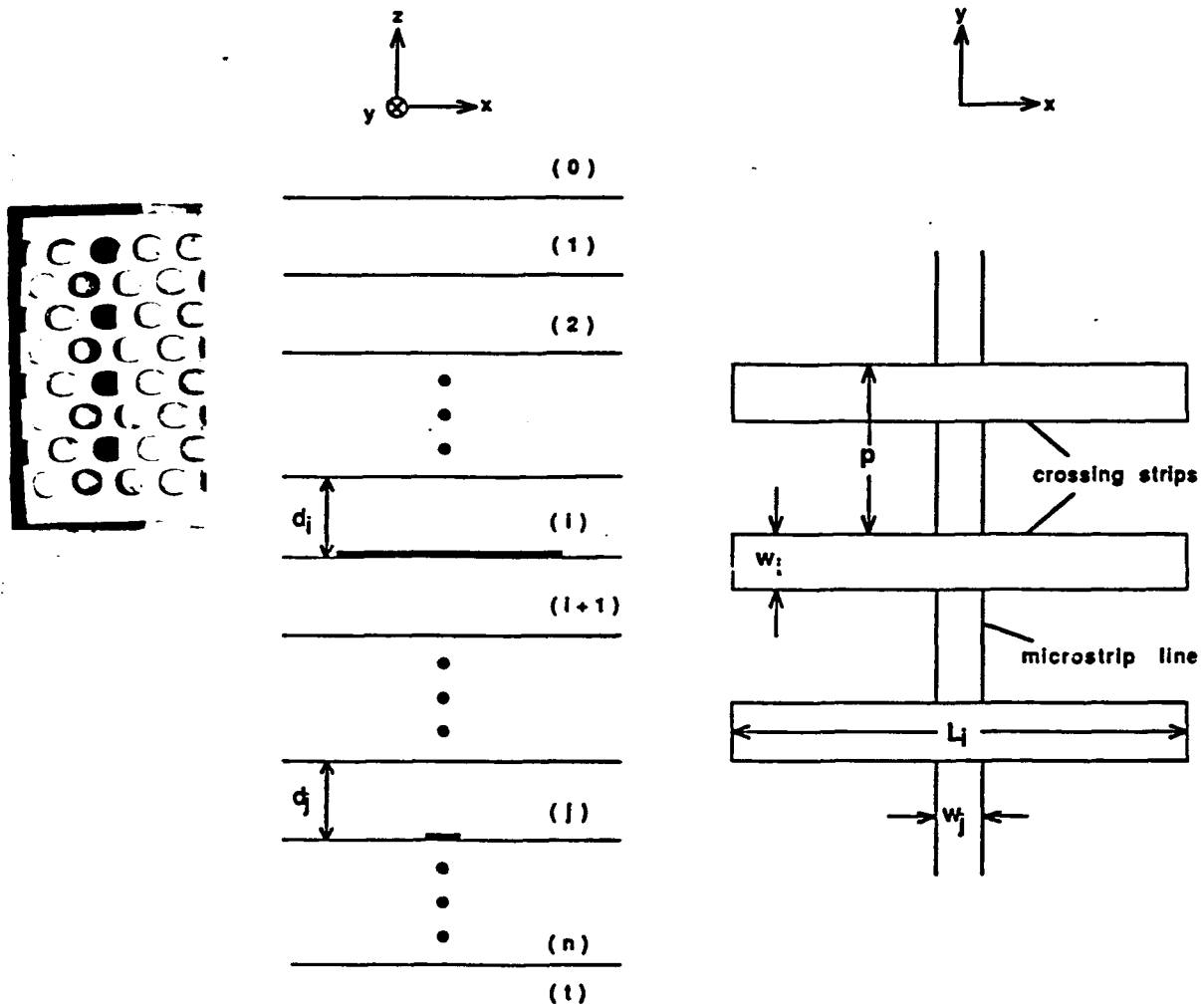


Figure 1. Geometrical configuration of a signal line in layer  $j$  loaded with crossing strips in layer  $i$ .

where  $\bar{E}_{lm}^{(s)}$  is the transverse electric field in layer  $(l)$  due to current sources in layer  $(m)$ , and is given by

$$\bar{E}_{lm}^{(s)}(\bar{r}) = i\omega \iiint_V dV' \bar{G}_{lm}^{(s)}(\bar{r}, \bar{r}') \cdot \bar{K}_m(\bar{r}') \quad (5)$$

$\bar{K}_m(\bar{r}')$  is the surface current distribution in layer  $(m)$ , and  $\bar{G}_{lm}^{(s)}(\bar{r}, \bar{r}')$  is the  $(2 \times 2)$  transverse part of the dyadic Green's function  $\bar{\bar{G}}_{lm}(\bar{r}, \bar{r}')$ .

Since the structure is assumed to be periodic in the  $y$ -direction, the electric field

$\bar{E}_l^{(s)}$  and the surface currents  $\bar{K}_m$  can be expressed using the Floquet harmonic representation in the  $y$ -direction. In this case we can get

$$\bar{E}_{lm}^{(s)}(\bar{r}) = i\omega \int_{-\infty}^{\infty} dx' \int_{-p/2}^{p/2} dy' \bar{G}_{lm}^{(s)}(\bar{r}, \bar{r}') \cdot \bar{K}_m(\bar{r}') \quad (6a)$$

where  $l = i, j$ , and

$$\bar{G}_{lm}^{(s)}(\bar{r}, \bar{r}') = \frac{2\pi}{p} \sum_{n=-\infty}^{\infty} \int_{-\infty}^{\infty} dk_x e^{i\bar{k}_{sn} \cdot (\bar{r}_s - \bar{r}'_s)} \bar{g}_{lm}^{(s)}(\bar{k}_{sn}; z, z') \quad (6b)$$

$$\bar{r}_s = \hat{x}x + \hat{y}y, \quad \bar{k}_{sn} = \hat{x}k_x + \hat{y}\beta_n, \quad \beta_n = \beta_0 + \frac{2n\pi}{p}$$

Here  $p$  is the period,  $\beta_0$  is the propagation constant of the dominant harmonic in the Floquet representation, and  $\bar{g}_{lm}^{(s)}(\bar{k}_{sn}; z, z')$  is the spectral dyadic Green's function.

Using the explicit expressions for the dyadic Green's functions  $\bar{G}_{ii}^{(s)}$ ,  $\bar{G}_{ij}^{(s)}$ ,  $\bar{G}_{ji}^{(s)}$  and  $\bar{G}_{jj}^{(s)}$  [7], the transverse electric fields on the surface of the conducting strips in layer (i) due to the currents in layer (j) can be expressed in the following form

$$\bar{E}_{ij}^{(s)}(\bar{r}_s) = -\frac{\pi}{p} \sum_{n=-\infty}^{\infty} \int_{-\infty}^{\infty} dk_x \bar{F}(\bar{k}_{sn}, \bar{r}_s) \cdot \bar{\xi}_{ij}(\bar{k}_{sn}) \cdot \bar{K}_j(\bar{k}_{sn}) \quad (7)$$

where  $\bar{F}(\bar{k}_{sn}, \bar{r}_s)$  is the kernel of the vector Fourier transform (VFT) given by [8]

$$\bar{F}(\bar{k}_{sn}, \bar{r}_s) = \frac{1}{k_{sn}} \begin{bmatrix} k_x & \beta_n \\ \beta_n & -k_x \end{bmatrix} e^{i\bar{k}_{sn} \cdot \bar{r}_s} \quad (8)$$

and  $\bar{K}_j(\bar{k}_{sn})$  is the vector Fourier transform of the surface current  $\bar{K}_j(\bar{r}'_s)$ . It is given by

$$\bar{K}_j(\bar{k}_{sn}) = \frac{1}{(2\pi)^2} \iint_{-\infty}^{\infty} d\bar{r}'_s \bar{F}(\bar{k}_{sn}, -\bar{r}'_s) \cdot \bar{K}_j(\bar{r}'_s) \quad (9)$$

The matrix  $\bar{\xi}_{ij}(\bar{k}_{sn})$  is given by

$$\bar{\xi}_{ij}(\bar{k}_{sn}) = \begin{bmatrix} f_{ij}^{\text{TM}} & 0 \\ 0 & f_{ij}^{\text{TE}} \end{bmatrix} \quad (10)$$

whose elements for different  $i$  and  $j$  are given in Appendix A.

In the above, the transverse electric field expressions  $\bar{E}_{lm}^{(s)}$  ( $l, m = i, j$ ) satisfy the boundary conditions at the dielectric interfaces of the layered medium. Applying the final boundary condition that the tangential electric field vanishes on the conducting strips, we can get the following set of dual vector integral equations for the currents on the metallic strips

$$\sum_{n=-\infty}^{\infty} \int_{-\infty}^{\infty} dk_x \bar{F}(\bar{k}_{sn}, \bar{r}_s) \cdot \bar{\xi}_{ii}(\bar{k}_{sn}) \cdot \bar{K}_i(\bar{k}_{sn}) + \sum_{n=-\infty}^{\infty} \int_{-\infty}^{\infty} dk_x \bar{F}(\bar{k}_{sn}, \bar{r}_s) \cdot \bar{\xi}_{ij}(\bar{k}_{sn}) \cdot \bar{K}_j(\bar{k}_{sn}) = 0, \quad \bar{r}_s \in S_i \quad (11)$$

on the crossing strips, and

$$\sum_{n=-\infty}^{\infty} \int_{-\infty}^{\infty} dk_z \bar{F}(\bar{k}_{sn}, \bar{r}_s) \cdot \bar{\xi}_{ji}(\bar{k}_{sn}) \cdot \bar{K}_i(\bar{k}_{sn}) + \sum_{n=-\infty}^{\infty} \int_{-\infty}^{\infty} dk_z \bar{F}(\bar{k}_{sn}, \bar{r}_s) \cdot \bar{\xi}_{jj}(\bar{k}_{sn}) \cdot \bar{K}_j(\bar{k}_{sn}) = 0, \quad \bar{r}_s \in S_j \quad (12)$$

on the signal line.

The next step is to solve this coupled set of vector integral equations to find the dispersion relation for the signal line in the presence of the crossing strips.

### III. GALERKIN'S METHOD AND THE EIGENVALUE EQUATION

The formulation up to this stage is exact. We now solve the set of vector integral equations (11) and (12) by using Galerkin's method. The unknown current distributions on the crossing strips  $\bar{K}_i(\bar{r}_s)$  and on the signal line  $\bar{K}_j(\bar{r}_s)$  are expanded in terms of the appropriate vector basis functions as follows:

$$\bar{K}_i(x, y) = \sum_{m=1}^M \sum_{r=1}^R \bar{\Phi}_{mr}(x, y) \cdot \bar{A}_{mr} \quad (13)$$

$$\bar{K}_j(x, y) = \sum_{k=1}^K \sum_{q=-Q_1}^{Q_2} \bar{\Psi}_k(x) e^{i\beta_q y} \cdot \bar{B}_{kq} \quad (14)$$

where  $\bar{K}_i(x, y)$  and  $\bar{K}_j(x, y)$  are the surface currents on the crossing strips and the signal line, respectively,  $\bar{\Phi}_{mr}$  and  $\bar{\Psi}_k e^{i\beta_q y}$  are the basis functions,  $\bar{A}_{mr}$  and  $\bar{B}_{kq}$  are the expansion coefficients.

Using (13) and (14), the vector Fourier transform (VFT) of the currents  $\bar{K}_i(\bar{r}_s)$  and  $\bar{K}_j(\bar{r}_s)$  are obtained as

$$\bar{\bar{K}}_i(\bar{k}_{sn}) = \sum_{m=1}^M \sum_{r=1}^R \bar{U}_{(+ )mr,n}(k_z, \beta) \cdot \bar{A}_{mr} \quad (15)$$

$$\bar{\bar{K}}_j(\bar{k}_{sn}) = \sum_{k=1}^K \sum_{q=-Q_1}^{Q_2} \bar{V}_{(+ )kq,n}(k_z, \beta) \cdot \bar{B}_{kq} \quad (16)$$

where

$$\bar{U}_{(\pm )mr,n}(k_z, \beta) = \frac{1}{(2\pi)^2} \iint d\bar{r}_s \bar{F}(\bar{k}_{sn}, \mp \bar{r}_s) \cdot \bar{\Phi}_{mr}(x, y) \quad (17)$$

and

$$\bar{V}_{(\pm )kq,n}(k_z, \beta) = \frac{1}{(2\pi)^2} \iint d\bar{r}_s \bar{F}(\bar{k}_{sn}, \mp \bar{r}_s) \cdot \bar{\Psi}_k(x) e^{\pm i\beta_q y} \quad (18)$$

Substituting (15) and (16) into (11) and (12), we obtain

$$\sum_{m=1}^M \sum_{r=1}^R \sum_{n=-\infty}^{\infty} \int_{-\infty}^{\infty} dk_z \bar{F}(\bar{k}_{sn}, \bar{r}_s) \cdot \bar{\xi}_{ii}(\bar{k}_{sn}) \cdot \bar{U}_{(+ )mr,n}(k_z, \beta) \cdot \bar{A}_{mr}$$

$$+ \sum_{k=1}^K \sum_{q=-Q_1}^{Q_2} \sum_{n=-\infty}^{\infty} \int_{-\infty}^{\infty} dk_z \bar{F}(\bar{k}_{sn}, \bar{r}_s) \cdot \bar{\xi}_{ij}(\bar{k}_{sn}) \cdot \bar{V}_{(+ )kq,n}(k_z, \beta) \cdot \bar{B}_{kq} = 0 \quad (19)$$

for  $\bar{r}_s \in S_i$ , and

$$\begin{aligned} & \sum_{m=1}^M \sum_{r=1}^R \sum_{n=-\infty}^{\infty} \int_{-\infty}^{\infty} dk_z \bar{F}(\bar{k}_{sn}, \bar{r}_s) \cdot \bar{\xi}_{ji}(\bar{k}_{sn}) \cdot \bar{U}_{(+ )mr,n}(k_z, \beta) \cdot \bar{A}_{mr} \\ & + \sum_{k=1}^K \sum_{q=-Q_1}^{Q_2} \sum_{n=-\infty}^{\infty} \int_{-\infty}^{\infty} dk_z \bar{F}(\bar{k}_{sn}, \bar{r}_s) \cdot \bar{\xi}_{jj}(\bar{k}_{sn}) \cdot \bar{V}_{(+ )kq,n}(k_z, \beta) \cdot \bar{B}_{kq} = 0 \end{aligned} \quad (20)$$

for  $\bar{r}_s \in S_j$ .

Multiplying (19) by  $\bar{\Phi}_{uv}^{\dagger}(x, y)$  and integrating over the support of  $\bar{K}_i(\bar{r}_s)$  for  $u = 1, 2, \dots, M$  and  $v = 1, 2, \dots, R$ , we obtain

$$\begin{aligned} & \sum_{m=1}^M \sum_{r=1}^R \sum_{n=-\infty}^{\infty} \int_{-\infty}^{\infty} dk_z \bar{U}_{(- )uv,n}^{\dagger}(k_z, \beta) \cdot \bar{\xi}_{ii}(\bar{k}_{sn}) \cdot \bar{U}_{(+ )mr,n}(k_z, \beta) \cdot \bar{A}_{mr} \\ & + \sum_{k=1}^K \sum_{q=-Q_1}^{Q_2} \sum_{n=-\infty}^{\infty} \int_{-\infty}^{\infty} dk_z \bar{U}_{(- )uv,n}^{\dagger}(k_z, \beta) \cdot \bar{\xi}_{ij}(\bar{k}_{sn}) \cdot \bar{V}_{(+ )kq,n}(k_z, \beta) \cdot \bar{B}_{kq} = 0 \end{aligned} \quad (21)$$

Similarly, multiplying (20) by  $\bar{\Psi}_s^{\dagger}(x) e^{-i\beta_t y}$  and integrating over the support of  $\bar{K}_j(\bar{r}_s)$  for  $s = 1, 2, \dots, K$  and  $t = -Q_1, \dots, 0, \dots, Q_2$ , we obtain

$$\begin{aligned} & \sum_{m=1}^M \sum_{r=1}^R \sum_{n=-\infty}^{\infty} \int_{-\infty}^{\infty} dk_z \bar{V}_{(- )st,n}^{\dagger}(k_z, \beta) \cdot \bar{\xi}_{ji}(\bar{k}_{sn}) \cdot \bar{U}_{(+ )mr,n}(k_z, \beta) \cdot \bar{A}_{mr} \\ & + \sum_{k=1}^K \sum_{q=-Q_1}^{Q_2} \sum_{n=-\infty}^{\infty} \int_{-\infty}^{\infty} dk_z \bar{V}_{(- )st,n}^{\dagger}(k_z, \beta) \cdot \bar{\xi}_{jj}(\bar{k}_{sn}) \cdot \bar{V}_{(+ )kq,n}(k_z, \beta) \cdot \bar{B}_{kq} = 0 \end{aligned} \quad (22)$$

Equations (21) and (22) constitute a system of  $(S + T)$  linear algebraic equations with  $S = MR$  and  $T = K(Q_1 + Q_2 + 1)$ , and may be written in matrix form as

$$\bar{N} \cdot \bar{c} = 0 \quad (23a)$$

where

$$\bar{N} = \begin{bmatrix} [N_{11}]_{S \times S} & [N_{12}]_{S \times T} \\ [N_{21}]_{T \times S} & [N_{22}]_{T \times T} \end{bmatrix} \quad (23b)$$

and

$$\bar{c} = \begin{bmatrix} [A_{mr}]_{S \times 1} \\ [B_{kq}]_{T \times 1} \end{bmatrix} \quad (23c)$$



Each element of the submatrices of  $\bar{N}$  is given by

$$[N_{11}]_{uv,mr} = \sum_{n=-\infty}^{\infty} \int_{-\infty}^{\infty} dk_z \bar{U}_{(-)uv,n}^{\dagger}(k_z, \beta) \cdot \bar{\xi}_{ii}(\bar{k}_{sn}) \cdot \bar{U}_{(+ )mr,n}(k_z, \beta) \quad (24a)$$

$$[N_{12}]_{uv,kq} = \sum_{n=-\infty}^{\infty} \int_{-\infty}^{\infty} dk_z \bar{U}_{(-)uv,n}^{\dagger}(k_z, \beta) \cdot \bar{\xi}_{ij}(\bar{k}_{sn}) \cdot \bar{V}_{(+ )kq,n}(k_z, \beta) \quad (24b)$$

$$[N_{21}]_{st,mr} = \sum_{n=-\infty}^{\infty} \int_{-\infty}^{\infty} dk_z \bar{V}_{(-)st,n}^{\dagger}(k_z, \beta) \cdot \bar{\xi}_{ji}(\bar{k}_{sn}) \cdot \bar{U}_{(+ )mr,n}(k_z, \beta) \quad (24c)$$

$$[N_{22}]_{st,kq} = \sum_{n=-\infty}^{\infty} \int_{-\infty}^{\infty} dk_z \bar{V}_{(-)st,n}^{\dagger}(k_z, \beta) \cdot \bar{\xi}_{jj}(\bar{k}_{sn}) \cdot \bar{V}_{(+ )kq,n}(k_z, \beta) \quad (24d)$$

For nontrivial solution to exist, the determinant of the coefficient matrix of (21) and (22) must be zero,

$$\det [\bar{N}(\omega, \beta)] = 0 \quad (25)$$

This is the eigenvalue equation for the propagation constant  $\beta$  which describes the dispersion relation of the loaded microstrip line in the multilayered anisotropic medium.

The next step is to choose appropriate basis functions for the surface currents  $\bar{K}_j(\bar{r}_s)$  and  $\bar{K}_i(\bar{r}_s)$  on the signal line and the crossing strips, respectively. The expansion functions we use are

$$\bar{\Phi}_{mr}(x, y) = \frac{p}{2\pi} \begin{bmatrix} P_m(x, L_i) & 0 \\ 0 & Q_m(x, L_i) \end{bmatrix} \begin{bmatrix} Q_r(y, w_i) & 0 \\ 0 & R_r(y, w_i) \end{bmatrix} \quad (26)$$

and

$$\bar{\Psi}_k(x) = \frac{p}{2\pi} \begin{bmatrix} P_k(x, w_j) & 0 \\ 0 & Q_k(x, w_j) \end{bmatrix} \quad (27)$$

where

$$P_n(\alpha, \gamma) = \frac{1}{\gamma} \sin \frac{2n\pi\alpha}{\gamma} \quad (28)$$

$$Q_n(\alpha, \gamma) = \frac{\cos \frac{2(n-1)\pi\alpha}{\gamma}}{\sqrt{(\frac{\gamma}{2})^2 - \alpha^2}} \quad (29)$$

$$R_n(\alpha, \gamma) = \frac{1}{\gamma} \sin \frac{n\pi(\alpha + \gamma/2)}{\gamma} \quad (30)$$

$w_i$  and  $w_j$  are the widths of the crossing strips and the signal line, respectively, and  $L_i$  is the length of the crossing strips. When choosing the basis functions for the surface currents, it should be borne in mind that the current cannot have

a normal component to the strip edges. Furthermore, the edge condition for the parallel component should be considered. By substituting (26) and (27) into (17) and (18), respectively, we can get

$$\bar{U}_{(\pm)mr,n}(k_x, \beta) = \frac{p}{(2\pi)^3 k_{sn}} \begin{bmatrix} \pm X_m(k_x, L_i) & 0 \\ 0 & Y_m(k_x, L_i) \end{bmatrix} \begin{bmatrix} Y_r(\beta_n, w_i) & 0 \\ 0 & Z_{(\pm)r}(\beta_n, w_i) \end{bmatrix} \quad (31)$$

and

$$\bar{V}_{(\pm)kq,n}(k_x, \beta) = \frac{p\delta_{qn}}{(2\pi)^3 k_{sn}} \begin{bmatrix} \pm X_k(k_x, w_j) & 0 \\ 0 & Y_k(k_x, w_j) \end{bmatrix} \quad (32)$$

where

$$X_n(\alpha, \gamma) = i(-1)^n \frac{4n\pi \sin \frac{\alpha\gamma}{2}}{4n^2\pi^2 - \alpha^2\gamma^2} \quad (33)$$

$$Y_n(\alpha, \gamma) = \frac{\pi}{2} \left\{ J_0[(n-1)\pi + \frac{\alpha\gamma}{2}] + J_0[(n-1)\pi - \frac{\alpha\gamma}{2}] \right\} \quad (34)$$

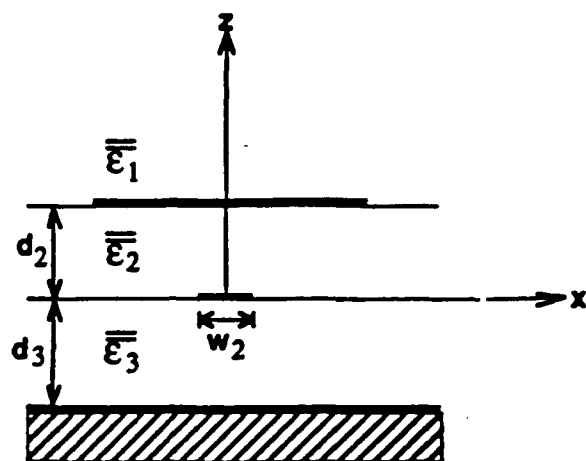
$$Z_{(\pm)n}(\alpha, \gamma) = \frac{-i}{n^2\pi^2 - \alpha^2\gamma^2} \left[ e^{\frac{i n \pi}{2}} (n\pi \pm \alpha\gamma) \sin\left(\frac{n\pi}{2} \mp \frac{\alpha\gamma}{2}\right) - e^{\frac{-i n \pi}{2}} (n\pi \mp \alpha\gamma) \sin\left(\frac{n\pi}{2} \pm \frac{\alpha\gamma}{2}\right) \right] \quad (35)$$

Equations (31) and (32) are then substituted into the determinantal equation (25) for the calculation of the dispersion characteristics.

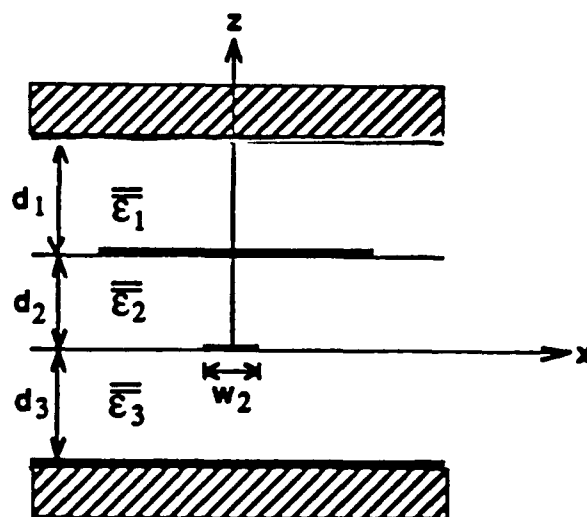
#### IV. NUMERICAL TREATMENT AND RESULTS

In this section, we present numerical results for open and closed three-layer structures with the crossing strips and the signal line embedded in two different layers as shown in Figs. 2(a) and (b). In numerical calculation, the infinite series of Floquet modes and the basis functions are truncated. The ranges of indices in (24) are chosen as:  $-10 \leq n \leq 9$ ,  $k = 1$ ,  $-1 \leq q \leq 0$ ,  $1 \leq m \leq 3$ ,  $r = 1$ ,  $s = 1$ ,  $-1 \leq t \leq 0$ ,  $1 \leq u \leq 3$ , and  $v = 1$ . It can be seen that each element in the coefficient matrix can be reduced to a sum of TE and TM terms, a summation over  $n$  Floquet modes, and an integral over  $k_x$ . Due to the symmetrical properties of the Green's function, the basis functions and the test functions, all the integrands are found to be even functions of  $k_x$ . So the integration path can be reduced to an integral from 0 to  $\infty$ . In numerical computation, the path of integration in the complex  $k_x$  plane is deformed to avoid the singularities on the real axis [9].

In the following calculations, the parameters used for Fig. 2 are:  $d_1 = d_2 = d_3 = 0.2$  mm,  $p = 0.5$  mm,  $w_1 = w_2 = 0.125$  mm,  $L_1 = 1.7$  mm, and  $\mu_j = \mu_z = \mu_0$ . Since the crossing strip length is much longer than the signal line width, the current near the crossing strip edges is relatively small so that the edge condition in the basis functions can be neglected.



(a)



(b)

Figure 2. (a) Cross section of an open structure. (b) Cross section of a closed structure.

Figure 3 shows the dispersion characteristics of a closed microstrip line loaded with periodic crossing strips (Fig. 2(b)). The result shows that the first stopband appears due to the coupling between the Floquet modes  $n = 0$  and  $n = -1$  of the fundamental mode of the signal line. The upper and lower bounds of the stopband is denoted by  $\omega_U$  and  $\omega_L$ , respectively. At higher frequencies, higher order stopbands are encountered because of the interaction with the higher order modes of the signal line. However, we concentrate only on the first stopband which is in the region of practical interest.

In Fig. 4, the dispersion characteristics of an open and a shielded structure are plotted in solid and dashed lines, respectively. It can be seen that both the stopband position and width are close to those of each other. This is because the fields are mostly confined under the first layer where the coupling between signal line and crossing strips takes place. So removing the top conducting plate does not affect the stopband properties much in this case. This point is illustrated in Figs. 5(a) and (b) which shows the effect of changing  $d_1$  on the stopband position and width, respectively. In the following, we are going to investigate the effect of anisotropy in the second and the third layer of a closed structure. It is believed that similar effects can be observed in an open structure.

The plot in Fig. 6 shows the effect of the anisotropy ratio ( $AR = \epsilon_2/\epsilon_{2z}$ ) of the second layer on the stopband position and the stopband width. The center frequency of the stopband is not much affected by the anisotropy. However, the stopband width is quite sensitive to it. The width increases with  $1/AR$ . For fixed  $\epsilon_2$ , it corresponds to an increase of  $\epsilon_{2z}$ , which enhances coupling between the signal line and the crossing strips, resulting in the rise of stopband width. For  $1/AR > 1$ , it is found in the dispersion diagram that a high order stopband starts to merge with the first order stopband, resulting in a large stopband width. Fig. 6 is thus plotted up to that value only.

In Fig. 7, we investigate the effect of anisotropy in the third layer on the stopband properties. As we have expected, the stopband width is not so sensitive to the anisotropy in the third layer as it is in the second layer where coupling occurs. The change of stopband position with the anisotropy is close to that in the second layer. Both are due to the change of the dispersion characteristics of the signal line which results in the lowering of the intersecting point of the Floquet modes  $n = 0$  and  $n = -1$ . A high order stopband is encountered for  $1/AR > 1$ .

Various combinations of substrate materials have been used to minimize the stopband width for the closed structure (Fig. 2(b)). The results are summarized in the following table:

Case	layer 1	layer 2	layer 3	$(k_0 p/\pi)_c$	$\Delta(k_0 p/\pi)$
1	$10\epsilon_0$	sapph.	$10\epsilon_0$	0.3093	5.93E-3
2	$10\epsilon_0$	$10\epsilon_0$	$10\epsilon_0$	0.3144	3.67E-3
3	$10\epsilon_0$	Eps-10	$10\epsilon_0$	0.3061	3.40E-3
4	$2.3\epsilon_0$	$10\epsilon_0$	$10\epsilon_0$	0.3194	0.80E-3
5	$2.3\epsilon_0$	$10\epsilon_0$	sapph.	0.3054	0.53E-3
6	$\epsilon_0$	$10\epsilon_0$	sapph.	0.3058	0.87E-3

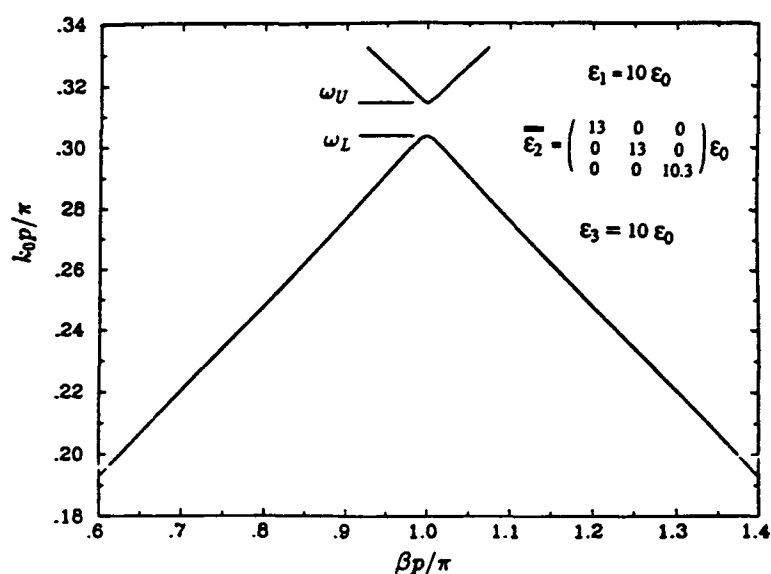


Figure 3. The dispersion characteristics of a closed structure with  $\epsilon_1 = \epsilon_{1z} = 10\epsilon_0$ ,  $\epsilon_2 = 13\epsilon_0$ ,  $\epsilon_{2z} = 10.3\epsilon_0$ , and  $\epsilon_3 = \epsilon_{3z} = 10\epsilon_0$ .

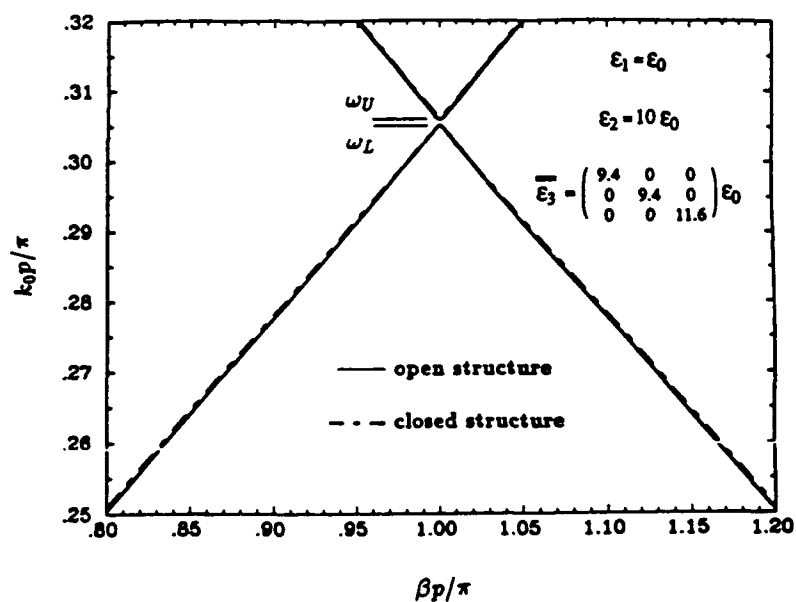
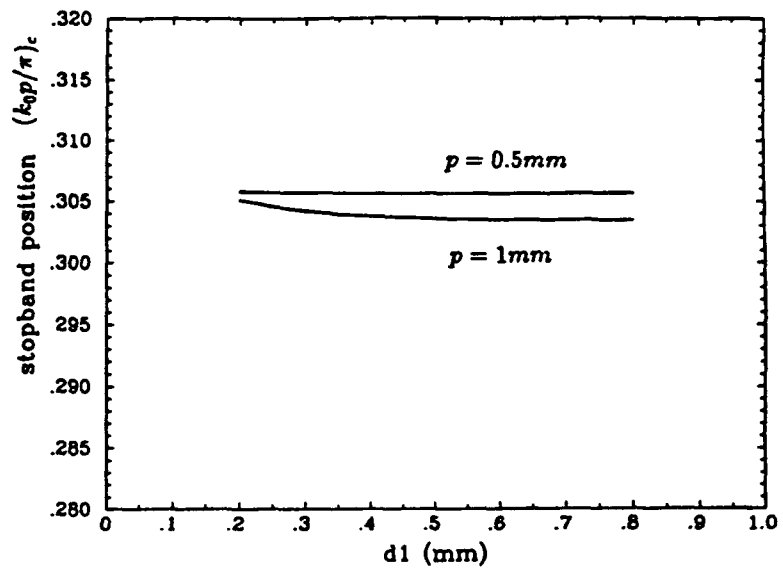
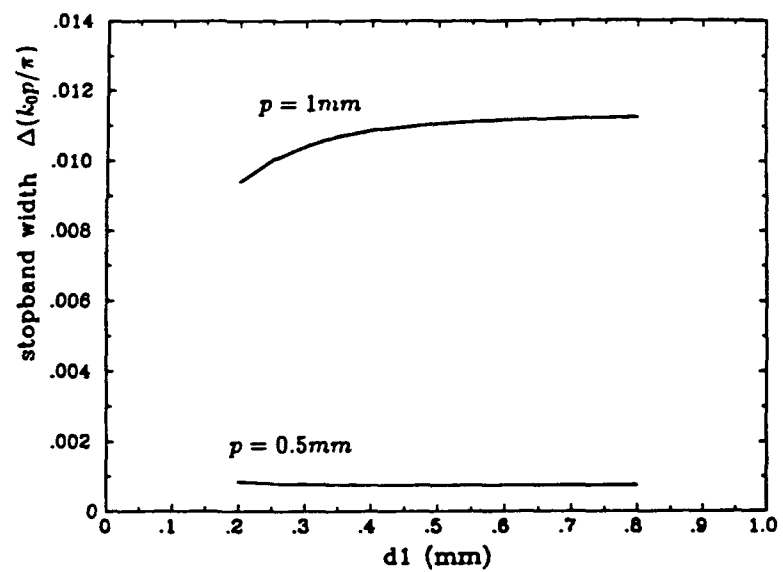


Figure 4. The dispersion characteristics of an open structure with  $\epsilon_1 = \epsilon_{1z} = \epsilon_0$ ,  $\epsilon_2 = \epsilon_{2z} = 10\epsilon_0$ ,  $\epsilon_3 = 9.4\epsilon_0$ , and  $\epsilon_{3z} = 11.6\epsilon_0$ .



(a)



(b)

Figure 5. The effect of  $d_1$  on the stopband: (a) position and (b) width.  $\epsilon_1 = \epsilon_{1z} = \epsilon_0$ ,  $\epsilon_2 = \epsilon_{2z} = 10\epsilon_0$ ,  $\epsilon_3 = 9.4\epsilon_0$ , and  $\epsilon_{3z} = 11.6\epsilon_0$ .

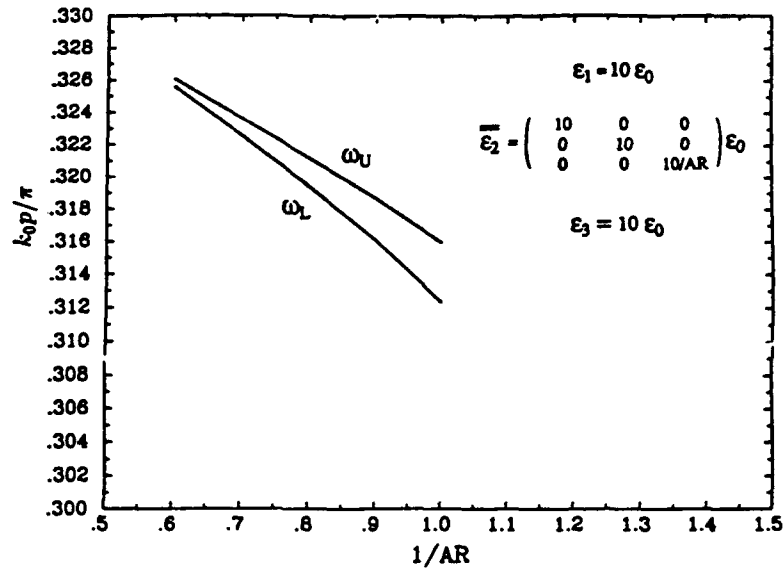


Figure 6. The effect of  $AR$  in the second layer on the upper and lower bounds of the stopband,  $\epsilon_1 = \epsilon_{1z} = 10\epsilon_0$ ,  $\epsilon_2 = 10\epsilon_0$ ,  $\epsilon_3 = \epsilon_{3z} = 10\epsilon_0$ .

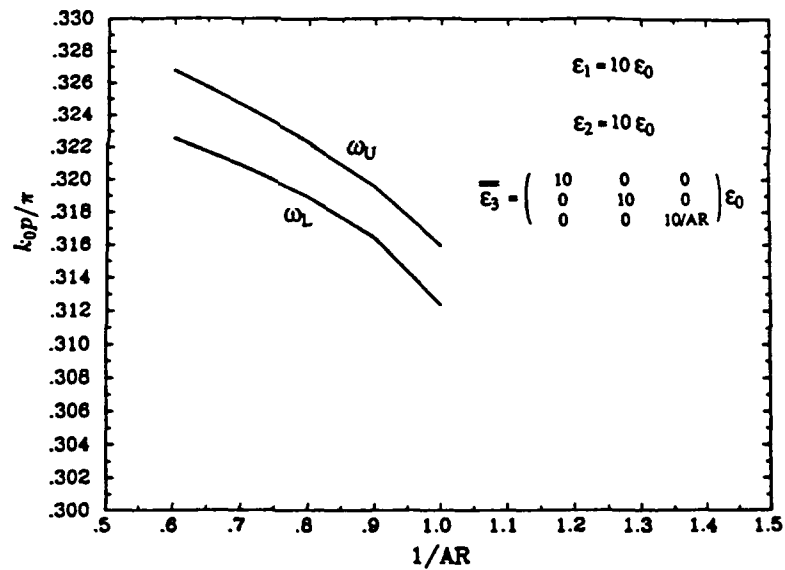


Figure 7. The effect of  $AR$  in the third layer on the upper and lower bounds of the stopband,  $\epsilon_1 = \epsilon_{1z} = 10\epsilon_0$ ,  $\epsilon_2 = \epsilon_{3z} = 10\epsilon_0$ ,  $\epsilon_3 = 10\epsilon_0$ .

where  $(k_0 p / \pi)_c$  is the normalized center frequency of the stopband and  $\Delta(k_0 p / \pi)$  is the normalized stopband width.

The two types of anisotropic substrates considered are Epsilam-10 ( $\epsilon = 13\epsilon_0$ ,  $\epsilon_z = 10.3\epsilon_0$ ) and sapphire ( $\epsilon = 9.4\epsilon_0$ ,  $\epsilon_z = 11.6\epsilon_0$ ). Comparison shows that the fifth case has the smallest stopband width. In fact, the stopband width is quite sensitive to the separation of the crossing strips due to the resonance effect [6]. Once the periodicity  $p$  is fixed, the stopband width can be minimized by a proper choice of substrate material.

## V. CONCLUSIONS

A dyadic Green's function formulation for the analysis of open and closed microstrip lines in the presence of periodic crossing strips in a stratified uniaxially anisotropic medium is presented. The dispersion characteristics for a three-layer structure is studied. Numerical results illustrate the relationship between the stopband properties and the material parameters. The effect of anisotropy has also been investigated. It is found that the crossing strip separation and the anisotropy in the second layer are important factors affecting the stopband width. To achieve small stopband width, careful choice of anisotropy must be made to avoid the lowering of the high order stopband. It should also be noted that by the proper choice of substrate materials, the stopband width can be much reduced for fixed crossing strip separation.

## APPENDIX A

Using the dyadic Green's function formulation [7], the elements of  $\bar{\bar{\xi}}_{ij}(\bar{k}_{sn})$  can be obtained as follows:

For  $i = j$ , where the source and observation points are in the same layer, we have

$$f_{jj}^{\text{TE}} = \frac{\omega \mu_j}{k_{jz}^{(h)}} \frac{1}{\left(1 - R_{Uj}^{\text{TE}} R_{\cap j}^{\text{TE}} e^{2ik_{jz}^{(h)} d_j}\right)} \left(1 + R_{Uj}^{\text{TE}} e^{2ik_{jz}^{(h)} d_j}\right) \left(1 + R_{\cap j}^{\text{TE}}\right) \quad (\text{A1})$$

$$f_{jj}^{\text{TM}} = \frac{1}{\omega \epsilon_j} k_{jz}^{(e)} \frac{1}{\left(1 - R_{Uj}^{\text{TM}} R_{\cap j}^{\text{TM}} e^{2ik_{jz}^{(e)} d_j}\right)} \left(1 - R_{Uj}^{\text{TM}} e^{2ik_{jz}^{(e)} d_j}\right) \left(1 - R_{\cap j}^{\text{TM}}\right) \quad (\text{A2})$$

and for  $j > i$ , where the source is in layer ( $j$ ) and observation point is in layer ( $i$ ), we have

$$f_{ij}^{\text{TE}} = \frac{\omega \mu_j}{k_{jz}^{(h)}} \frac{X_{Uj,i}^{\text{TE}}}{\left(1 - R_{\cap j}^{\text{TE}} R_{Uj}^{\text{TE}} e^{2ik_{jz}^{(h)} d_j}\right)} e^{ik_{jz}^{(h)} d_j} \left(1 + R_{\cap j}^{\text{TE}}\right) \left(1 + R_{Ui}^{\text{TE}} e^{2ik_{iz}^{(h)} d_i}\right) \quad (\text{A3})$$



$$f_{ij}^{TM} = \frac{1}{\omega \epsilon_j} k_{iz}^{(e)} \frac{k_j}{k_i} \frac{X_{Uij}^{TM}}{(1 - R_{\cap j}^{TM} R_{Uj}^{TM} e^{2ik_{jz}^{(e)} d_j})} e^{ik_{jz}^{(e)} d_j} (1 - R_{\cap j}^{TM}) (1 - R_{Ui}^{TM} e^{2ik_{iz}^{(e)} d_i}) \quad (A4)$$

where  $X_{Uij}^{TE}$  and  $X_{Uij}^{TM}$  are, respectively, the TE and TM upward transmission coefficients from layer (j) to layer (i), given by

$$X_{Ul,m}^{TE} = X_{U(l+1),m}^{TE} e^{ik_{(l+1)z}^{(h)} d_{(l+1)}} \frac{(1 + R_{U(l+1)}^{TE})}{(1 + R_{Ul}^{TE} e^{2ik_{lz}^{(h)} d_l})} \quad (A5)$$

$$X_{Ul,m}^{TM} = X_{U(l+1),m}^{TM} \frac{k_l}{k_{lz}^{(e)}} \frac{k_{(l+1)z}^{(e)}}{k_{(l+1)}} e^{ik_{(l+1)z}^{(e)} d_{(l+1)}} \frac{(1 - R_{U(l+1)}^{TM})}{(1 - R_{Ul}^{TM} e^{2ik_{lz}^{(e)} d_l})} \quad (A6)$$

for  $l = (m-2), (m-3), \dots, 0$ , and for  $l = (m-1)$ , we have

$$X_{U(m-1),m}^{TE} = \frac{(1 + R_{Um}^{TE})}{(1 + R_{U(m-1)}^{TE} e^{2ik_{(m-1)z}^{(h)} d_{(m-1)}})} \quad (A7)$$

$$X_{U(m-1),m}^{TM} = \frac{k_l}{k_{lz}} \frac{k_{mz}}{k_m} \frac{(1 - R_{Um}^{TM})}{(1 - R_{U(m-1)}^{TM} e^{2ik_{(m-1)z}^{(e)} d_{(m-1)}})} \quad (A8)$$

and

$$k_{jz}^{(h)} = \sqrt{k_j^2 - \frac{\mu_j}{\mu_{jz}} k_s^2} \quad (A9)$$

$$k_{jz}^{(e)} = \sqrt{k_j^2 - \frac{\epsilon_j}{\epsilon_{jz}} k_s^2} \quad (A10)$$

$$k_j^2 = \omega^2 \epsilon_j \mu_j \quad (A11)$$

Using the symmetrical properties of the dyadic Green's function in the layered media, it can be shown that  $f_{ji}^\alpha = f_{ij}^\alpha$ , where  $\alpha$  denotes TE or TM. In the above equations, the superscripts (h) and (e) denote TE and TM fields, respectively.  $R_{\cap l}^\alpha$  and  $R_{Ul}^\alpha$  are, respectively, the Fresnel reflection coefficients at the lower and upper boundaries of layer (l) and can be determined recursively by the following relations

$$R_{\cap l}^\alpha = \frac{R_{l(l+1)}^\alpha + R_{\cap(l+1)}^\alpha e^{2ik_{(l+1)z}^\alpha d_{l+1}}}{1 + R_{l(l+1)}^\alpha R_{\cap(l+1)}^\alpha e^{2ik_{(l+1)z}^\alpha d_{l+1}}} \quad (A12)$$

where  $l = 0, \dots, (n-1)$  and  $R_{\cap n}^\alpha = R_{nl}^\alpha$ .

$$R_{U,l}^{\alpha} = \frac{R_{l(l-1)}^{\alpha} + R_{U(l-1)}^{\alpha} e^{2ik_{(l-1)z}^{\alpha} d_{l-1}}}{1 + R_{l(l-1)}^{\alpha} R_{U(l-1)}^{\alpha} e^{2ik_{(l-1)z}^{\alpha} d_{l-1}}} \quad (A13)$$

where  $l = 2, 3, \dots, t$  and  $R_{U,1}^{\alpha} = R_{10}^{\alpha}$ .  $R_{l(l-1)}^{\alpha}$  and  $R_{l(l+1)}^{\alpha}$  are the Fresnel reflection coefficients across the interface between layers ( $l$ ) and ( $l+1$ ).

#### ACKNOWLEDGMENTS

This work was supported by the NSF under Grant 8620029-ECS, by the Joint Services Electronics Program under Contract DAAL03-89-C-0001, by the RADCS under Contract F19628-88-K-0013, by the ARO under Contract DAAL03-88-J-0057, and by the ONR under Contract N00014-90-J-1002.

The Editor thanks T. M. Habashy, J. F. Kiang, and one anonymous Reviewer for reviewing the paper.

#### REFERENCES

1. Koike, S., N. Yoshida, and I. Fukai, "Transient analysis of coupling between crossing lines in three-dimensional space," *IEEE Trans. Microwave Theory Tech.*, Vol. MTT-35, No. 1, 67-71, Jan. 1987.
2. Glandorf, F. J., and I. Wolff, "A spectral-domain analysis of periodically non-uniform microstrip lines," *IEEE Trans. Microwave Theory Tech.*, Vol. MTT-35, No. 3, 336-343, Mar. 1987.
3. Kitazawa, T., and R. Mittra, "An investigation of striplines and fin lines with periodic stubs," *IEEE Trans. Microwave Theory Tech.*, Vol. MTT-32, No. 7, 684-688, July 1984.
4. Chan, C. H., and R. Mittra, "The propagation characteristics of signal lines embedded in a multilayered structure in the presence of a periodically perforated ground plane," *IEEE Trans. Microwave Theory Tech.*, Vol. MTT-36, No. 6, 968-975, June 1988.
5. Rubin, B. J., "The propagation characteristics of signal lines in a mesh-plane environment," *IEEE Trans. Microwave Theory Tech.*, Vol. MTT-32, No. 5, 522-531, May 1984.
6. Kiang, J. F., S. M. Ali, and J. A. Kong, "Propagation properties of strip lines periodically loaded with crossing strips," *IEEE Trans. Microwave Theory Tech.*, Vol. MTT-37, No. 4, 776-786, Apr. 1989.
7. Ali, S. M., T. M. Habashy, and J. A. Kong, "Dyadic Green's functions for multilayered uniaxially anisotropic media," submitted for publication.
8. Chew, W. C., and T. M. Habashy, "The use of vector transforms in solving some electromagnetic scattering problems," *IEEE Trans. Antennas Propagat.*, Vol. AP-34, No. 7, 871-879, July 1986.
9. Fache, N., and D. De Zutter, "Rigorous full-wave space-domain solution for dispersive microstrip lines," *IEEE Trans. Microwave Theory Tech.*, Vol. MTT-36, No. 4, 731-737, Apr. 1988.

Cheung-Wei Lam was born in Hong Kong on March 5, 1965. He received the B.S. degree (1987) in electronics from Chinese University of Hong Kong. In 1989 he obtained his S.M. degree in electrical engineering from the Massachusetts Institute of Technology where he is currently a graduate research assistant working towards the Ph.D degree. His main research interests include full-wave analyses of microstrip structures on anisotropic substrates and application of the finite-difference time-domain method to microstrip problems.

Sami M. Ali was born in Egypt on December 7, 1938. He received the B.Sc. degree from the Military Technical College, Cairo, Egypt, in 1965, and the Ph.D. degree from the Technical University of Prague, Prague, Czechoslovakia, in 1975, both in electrical engineering. In 1975 he joined the Department of Electrical Engineering, Military Technical College, Cairo. He spent the 1981-1982 academic year as a visiting scientist at the Research Laboratory of Electronics, MIT, Cambridge, Massachusetts. In 1985, he became a Professor and head of the Basic Electrical Engineering Department, Military Technical College, Cairo, Egypt. Since 1987, he is a visiting scientist at the Research Laboratory of Electronics, MIT, Cambridge, Massachusetts. His current research interests deal with microwave integrated circuits and microstrip antenna applications. He is currently serving as a member of the International Advisory Board of the book series *Progress in Electromagnetics Research*, published by Elsevier.

J. A. Kong is Professor of Electrical Engineering and Chairman of Area IV on Energy and Electromagnetic Systems in the Department of Electrical Engineering and Computer Science at the Massachusetts Institute of Technology in Cambridge, Massachusetts. His research interest is in the field of electromagnetic wave theory and applications. He has published 6 books and over 200 refereed journal and conference papers, and is the Editor of the Wiley Series in Remote Sensing, and Chief Editor of the Elsevier book series of *Progress In Electromagnetics Research (PIER)*.

# ELECTROMAGNETIC RADIATION FROM A VLSI PACKAGE AND HEATSINK CONFIGURATION

C.F. Lee\*, K. Li, S.Y. Poh†, R.T. Shin, and J.A. Kong

Department of Electrical Engineering and Computer Science  
and Research Laboratory of Electronics  
Massachusetts Institute of Technology  
Cambridge, MA 02139

†Physical Technology Group  
Digital Equipment Corporation  
Andover, MA 01810

## Abstract

The electromagnetic radiation from a VLSI chip package and heatsink structure is analysed by means of the finite-difference time-domain (FD-TD) method. The FD-TD algorithm implemented incorporates a multi-zone gridding scheme to accommodate fine grid cells in the vicinity of the heatsink and package cavity and sparse gridding in the remainder of the computational domain. The issues pertaining to the effects of the heatsink in influencing the overall radiating capacity of the configuration are addressed. Analyses are facilitated by using simplified heatsink models and by using dipole elements as sources of electromagnetic energy to model the VLSI chip. The potential for enhancement of spurious emissions by the heatsink structure is illustrated. For heatsinks of typical dimensions, resonance is possible within the low gigahertz frequency range. The potential exploitation of the heatsink as an emissions shield by appropriate implementation schemes is discussed and evaluated.

## Introduction

The extension of regulatory electromagnetic emissions test limits to the gigahertz range of frequencies for high performance computing equipment has necessitated caution in the design and implementation of components down to the VLSI chip package level for computing systems. At issue is the avoidance of potentially efficient radiators at the design and development phase. The objective is to minimize the need for cost prohibitive corrective measures commonly invoked in reaction to problems encountered in tests on assembled systems.

In this paper, the effects of a heatsink over a chip package on the electromagnetic emissions characteristics of the chip and package environment are addressed. Such an interest is justified by the following reasons. First, the heatsink is typically metallic and is in close proximity to a major energy source — the chip. Also, the electrical dimensions of the structure are comparable to the wavelengths of concern. Finally, in light of the ever-increasing power levels of high performance integrated circuitry, the heatsink is an indispensable component of the VLSI chip packaging configuration. The objectives are to identify and quantify the effects of the heatsink on the radiating properties of the package structure; to understand and exploit the radiation mechanisms; and to evaluate viable heatsink implementation schemes for minimizing the overall radiating capacity.

## Problem Configuration and Model

The electromagnetic radiation properties of a heatsink and integrated circuit (IC) package configuration are analysed by means of suitable models. A typical heatsink/package configuration of interest is shown in Figure 1. The heatsink may be modeled as a perfectly conducting rectangular slab positioned over a finite-size dielectric medium representing the chip package. The chip is supported in turn by a dielectric layer of infinite extent over an infinite ground plane which models the substrate or printed wiring board (PWB) with (at least) one reference layer. The electromagnetic sources used to model the active chip include electric and magnetic dipoles of vertical and horizontal orientation positioned on the package/substrate dielectric interface. The resulting model of an electromagnetically-coupled slab structure is shown in Figure 2. The generation of a model with reduced complexity for both source and heatsink is to facilitate the interpretation of results based on underlying physics. The extension to more complex heatsink (e.g., finned) and source models may be readily accomplished with the rectangular gridding scheme associated with the numerical solution employed. With sufficiently fine grids, circular heatsinks may also be adequately modeled. In addition, the models are modified to reflect alternate implementation schemes for emissions suppression purposes in order to conduct quantitative analyses. Field strengths and radiated powers are computed for quantitative analysis and evaluation.

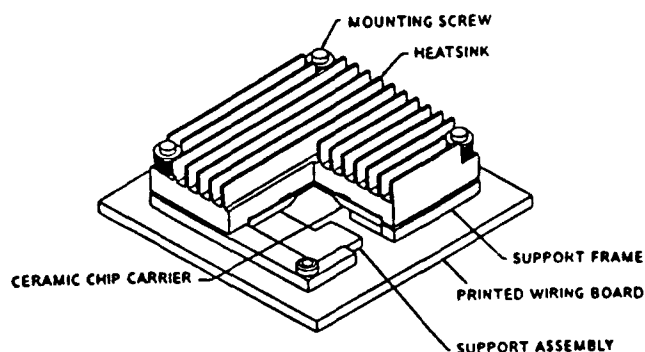


Figure 1. Cutaway view of a VLSI package/heatsink configuration.

\* Current address: WAVETRACER, Acton, MA 01720.

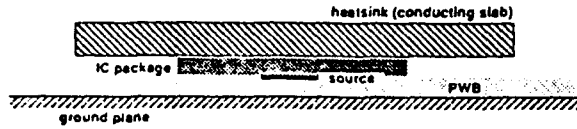


Figure 2. Cross-sectional view of simplified package/heatsink model.

### Method of Solution

The method employed in the analysis is the *finite-difference time-domain* (FD-TD) technique. It is based on the discretization of the electric and magnetic fields over rectangular grids together with the finite difference approximation of the spatial and temporal derivatives appearing in the differential form of Maxwell's equations. The reasons for which the FD-TD methodology was selected include the relative ease of implementation for complicated geometries, the requirement of only simple arithmetic operations in the solution process, and the flexibility for time- and frequency-domain analyses.

In the FD-TD technique, a computational domain is first defined and divided into rectangular cells. Electric and magnetic fields are spatially discretized in a staggered manner [1] as shown in Figure 3. Electric fields are assigned to half-integer  $(n + 1/2)$  time steps and magnetic fields are assigned to integer  $(n)$  time steps for the temporal discretization of fields. Next, the spatial and temporal derivatives of the two Maxwell's curl equations are approximated using center differences. Maxwell's curl equations for a time- and frequency-invariant medium are:

$$\nabla \times \vec{H} = \sigma_e \vec{E} + \epsilon_e \epsilon_r \frac{\partial \vec{E}}{\partial t}, \quad \nabla \times \vec{E} = -\mu_o \mu_r \frac{\partial \vec{H}}{\partial t},$$

where  $\epsilon_o$  is the free-space permittivity,  $8.854 \times 10^{-12}$  F/m and  $\mu_o$  is the free-space permeability,  $4\pi \times 10^{-7}$  H/m. In addition,  $\epsilon_r$  and  $\mu_r$  are respectively the relative permittivity (dielectric constant) and relative permeability of the medium; while  $\sigma_e$  is the electric conductivity. Maxwell's divergence equations are ignored since the curl equations with appropriate boundary conditions uniquely determine the solution. In rectilinear coordinates, the curl equations are rewritten as:

$$\begin{aligned} \frac{\partial H_x}{\partial y} - \frac{\partial H_y}{\partial x} &= \sigma_e E_z + \epsilon_e \epsilon_r \frac{\partial E_z}{\partial t}; & \frac{\partial E_x}{\partial y} - \frac{\partial E_y}{\partial x} &= -\mu_r \mu_o \frac{\partial H_z}{\partial t} \\ \frac{\partial H_x}{\partial z} - \frac{\partial H_z}{\partial x} &= \sigma_e E_y + \epsilon_e \epsilon_r \frac{\partial E_y}{\partial t}; & \frac{\partial E_x}{\partial z} - \frac{\partial E_z}{\partial x} &= -\mu_r \mu_o \frac{\partial H_y}{\partial t} \\ \frac{\partial H_y}{\partial z} - \frac{\partial H_z}{\partial y} &= \sigma_e E_x + \epsilon_e \epsilon_r \frac{\partial E_x}{\partial t}; & \frac{\partial E_y}{\partial z} - \frac{\partial E_z}{\partial y} &= -\mu_r \mu_o \frac{\partial H_x}{\partial t} \end{aligned}$$

Difference equations are derived from these six equations by applying center differencing. For example, the expression relating  $H_x$  to  $E_y$  and  $E_z$  at time  $(n + 1/2)\Delta t$  is given by:

$$\begin{aligned} \frac{E_{x(i,j,k)}^{n+1/2} - E_{x(i,j,k)}^{n+1/2}}{\Delta y} - \frac{E_{y(i,j,k+1)}^{n+1/2} - E_{y(i,j,k)}^{n+1/2}}{\Delta z} \\ = -\mu_r \mu_o \frac{H_{x(i,j,k)}^{n+1} - H_{x(i,j,k)}^n}{\Delta t} \end{aligned}$$

The center difference ensures that the spatial and temporal discretizations are of second order where errors are proportional to the square of the cell size and time increment. Finally, with appropriate initial and boundary conditions, the solutions to the difference equations are obtained through explicit leapfrog time marching. This corresponds to alternating the advance of

electric and magnetic fields. To achieve accurate results, the cell sizes are taken to be a fraction of the smallest wavelength. The time increment and the cell size are related by the stability criterion [2],

$$\Delta t \leq \frac{1}{c_o \sqrt{(1/\Delta x)^2 + (1/\Delta y)^2 + (1/\Delta z)^2}}$$

where  $c_o$  is the speed of light in free space. Fields are set to be zero initially everywhere to satisfy the causality condition consistent with zero excitation for time less than zero. The boundary conditions are continuity of tangential electric and magnetic fields on material interfaces, vanishing tangential electric fields on perfect conductors, and the absorbing boundary conditions on the boundary of the computational domain. The absorbing boundary conditions [3] are used to limit the computational domain by simulating unbounded space. The minimum distance to the absorbing boundary, i.e., computational boundary, from the heatsink is determined by consideration of reflection error, computation time, and memory. For a given cell size, the reflection error decreases but the computation time increases substantially with increasing distance to the boundary.

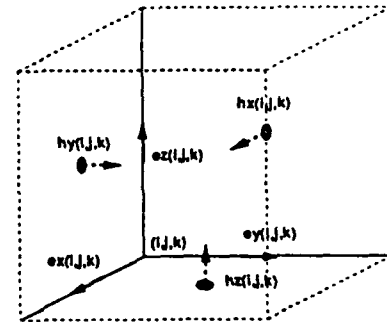


Figure 3. Staggered rectangular grid on typical unit cell in computational domain.

The size of the discretization cells should be reasonably small in order to model features of the heatsink and capture correct field variations. On the other hand, since the heatsink should not be too close to the computational boundary, the cell count is highest outside the heatsink when a small cell size is used. To avoid the excessive number of cells which would otherwise be generated, a three-zone gridding scheme [4] is used (Figure 4). The first zone contains the heatsink and dipole source; it has the finest grid among the three zones. The second zone has the same height as the first and extends horizontally from the heatsink to the outer boundary of the computational domain. The cell size of this zone has the same vertical dimension as those of the first zone; while the horizontal dimensions may be a few times larger than the first zone. The remainder of the computational domain belongs to the third zone. The horizontal dimensions of the cells are identical to those of the second zone, and the vertical dimension of the cells may be a few times larger than the first or second zones. Fields at nodes on an interface between two zones are calculated via a combination of parabolic curve fitting and linear interpolation. For example, in Figure 5, the partial derivative of  $H_y$  with respect to the vertical direction  $z$  at position of  $E_{x(i,j,k)}$  at the  $n$ th time step is given by

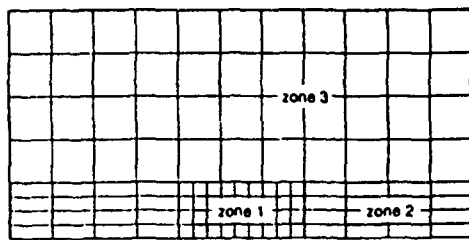


Figure 4. A three-zone gridding scheme for multi-zone gridding. The heatsink is in zone 1.

$$\begin{aligned} \left. \frac{\partial H_y}{\partial z} \right|_{E_{\theta(i,j,k)}}^n &\approx \frac{8}{\Delta(1+a)(3+a)} H_{y(i,j,k)}^n \\ &+ \frac{a-3}{\Delta(1+a)} H_{y(i,j,k-1)}^n \\ &+ \frac{1-a}{\Delta(3+a)} H_{y(i,j,k-2)}^n \\ &+ \frac{4a^3 + 13a^2 - 9}{24(a+1)(a+3)} \Delta^2 \left. \frac{\partial^3 H_y}{\partial z^3} \right|_{E_{\theta(i,j,k)}}^n \end{aligned}$$

Second order accuracy is therefore maintained everywhere. Although the discretization scheme is second order everywhere, the proportionality constants for the discretization errors are different due to different cell sizes. Reasonable accuracy is maintained due to the fact that the spatial variation of the fields outside the first zone is relatively small and that all cell sizes remain a fraction of the smallest wavelength. The size of the time step is primarily determined by the smallest grid size. For simplicity, the variable time step implementation [5] is not used.

The fields beyond the computational domain are calculated using Huygens' principle [6]. The post-processing of full time domain information for the purpose of generating frequency domain data is expensive in storage and is inefficient. The fields are instead calculated at selected multiple frequencies. To obtain multi-frequency data, the time waveforms of the dipole excitations are chosen to be modulated Gaussian pulses, i.e.,  $\approx \cos(\omega_0(t - t_0)) \exp[-((t - t_0)/T)^2]$ , where  $\omega_0$  is the center frequency of the excitation,  $t_0$  is the delay, and  $T$  determines the pulse-width. Complex amplitudes at each frequency are calculated simultaneously on a selected surface outside the first zone using the discrete Fourier transform.

### Results and Discussion

The basic model described in Figure 2 is analysed with the use of horizontal electric and magnetic dipoles and vertical electric and magnetic dipoles as sources. The choice of such elements circumvents the problem of deriving a rigorous model for the VLSI circuitry as an electromagnetic source and eliminates factors which may otherwise clutter the understanding and interpretation of the physical processes associated with the spurious radiation study. Of these sources only the horizontal magnetic dipole (HMD) and vertical electric dipole (VED) show radiation enhancement in the presence of the heatsink. The frequency range considered does not exceed 10 GHz. The dominant horizontal (electric field) polarization generated by the other 2 sources remains below cutoff within this frequency

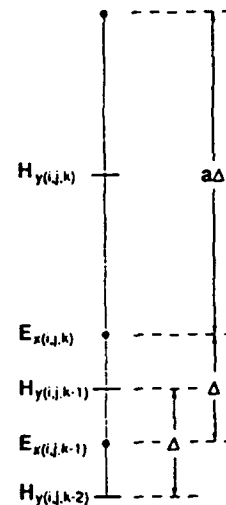


Figure 5. Node and field designations for multi-zone gridding in vertical direction.

range and for the typical dimensions considered. Both classes of sources may be found in VLSI package configurations — the VED in the form of vias and pins and the HMD as vertically stratified signal and return paths. Results and discussions will focus on one or both of the VED, HMD sources. Unless stated otherwise, the dimensions of the conducting slab are 4.8 cm square and 2.5 mm thick. Its lower surface is located 7.5 mm above a lower ground or reference plane. In the results presented, the effects of the dielectric layers are not considered. The dipole sources are located at the nodes closest to the center of the heatsink-ground plane cavity.

Figure 6 compares the normalized radiated power of an HMD over a ground plane in the presence and absence of a heatsink for a frequency range of 1 to 6.5 GHz. Normalization is with respect to the total radiated power of an identical dipole in unbounded space. The resonant behavior around 2.4 and 5.5 GHz in the presence of the heatsink is evident, with the first resonance showing a significant enhancement of radiation over the case without the heatsink. This resonance feature is illustrated in Figure 7 where the time response of the vertical E-field at the indicated location on the periphery of the heatsink-ground plane cavity is shown. The oscillations at the resonant frequency become increasingly evident after 700 time-steps. The quality factor (Q) of the structure may also be deduced from the decay rate and the resonant frequency. Figure 8 shows the surface plots of the vertical electric field amplitudes over a horizontal plane that traverses the heatsink and ground plane cavity and spanning the computational domain at 4 different time steps. Each plot is normalized to the maximum value for the respective time step. The absence of any obvious reflected disturbances from the edges of the computational domain illustrates the efficiency of the absorbing boundary condition. The sustained resonant mode pattern is evident after 1000 time steps.

Figure 9 shows the corresponding results over the frequency range of 1 to 8 GHz with a VED as the source. Again, substantial enhancement in radiated power in the presence of a heatsink occurs at the primary resonance of 4.8 GHz, and at the second resonance near 7 GHz. The symmetry and anti-symmetry of the dipole source fields are responsible for the difference in excited resonances with the HMD and VED dipoles.

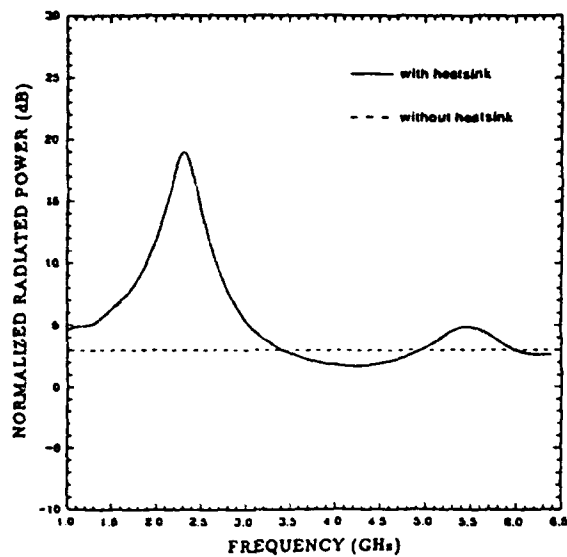


Figure 6. Comparison of normalized total radiated power in presence and absence of a heatsink with a HMD source. Source function  $\sim \cos(\omega_0(t - t_0)) \exp[-((t - t_0)/T)^2]$ , where  $\omega_0 = 5\pi \times 10^9$  rad/s,  $t_0 = 4T = 0.8$  ns.

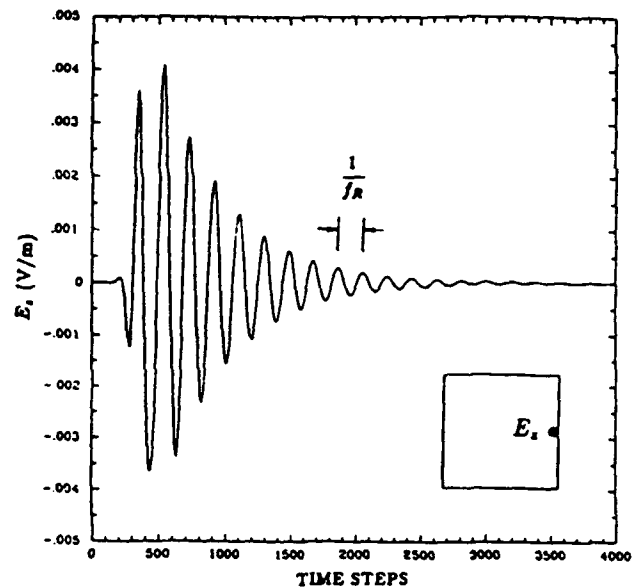


Figure 7. Time response of vertical electric field at indicated position on the boundary of heatsink and ground plane cavity for HMD source of Figure 6. Each time step corresponds approximately to 2.2 picoseconds.  $f_R = 2.3$  GHz.

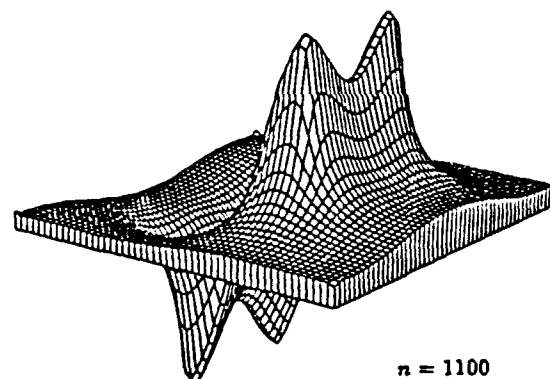
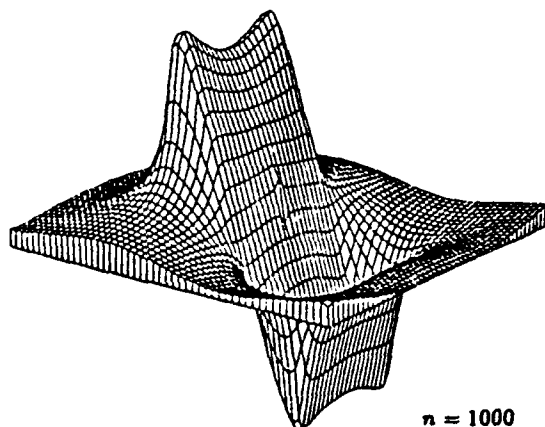
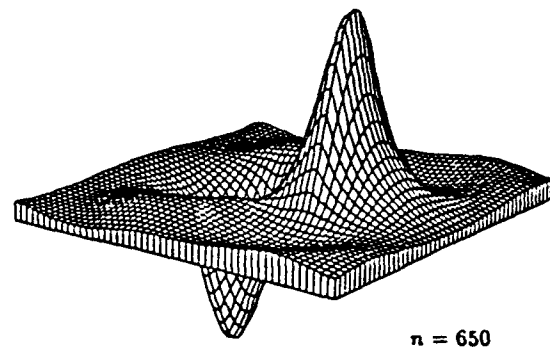
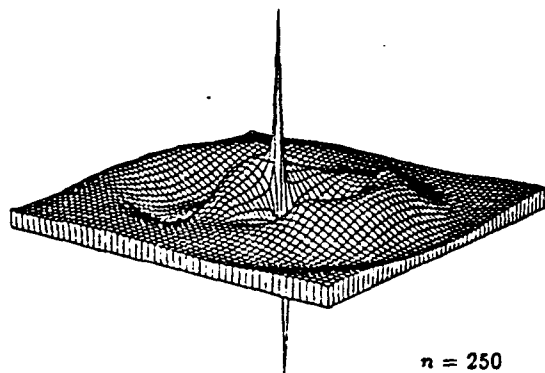


Figure 8. Vertical electric field amplitude plots over horizontal plane through heatsink/ground plane cavity for HMD source of Figure 6.  $n$  is the number of time steps elapsed, and each time step corresponds approximately to 2.2 picoseconds.

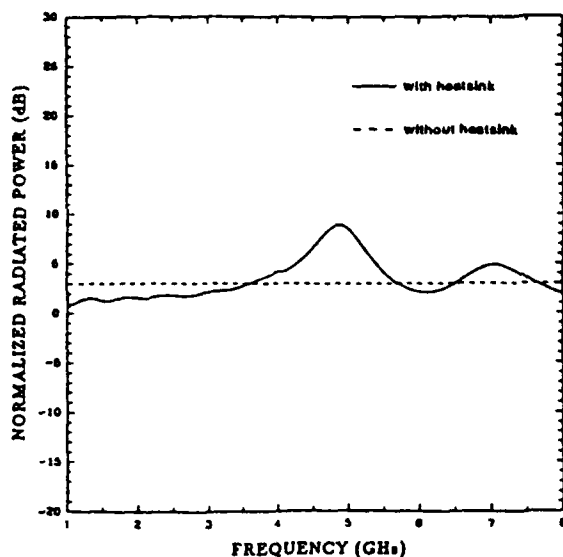


Figure 9. Comparison of normalized total radiated power in presence and absence of heatsink with an VED source. Source function  $\sim \cos(\omega_0(t - t_0)) \exp[-((t - t_0)/T)^2]$ , where  $\omega_0 = 5\pi \times 10^9$  rad/s,  $t_0 = 4T = 0.8$  ns.

Although modeled so far as a suspended slab of conducting material, the heatsink may also be supported by posts (e.g., Figure 1) which may or may not be connected to any other conducting paths. In Figure 10 we show the model of a heatsink supported with 4 posts, of 4 mm square cross-section, connected to a reference or ground plane. We also investigate the effect of increasing the number of the posts as a means of exploiting the heatsink as an emissions shield through appropriate implementation. This is particularly pertinent in light of the observation of radiation enhancement by the indispensable heatsink. The rationale for consideration of such posts is the reduction in the size of the wavelengths allowed to leak through the smaller gaps, whose effectiveness is weakened by the interaction between the resulting multiple gaps.

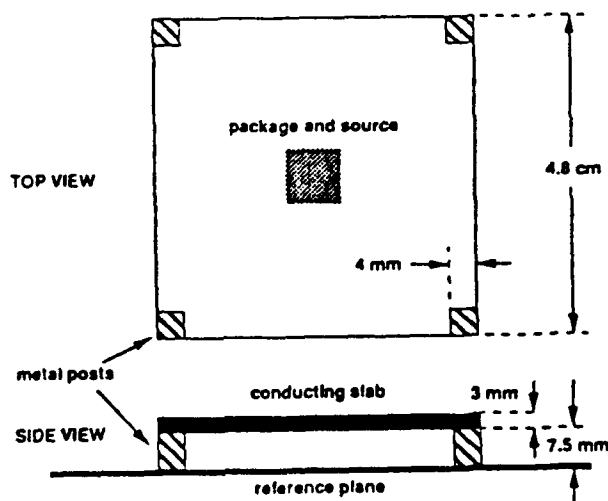


Figure 10. Model for heatsink with 4 support posts connected to reference plane.

Figure 11 shows the effects of the implementation of 4 or 8 uniformly distributed posts on the radiated power. The dipole source is a HMD. The figure shows the typical effects of adding posts — the shifting of resonant frequencies upwards which also renders the resulting configuration to be of lower Q. In implementing such an option for emissions suppression, care has to be taken to ensure that such shifts move the resonant frequencies beyond the range of test frequencies.

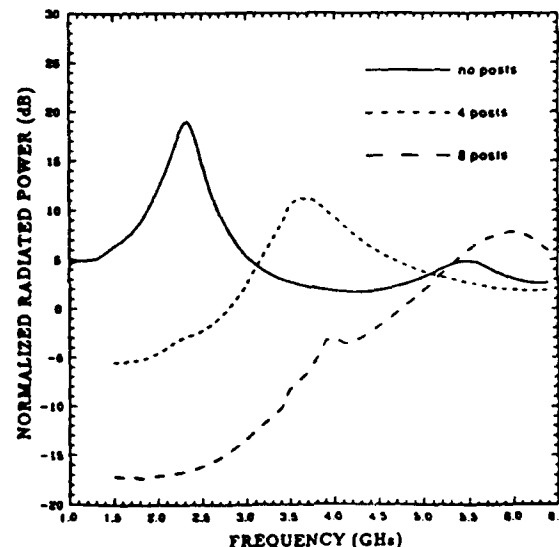


Figure 11. Comparison of normalized total radiated power with HMD source for heatsink with 4 and 8 posts and without posts.

Another potential means of exploiting the heatsink for emissions suppression is to employ a skirt of conducting material beneath and around the periphery of the heatsink, thereby serving as a compliant containment which would dissipate the contained energy with its finite conductivity. Figure 12 shows the model considered. The gaps in the gasket material are to facilitate lead passage. The simulation results, comparing radiation from a gasketed and ungasketed heatsink with an HMD as source, are shown in Figure 13 where a conductivity of 10 mhos/m, a dielectric constant of 4, and a thickness of approximately 7.5 mm are assumed for the gasket material. This conductivity is conservative since typical bulk conductivities for conductive gasket material are of the order of  $10^4$  mhos/m. Despite the conservative estimate on the conductivity of a typical material, the improvement in emissions reduction near resonance is substantial, although the lower Q that results may tend to raise emission levels at nearby frequencies. For reference, the size of the skin depth at 1 GHz for the conductivity assumed is approximately 5 mm and will decrease as the square-root of the frequency. The frequency response indicates a slight downward shift in the resonant frequency due to an effectively denser dielectric medium beneath the heatsink and a broader bandwidth corresponding to a lowered Q due to added energy dissipation in the gasket material.



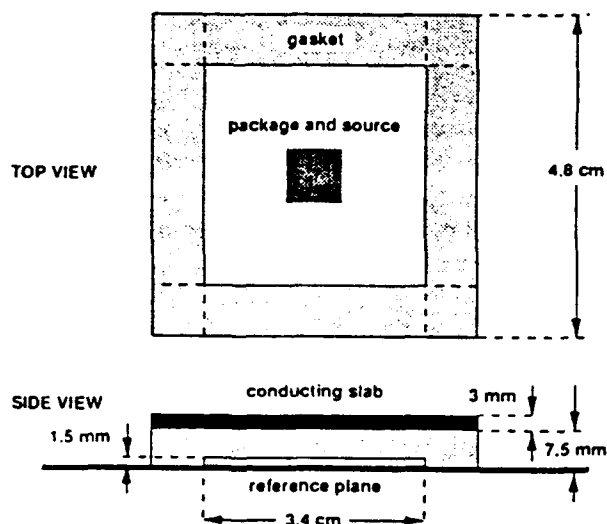


Figure 12. Model for heatsink with a conducting gasket.

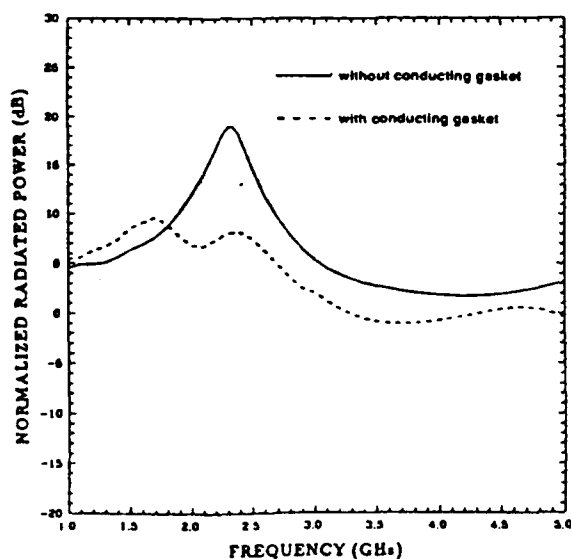


Figure 13. Comparison of normalized total radiated power with HMD source for heatsink with and without gasketing.

For the purpose of suppressing emissions, exclusive usage of posts appears viable if the resonant frequencies may be shifted beyond the frequency range of concern. The use of gaskets results in slightly lower resonant frequencies with broader frequency responses. This spreads the resonance effect over a broader frequency range, albeit at lower amplitudes. A recommendation would be to use a combination of the gasketing and multiple posts schemes. The shielding performance of conductive gaskets are expected to improve at higher frequencies to which multiple posts shift the resonant frequencies of concern.

## Conclusion

The FD-TD technique has been applied to the analyses of the radiation from a VLSI heatsink and package configuration. The technique was chosen for its flexibility in treating this class of problems involving potentially complex configurations where neither approximate nor analytical methods are practical. The multi-zone gridding scheme implemented allowed a high grid resolution in the vicinity of the heatsink without sacrificing overall cell number thereby allowing increased numerical efficiency for low frequencies. Additional advantages of this discretization scheme include improved geometrical and material modeling. The analysis of the heatsink, a critical component within the computer packaging environment, illustrated the significance of resonance due to appreciable electrical dimensions on the spurious electromagnetic radiation from the VLSI packaging environment. Simulations with typical heatsinks dimensions showed the occurrence of resonance in the low gigahertz range. The effects of the presence of a heatsink on the radiation properties of dipole models have been explained and the features of resonant behavior presented. The effectiveness and consequences of exploiting practical heatsink implementation options such as grounding and shielding to reduce electromagnetic emissions has been discussed and quantified using the FD-TD numerical technique.

## Acknowledgment

The authors thank Donald Vonada of Digital Equipment Corporation for his support and interest.

## References

- [1] Yee, K.S., "Numerical solution of initial boundary value problems involving Maxwell's equations in isotropic media," *IEEE Trans. Antennas Propagat.*, AP-14, 302-307, May 1966.
- [2] Taflov, A., and M.E. Brodwin, "Numerical solution of steady-state electromagnetic scattering problems using the time-dependent Maxwell's equations," *IEEE Trans. Microwave Theory Tech.*, MTT-23, 623-630, Aug. 1975.
- [3] Mur, G., "Absorbing boundary conditions for the finite difference approximation of the time domain electromagnetic field equations," *IEEE Trans. Electromagn. Compat.*, EMC-23, 377-382, Nov. 1981.
- [4] Lee, C.F., *Finite Difference Method For Electromagnetic Scattering Problems*, Ph.D. Thesis, Dept. of EECS, MIT, Cambridge, MA, June 1990.
- [5] Fusco, M., "FDTD algorithm in curvilinear coordinates," *IEEE Trans. Antennas Propagat.*, AP-38, 76-89, Jan. 1990.
- [6] Kong, J.A., *Electromagnetic Wave Theory*, Wiley-Interscience, New York, 1986.

## Electromagnetic calculation of soft x-ray diffraction from 0.1 $\mu\text{m}$ -scale gold structures

M. L. Schattenburg

*Center for Space Research, Massachusetts Institute of Technology,  
77 Massachusetts Avenue, Cambridge, MA 02139, USA*

K. Li, R. T. Shin, J. A. Kong, D. B. Olsier, and Henry I. Smith

*Research Laboratory of Electronics, Massachusetts Institute of  
Technology, 77 Massachusetts Avenue, Cambridge, MA 02139, USA*

Because the effects of diffraction during proximity-print x-ray lithography are of critical importance, a number of previous researchers have attempted to calculate the diffraction patterns and minimum achievable feature sizes as a function of wavelength and gap. Work to date has assumed that scalar diffraction theory is applicable—as calculated, for example, by the Rayleigh-Sommerfeld formulation—and that Kirchhoff boundary conditions can be applied. Kirchhoff boundary conditions assume that the fields (amplitude and phase) are constant in the open regions between absorbers, and a different constant in regions just under the absorbers (i.e., that there are no fringing fields). An x-ray absorber is, however, best described as a lossy dielectric that is tens or hundreds of wavelengths tall, and hence Kirchhoff boundary conditions are unsuitable. In this report we use two numerical techniques to calculate (on a Cray 2 supercomputer) accurate diffracted fields from gold absorbers for two cases: a 30 nm-wide line at  $\lambda = 4.5$  nm, and a 100 nm-wide line at  $\lambda = 1.3$  nm. We show that the use of Kirchhoff boundary conditions introduces unphysically high spatial frequencies into the diffracted fields. The suppression of these frequencies—which occurs naturally without the need to introduce an extended source or broad spectrum—improves exposure latitude for mask features near 0.1  $\mu\text{m}$  and below.

## I. INTRODUCTION

The limits and practicality of proximity-print x-ray lithography continues to be a topic of discussion and debate. Of particular concern are the limits of resolution imposed by the effects of diffraction. Because the mechanical limits imposed on the mask-substrate gap during the volume manufacturing of ULSI circuits are not presently certain, it remains prudent to ask: what is the minimum practical feature size that can be printed at a given gap?

In order to resolve these issues, a series of papers have appeared in the literature which present theoretical calculations for the diffraction of x rays from mask absorbers. Early papers simply considered absorption [1-3], but later papers also included the effects of phase-shift [4-8]. Most recently, authors have included the effects of source spatial and temporal coherence, and have generated exposure "trees" which allow the determination of exposure latitude versus gap for various types of mask features [9-15].

The method most commonly used to calculate the diffraction pattern is to apply a Fresnel-Kirchhoff or Rayleigh-Sommerfeld diffraction integral [16,17], or a more sophisticated formulation (Hopkin's formula) which takes into account source partial coherence [18]. These calculations can be carried out either in the spatial or the spatial-frequency domain. In any of these cases, approximate boundary conditions known as Kirchhoff boundary conditions (KBC) are generally applied. KBC assume that the field (amplitude and phase) is constant in the open regions between absorbers, and also constant (but attenuated and phase shifted) in regions just under the absorbers—in other words, that there are no fringing fields at the boundary between the two regions.

In general, KBC apply when the wavelength,  $\lambda$ , is much smaller than the lateral size,  $d$ , of the feature being printed—which is the case in most x-ray lithography (e.g.,  $d = 0.1 \mu\text{m}$ ,  $\lambda = 1 \text{ nm}$ ). However, what is not generally recognized is that KBC will not necessarily apply when the absorbers are lossy dielectrics that are tens or hundreds of wavelengths tall.

Work to date concerning the printability of  $0.25 \mu\text{m}$  features is probably reasonably accurate. However, in this report we show that the assumption of KBC for features near  $0.1 \mu\text{m}$  and below is not tenable. In particular, we show that the suppression of the undesirable high-spatial-frequency components—

which some authors note an extended source and/or a broad spectrum achieves—occurs naturally in the absorber due to the “lossy dielectric” effect.

## II. CALCULATIONS

We used two different methods to calculate the diffraction from gold absorbers: the Method of Moments (MoM) and the Finite Difference-Time Domain (FD-TD) method. (We used two algorithms in order to check for consistency.) The only approximations inherent in these methods are in the discretization of the object space and Maxwell’s equations. Because the discretization can be performed on a scale that is small compared to the wavelength, and furthermore the discretization scale can be reduced until convergence is achieved, accuracy is assured.

Of these two techniques, the MoM is typically faster and uses less memory for single-frequency calculations. On the other hand, the FD-TD method is simpler to code and therefore less likely to have errors. In practice we ran small test cases using both methods and then increased the spatial resolution (reduced discretization scale) until both methods converged to the same solution. Then the computationally-intensive cases reported here were calculated with the MoM.

### A. METHOD OF MOMENTS

The Method of Moments (MoM) is a numerical technique useful in the solution of steady-state electromagnetic wave scattering and radiation problems [19,20]. The method calculates steady-state fields on the surface of a closed dielectric object in free space, which is impinged upon by a known exciting wave. The surface of the object is broken up into small patches which are small compared to the wavelength. The surface currents at each patch and thus the tangential surface fields are then calculated. Computation time was up to two hours on a Cray 2. Once the fields are known on the boundary of the object they can readily be propagated to any desired point or plane [16,17].

## B. FINITE DIFFERENCE-TIME DOMAIN METHOD

The Finite Difference-Time Domain (FD-TD) method is a numerical technique useful in the solution of time-dependent electromagnetic wave scattering and radiation problems [21-24]. The method involves the formation of a computational domain which encompasses the object of interest and is typically several times larger. The entire domain inside the boundary—including the object—is discretized on a rectangular grid. The spacing between adjacent nodes on the grid is small compared to the wavelength. A clock is started and incremented in time steps that are small compared to the light-travel time between adjacent nodes. Then discretized forms of Maxwell's equations are used to calculate the fields at each node from the fields at nearby nodes which were in effect at the previous time step. Absorbing boundary conditions are imposed at the edges of the computational domain in order to simulate unbounded space. Also, a boundary condition is typically imposed on a surface surrounding the object to simulate an incoming plane wave. The result can be displayed as a video image of the fields inside the domain. Computation time was up to one hour on a Cray 2. In practice the calculation is run until steady state is achieved, and the fields at nodes along a line just under the absorber are saved for comparison with the MoM results.

## III. RESULTS

Calculations were performed using MoM and FD-TD on single gold parallelepiped absorbers, infinite in length and rectangular in cross-section, which were impinged upon by a monochromatic plane wave. The electric-field polarization was used (E-field perpendicular to the page). (The magnetic-field polarization yielded results similar to the electric-field polarization.) These were compared to the results of a Rayleigh-Sommerfeld-Kirchhoff (RSK) calculation [16]. We considered two cases (see Table I), which were selected in order to explore a range of spatial frequencies: Case 1, which is a 30x100 nm absorber with the 4.5 nm ( $C_K$ ) x ray, and Case 2, which is a 100x250 nm absorber with the 1.3 nm ( $Cu_L$ ) x ray. Note that the attenuation of the absorber in both cases is roughly equivalent. (~12 dB).

#### A. CASE 1 ( $\lambda = 4.5$ nm)

Figs. 1 (a) to (d) show the resulting intensities or irradiance distributions for both the MoM and RSK methods calculated for  $\alpha$  from 0-1.5 (gap  $G$  from 0-0.3  $\mu\text{m}$ ). Here  $\alpha$  is a dimensionless gap given by  $\alpha = G\lambda/W^2$ , where  $G$  is the gap,  $\lambda$  is the wavelength, and  $W$  is the linewidth. Note the suppression of high spatial frequencies in the MoM calculation, and the "fuzzy edge" of a few tens of nanometers in extent. Figs. 2 (a) and (b) show the beneficial effects of the suppression of high spatial frequencies on exposure latitude in the form of exposure "trees" [9-12] which plot  $\pm 10$  % linewidth contours versus  $\alpha$ . Here we have used a line bias of 33 % (40 nm resist line). (A line bias is the use of a smaller-than-desired feature size in the mask than on the wafer in order to compensate for diffractive broadening.) An enlightening way to view the suppression of high spatial frequencies is to plot the intensity of the waves at  $\alpha = 0$  (gap  $G = 0$ ) as a function of spatial frequency, as shown in Fig. 3. Note that at low spatial frequencies the RSK and MoM calculations agree, but the MoM calculation "rolls off" at around  $0.05 \text{ nm}^{-1}$ .

#### B. CASE 2 ( $\lambda = 1.3$ nm)

The results for the intensities versus  $\alpha$  for Case 2 are shown in Figs. 4 (a) to (d). Note that even though the wavelength is much smaller, the "fuzzy edge" length is roughly the same—a few tens of nanometers. This may be due to the smaller wavelength ( $3.3\times$  smaller) being partially compensated by a taller absorber ( $2.5\times$  taller). The exposure trees are shown in Figs. 5 (a) and (b). Here we have used a line bias of 50% (150 nm resist line). The intensity versus spatial frequency is shown in Fig. 6. Note that the roll-off in this case is still around  $0.05 \text{ nm}^{-1}$ , but that this represents a higher spatial frequency *relative* to the information content in the larger-line/smaller-wavelength case.

### IV. CONCLUSION

We have shown that the use of Kirchhoff boundary conditions introduces unphysically high spatial frequencies into the diffracted fields. The natural suppression of these frequencies by the electromagnetic properties of x-ray

absorbers tremendously improves exposure latitude for mask features near 0.1  $\mu\text{m}$  and below.

## ACKNOWLEDGEMENTS

We would like to thank E. Gullikson, K. Early, and F. Davis for useful discussions. This work was sponsored in part by the National Science Foundation (Grant ECS-8709806), the Office of Naval Research (Contract N00014-90-K-2108), the Joint Services Electronics Program (DAAL03-89-C-0001), and NASA (Contract NAS8-36748).

- 1) K. Heinrich, H. Betz, A. Heuberger, and S. Pongratz, *J. Vac. Sci. Technol.* **19**, 1254 (1981).
- 2) N. Atoda, H. Kawakatsu, H. Tanino, S. Ichimura, M. Hirata, and K. Hoh, *J. Vac. Sci. Technol. B* **1**, 1267 (1983).
- 3) H. Betz, K. Heinrich, A. Heuberger, H. Huber, and H. Oertel, *J. Vac. Sci. Technol. B* **4**, 248 (1986).
- 4) R. Redealli, R. Tatchyn, and P. Pianetta, in *Electron-Beam, X-ray & Ion-Beam Techniques for Submicrometer Lithographies V* (Proc. SPIE **632**), ed. P. D. Blais (SPIE, Bellingham WA), 264 (1986).
- 5) Y. Yamakoshi, H. Atoda, K. Shimizu, T. Sato, and Y. Shimizu, *Appl. Optics* **25**, 928 (1986).
- 6) M. Weiss, H. Oertel, and H.-L. Huber, *Microelec. Engin.* **6**, 265 (1987).
- 7) Y.-C. Ku, E. H. Anderson, M. L. Schattenburg, and Henry I. Smith, *J. Vac. Sci. Technol. B* **6**, 150 (1988).
- 8) S. Hasegawa, J. Itoh, and N. Atoda, *Microelec. Engin.* **8**, 127 (1988).
- 9) B. J. Lin, in *Electron-Beam, X-ray, and Ion-Beam Technology: Submicrometer Lithographies IX* (Proc. SPIE **1263**), ed. D. J. Resnick (SPIE, Bellingham WA, 1990), p. 80.
- 10) B. J. Lin, *Microelec. Engin.* **11**, 137 (1990).
- 11) B. J. Lin, *J. Vac. Sci. Technol. B* **8**, 1539 (1990).
- 12) J. Z. Y. Guo, G. Chen, V. White, P. Anderson, and F. Cerrina, *J. Vac. Sci. Technol. B* **8**, 1551 (1990).
- 13) T. Horiuchi, K. Deguchi, S. Hirota, and A. Yoshikawa, *Microelec. Engin.* **13**, 315 (1991).
- 14) H. K. Oertel, M. Weiß, and H.-L. Huber, *Microelec. Engin.* **13**, 339 (1991).

- 15) Y. Vladimirovsky and J. R. Maldonado, *Microelec. Engin.* **13**, 343 (1991).
- 16) J. W. Goodman, *Introduction to Fourier Optics* (McGraw-Hill, San Francisco, 1968).
- 17) M. Born and E. Wolf, *Principles of Optics, Sixth Edition* (Pergamon, Oxford, 1980), Chap. VIII.
- 18) M. Born and E. Wolf, *ibid.*, Chap. X.
- 19) R. F. Harrington, *Field Computation by Moment Methods* (Macmillan, New York, 1968).
- 20) J. J. H. Wang, *Generalized Moment Methods in Electromagnetics* (Wiley, New York, 1991).
- 21) K. S. Yee, *IEEE Trans. Antennas Propagat.* **AP-14**, 302 (1966).
- 22) A. Taflov and M. E. Brodwin, *IEEE Trans. Microwave Theory Tech.* **MTT-23**, 623 (1975).
- 23) G. Mur, *IEEE Trans. Electromagn. Compat.* **EMC-23**, 377 (1981).
- 24) K. Li, M. A. Tassoudji, R. T. Shin, and J. A. Kong, in *Conference Proceedings of the 7th Annual Review of Progress in Applied Computational Electromagnetics at the Naval Postgraduate School, Monterey, CA, March 18-22, 1991*, ed. F. Walker (The Applied Computational Electromagnetics Society, 1991), p. 38.
- 25) B. L. Henke, P. Lee, T.J. Tanaka, R. L. Shimabukuro, and B. K. Fujikawa, *Atomic Data and Nuclear Data Tables* **27**, 1 (1982); private comm. (1989).

## Figure Captions

- FIG. 1. Intensity vs. lateral position for Case 1. (a)  $\alpha = 0$  (gap = 0), (b)  $\alpha = 0.5$  (gap = 0.1  $\mu\text{m}$ ), (c)  $\alpha = 1.0$  (gap = 0.2  $\mu\text{m}$ ), (d)  $\alpha = 1.5$  (gap = 0.3  $\mu\text{m}$ ).
- FIG. 2. Exposure trees vs.  $\alpha$  (dimensionless gap) for Case 1. (Gaps range from 0-0.3  $\mu\text{m}$ .) The line is biased 33% (40 nm resist line). (a) MoM solution, (b) Rayleigh-Sommerfeld-Kirchhoff approximation.
- FIG. 3. Intensity vs. spatial frequency for Case 1. Note roll-off at 0.05  $\text{nm}^{-1}$ .
- FIG. 4. Intensity vs. lateral position for Case 2. (a)  $\alpha = 0$  (gap = 0), (b)  $\alpha = 0.5$  (gap = 3.7  $\mu\text{m}$ ), (c)  $\alpha = 1.0$  (gap = 7.5  $\mu\text{m}$ ), (d)  $\alpha = 1.5$  (gap = 11.2  $\mu\text{m}$ ).
- FIG. 5. Exposure trees vs.  $\alpha$  (dimensionless gap) for Case 2. (Gaps range from 0-11.2  $\mu\text{m}$ .) The line is biased 50% (150 nm resist line). (a) MoM solution, (b) Rayleigh-Sommerfeld-Kirchhoff approximation.
- FIG. 6. Intensity vs. spatial frequency for Case 2. Note roll-off at 0.05  $\text{nm}^{-1}$ .



TABLE I. Computational cases considered.

	Case 1	Case 2
Wavelength $\lambda$ (nm)	4.48	1.334
Refractive Index [25]	$1 - 7.54 \times 10^{-3} + j1.04 \times 10^{-2}$	$1 - 2.31 \times 10^{-3} + j1.19 \times 10^{-3}$
Width W (nm)	30	100
Height (nm)	100	250
Transmission	0.0541	0.0607
Phase Shift (rad)	1.058	2.72
Patch Size (nm)	$\sim 0.64$	$\sim 0.19$

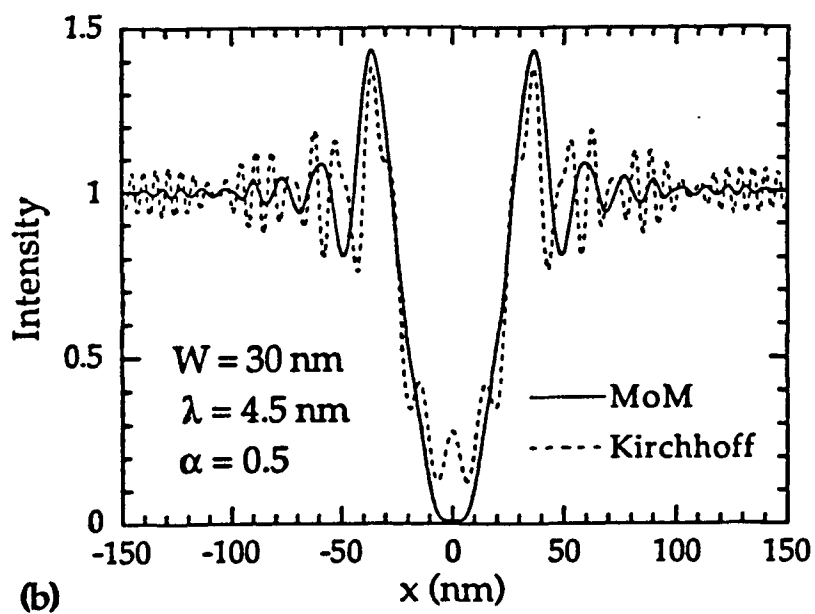
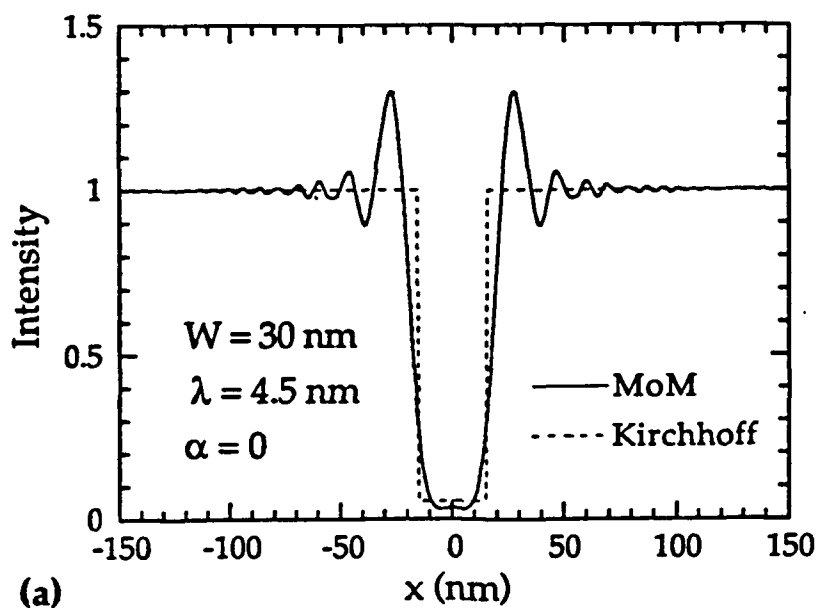


Fig. 1 (a), (b)

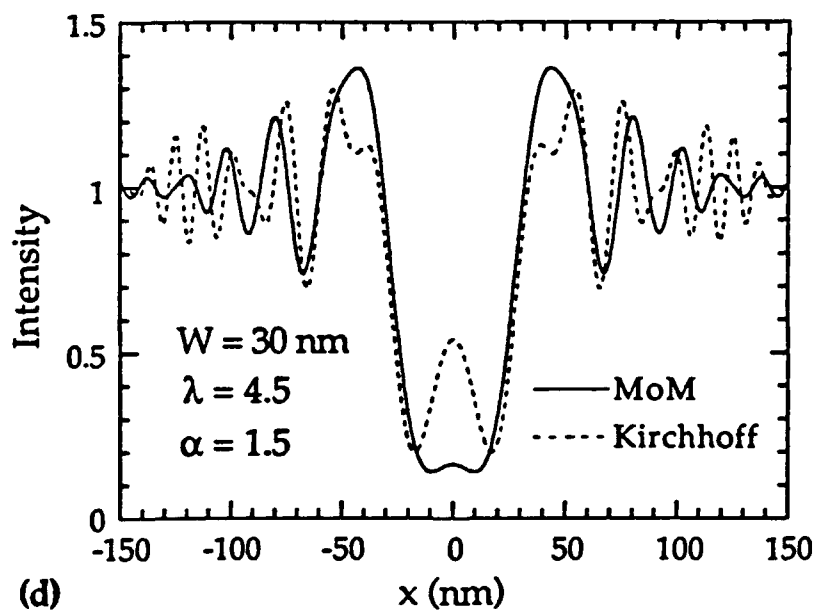
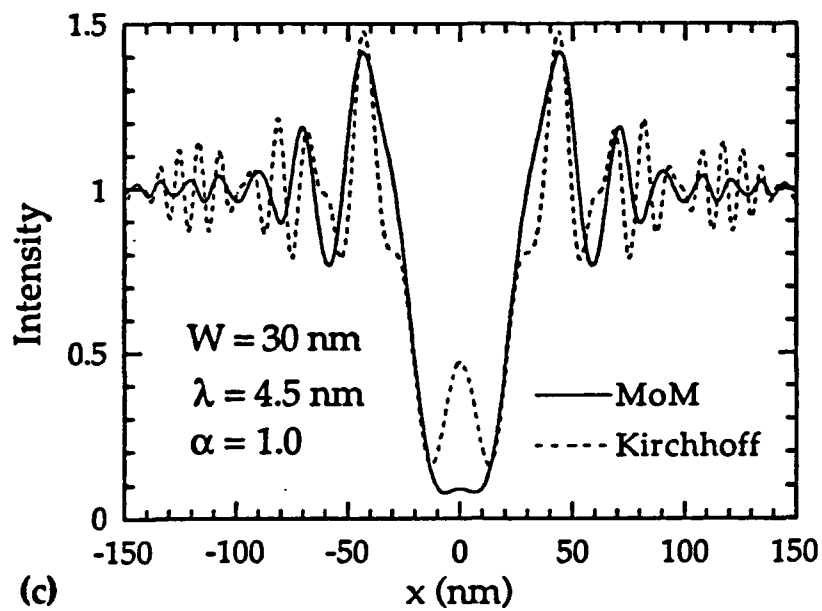


Fig. 1 (c),(d)

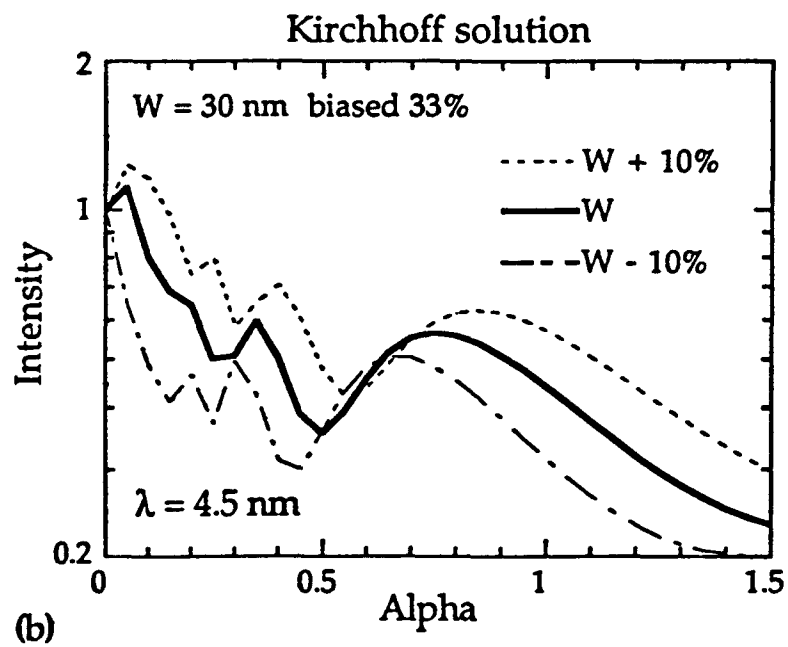
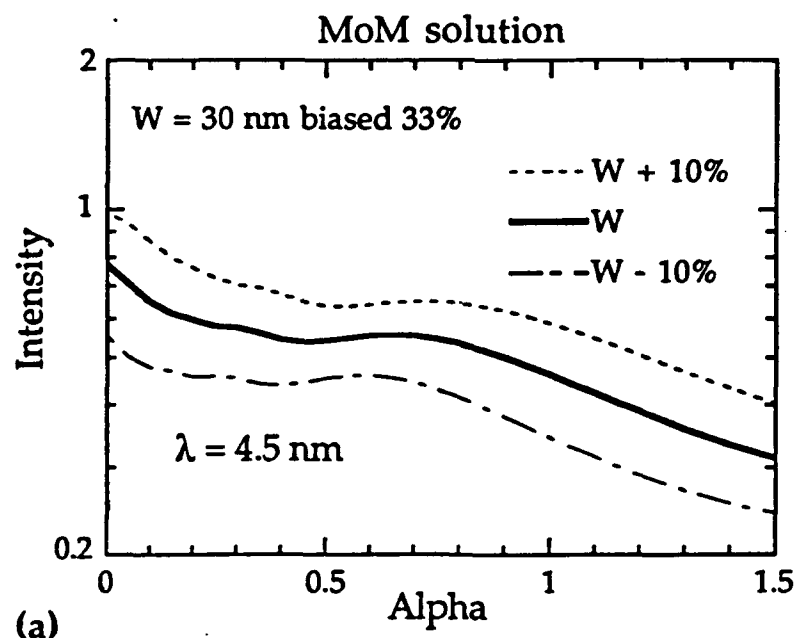


Fig. 2 (a), (b)

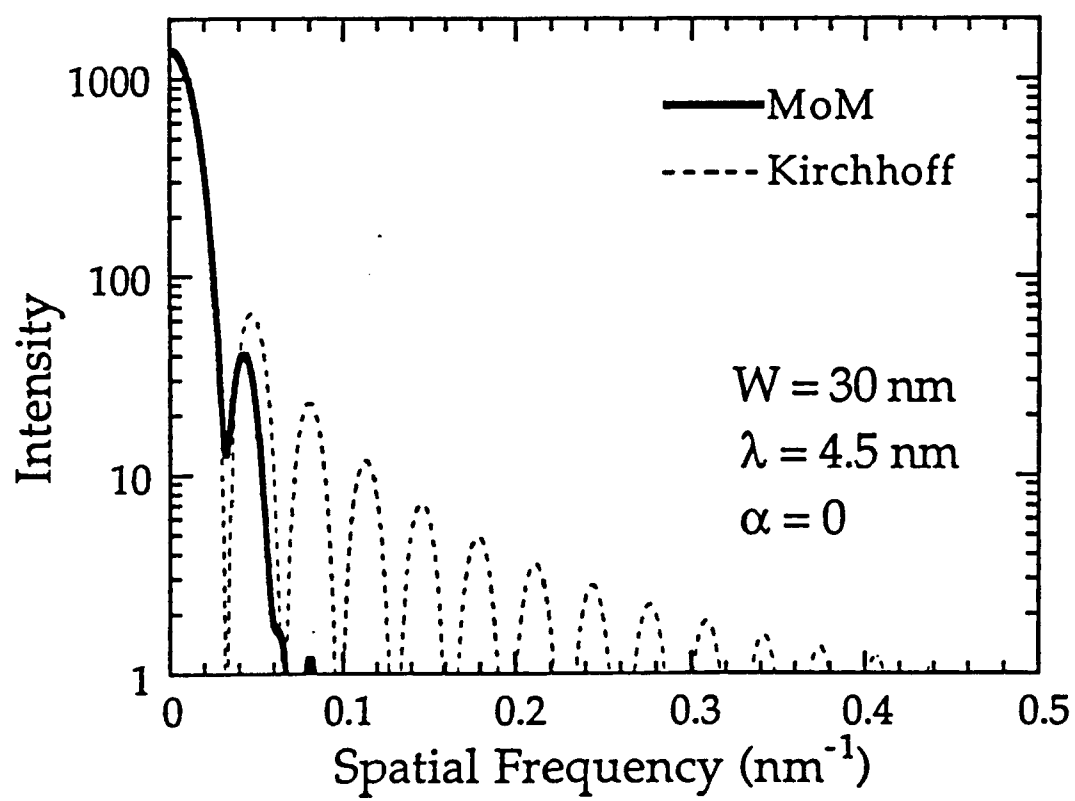


Fig. 3

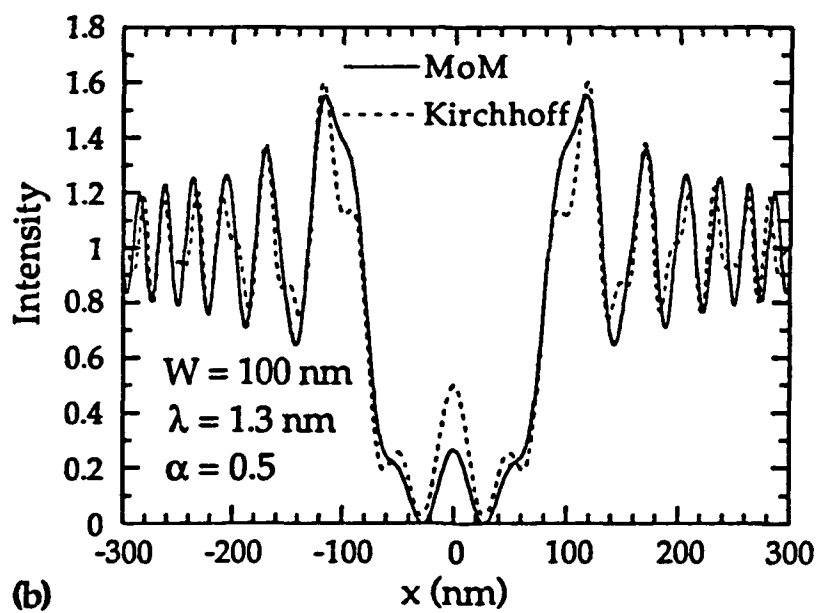
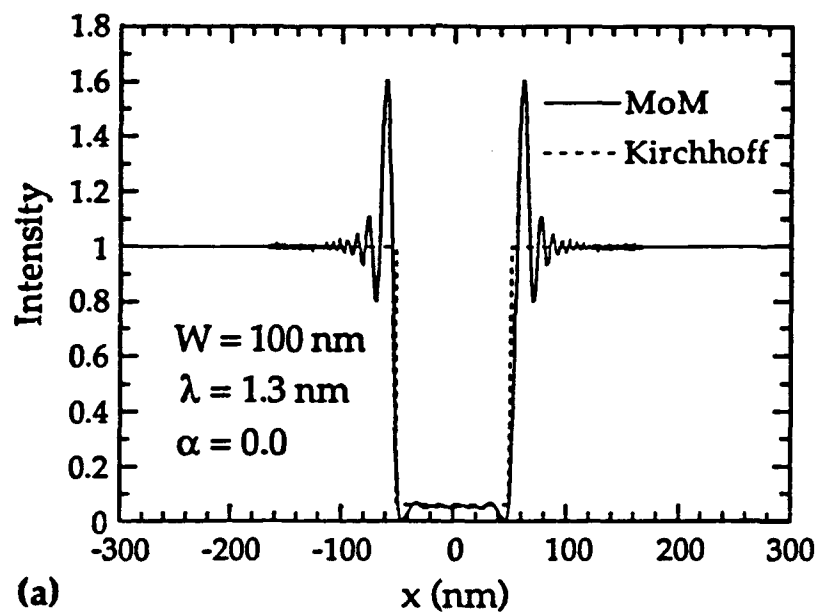


Fig. 4 (a), (b)

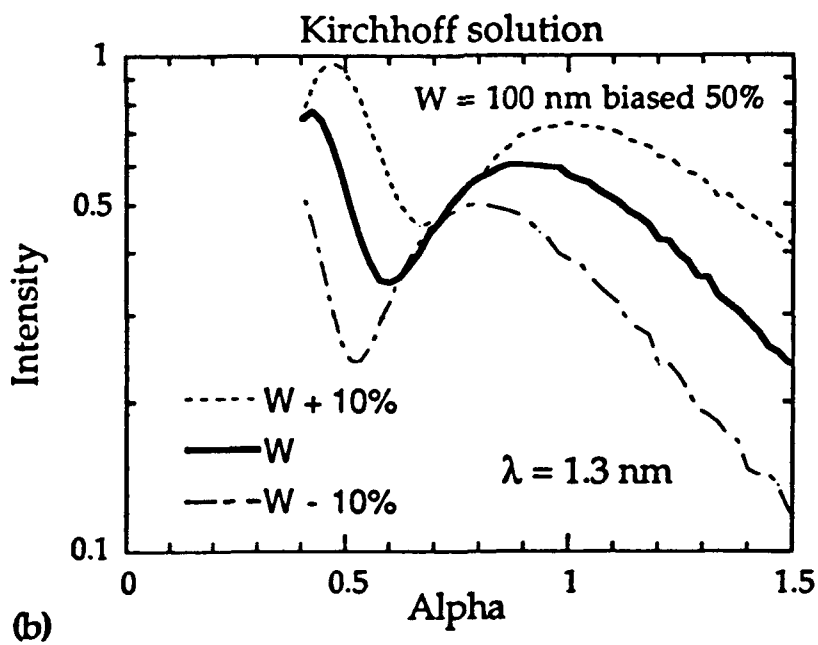
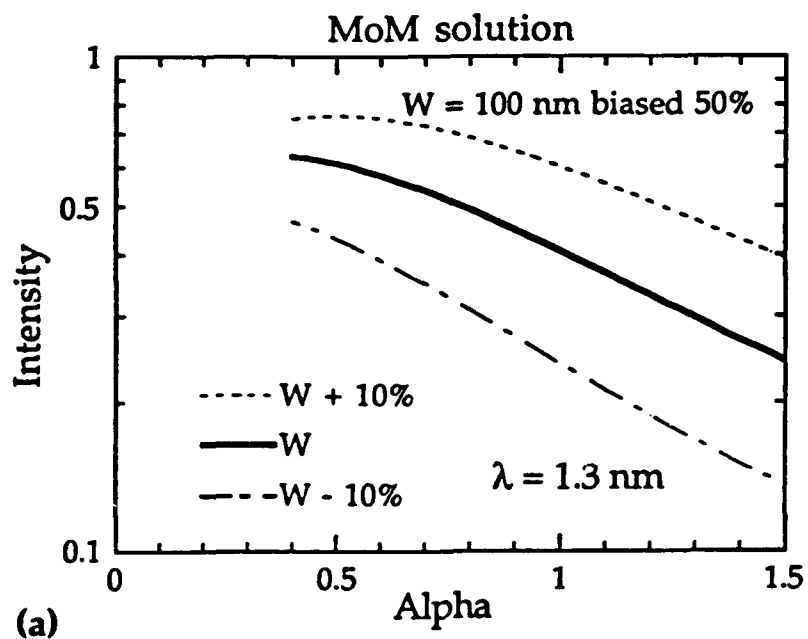


Fig. 5 (a), (b)

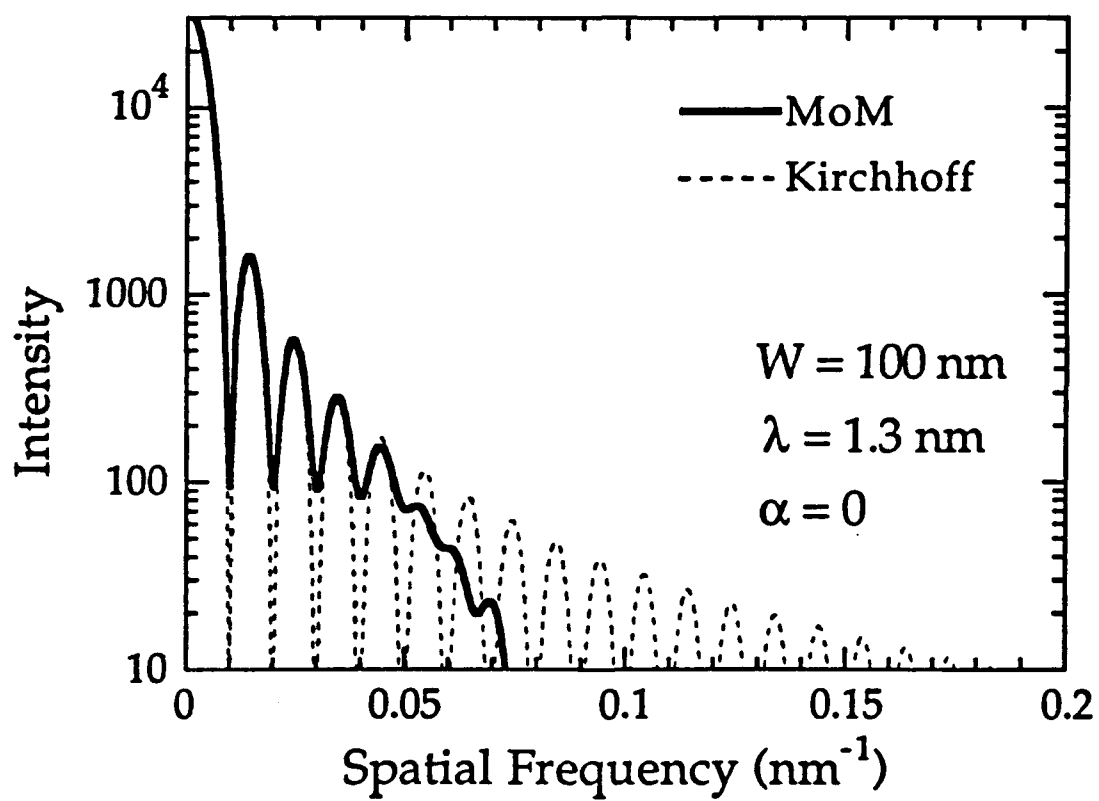


Fig. 6



# 3

## MODELLING OF LOSSY MICROSTRIP LINES WITH FINITE THICKNESS

*J. F. Kiang, S. M. Ali, and J. A. Kong*

- 3.1 Introduction
- 3.2 Integral Equation Formulation
- 3.3 Numerical Solution of Charge Distribution
- 3.4 Magnetostatic Dual Problem
- 3.5 Calculation of  $\bar{G}$  and  $\bar{R}$
- 3.6 Transmission Line Analysis
- 3.7 Results and Discussions
- Conclusions
- References

### 3.1 Introduction

For microwave integrated circuit applications, the characteristics of interconnects have been investigated for propagation modes [1,2], time response [3], crosstalk [4], coupling [5], delay [6], etc. In these analyses, it is assumed that quasi-TEM modes are guided along the multiconductor transmission line. In [1], the analysis was performed for two asymmetric transmission lines. In [2] and [3], an arbitrary number of transmission lines were analyzed. In [3], the load and the source conditions were presented in terms of the modal reflection and transmission coefficient matrices.

To perform the quasi-TEM analysis, the capacitance matrix for the multiconductor transmission line has to be obtained first. Both the spectral and the spatial domain methods have been proposed to

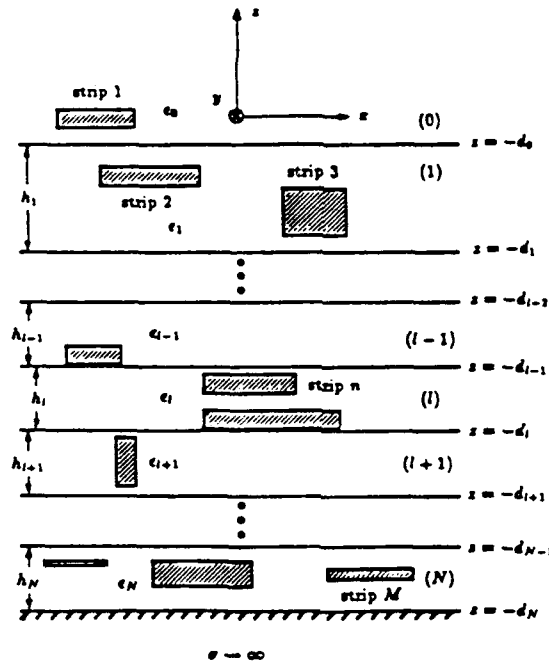


Figure 3.1 Geometrical configuration of  $M$  microstrip lines with finite thickness embedded in arbitrary layers of an isotropic stratified medium.

calculate the capacitance matrix. In the spectral domain methods, two side walls are used to enclose the whole transmission line structure, and the thickness of the strip lines has not been considered [7,8]. In using the spatial domain method [9], the structure has to be truncated to a finite extent to make the numerical implementation feasible. In [10], the infinite extent of the structure was incorporated, but only a two-layer medium was considered.

In practical microwave integrated circuits, the dielectric loss due to the substrate and the conductor loss due to the metallic strips have been studied in the analysis of circuit performances[11-13].

In this chapter, we present a quasi-TEM analysis of coupled lossy microstrip lines of finite strip thickness embedded in different layers of a lossy isotropic stratified medium as shown in Fig. 3.1. First, a spectral domain scalar Green's function in a lossy isotropic stratified medium is derived. In the formulation, no side walls are introduced, the transmission structure is not truncated, and the analysis is valid for arbitrary number of dielectric layers.

Based on the scalar Green's function, a set of coupled integral equations is obtained for the charge distribution on the strip surfaces. The method of moments is then applied where pulse basis functions and a point-matching scheme is used to solve numerically the set of integral equations for the charge distribution, and hence the capacitance matrix. The duality between the electrostatic formulation and the magnetostatic one is applied to calculate the inductance matrix. The conductance matrix is obtained by using the duality between the electrostatic problem and the current field problem. A perturbation method is used to calculate the resistance matrix.

Finally, a transmission line analysis is derived to obtain the transfer matrix for multiconductor line, which significantly reduces the effort in treating the load and the source conditions. Transient responses are obtained by using the Fourier transform. The results for two coupled lines are presented.

### 3.2 Integral Equation Formulation

We first formulate the scalar Green's function in the spectral domain in a homogeneous medium of permittivity  $\epsilon$  with a ground plane located at  $z = 0$ . Thus, we consider a uniform line charge of unit amplitude to be located at  $(x', z')$  along the  $y$  direction, and evaluate the electrostatic potential at  $(x, z)$ .

The scalar Green's function  $g(\bar{r}, \bar{r}')$  is the solution of the following Poisson equation :

$$\nabla_s^2 g(\bar{r}, \bar{r}') = -\frac{1}{\epsilon} \delta(\bar{r} - \bar{r}') \quad (1)$$

where  $\nabla_s^2 = \partial^2/\partial x^2 + \partial^2/\partial z^2$ ,  $\bar{r} = \hat{x}x + \hat{z}z$ , and  $\bar{r}' = \hat{x}x' + \hat{z}z'$ . The scalar Green's function can be expressed in the spectral domain as

$$g(\bar{r}, \bar{r}') = \iint_{-\infty}^{\infty} dk_x dk_z e^{ik_x x + ik_z z} \tilde{g}(\bar{k}_s) \quad (2)$$

where  $\bar{k}_s = \hat{x}k_x + \hat{z}k_z$ , and  $\tilde{g}(\bar{k}_s)$  is the Fourier transform of  $g(\bar{r}, \bar{r}')$  with respect to  $x$  and  $z$ . Substituting (2) into (1), and using the image theory, we get

$$\tilde{g}(\bar{k}_s) = \frac{1}{4\pi^2 \epsilon (k_x^2 + k_z^2)} \left[ e^{-ik_x x' - ik_z z'} - e^{-ik_x x' + ik_z z'} \right] \quad (3)$$

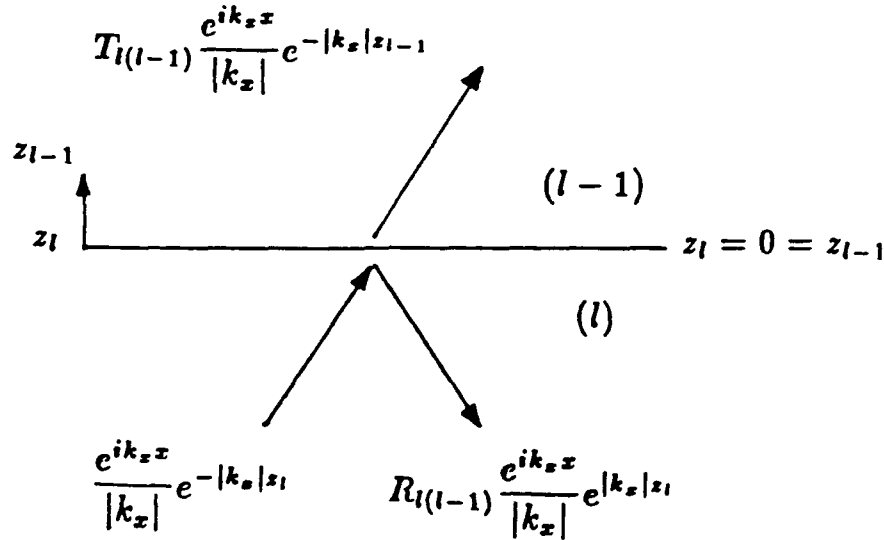


Figure 3.2 Definition of the local reflection and transmission coefficients at a dielectric interface between media (l) and (l-1).

The second term is the Fourier transform of the Green's function due to the image line charge at  $\bar{r}'_I = \hat{x}x' - \hat{z}z'$  which is the image of  $\bar{r}'$  with respect to the ground plane at  $z = 0$ . The scalar Green's function can then be written as

$$g(\bar{r}, \bar{r}') = \iint_{-\infty}^{\infty} dk_x dk_z e^{ik_x(x-x')} \frac{e^{ik_z(z-z')} - e^{ik_z(z+z')}}{4\pi^2 \epsilon (k_x^2 + k_z^2)} \quad (4)$$

By contour integration in the complex  $k_z$  plane, we have

$$g(\bar{r}, \bar{r}') = \int_{-\infty}^{\infty} dk_x \frac{e^{ik_x(x-x')}}{4\pi \epsilon |k_x|} \left[ e^{-|k_x||z-z'|} - e^{-|k_x|(z+z')} \right] \quad (5)$$

The integrand is regular at  $k_x = 0$ , and the integration is well defined as  $\bar{r}$  goes to infinity.

Next, we introduce local reflection and transmission coefficients at a boundary between two dielectrics. Consider a dielectric interface between media (l) and (l-1) as shown in Fig. 3.2. We assume that the spectral domain potential in each region can be expressed as

$$\phi_l(\bar{r}, k_x) = \frac{e^{ik_x x}}{|k_x|} \left[ e^{-|k_x| z_l} + R_{l(l-1)} e^{|k_x| z_l} \right] \quad (6a)$$

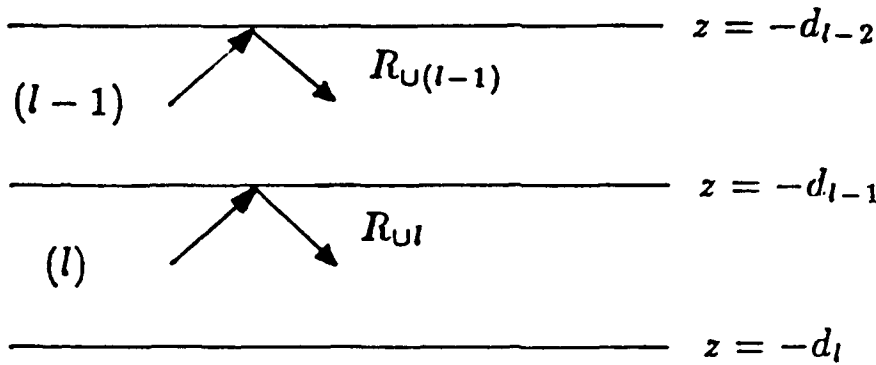


Figure 3.3 Definition of the global reflection coefficients at the upper boundaries of dielectric layers  $(l)$  and  $(l-1)$ .

$$\phi_{l-1}(\bar{r}, k_z) = \frac{e^{ik_z z}}{|k_z|} T_{l(l-1)} e^{-|k_z| z_{l-1}} \quad (6b)$$

where  $z_l = z_{l-1} = z + d_{l-1}$ ,  $R_{l(l-1)}$  and  $T_{l(l-1)}$  are constants to be determined. The  $z$  component of the electric field in each region can be obtained as

$$E_{lz}(\bar{r}, k_z) = e^{ik_z z} \left[ e^{-|k_z| z_l} - R_{l(l-1)} e^{|k_z| z_l} \right] \quad (7a)$$

$$E_{(l-1)z}(\bar{r}, k_z) = T_{l(l-1)} e^{ik_z z} e^{-|k_z| z_{l-1}} \quad (7b)$$

By imposing the boundary conditions that the potential and the normal component of the electric flux density are continuous at  $z = -d_{l-1}$ , we obtain

$$R_{l(l-1)} = \frac{\epsilon_l - \epsilon_{l-1}}{\epsilon_l + \epsilon_{l-1}} \quad (8a)$$

$$T_{l(l-1)} = \frac{2\epsilon_l}{\epsilon_l + \epsilon_{l-1}} \quad (8b)$$

where  $R_{l(l-1)}$  and  $T_{l(l-1)}$  can be interpreted as local reflection and transmission coefficients, respectively.

Next, consider the two source-free layers  $(l)$  and  $(l-1)$  of the stratified medium as shown in Fig. 3.3, where the potential and the  $z$

component of the electric field in each layer can be expressed as

$$\phi_j(\bar{r}, k_z) = \frac{e^{ik_z z}}{|k_z|} \left[ A_j e^{-|k_z| z_j} + B_j e^{|k_z| z_j} \right] \quad (9a)$$

$$E_{jz}(\bar{r}, k_z) = e^{ik_z z} \left[ A_j e^{-|k_z| z_j} - B_j e^{|k_z| z_j} \right] \quad (9b)$$

where  $z_j = z + d_j$  and  $j = l, l-1$ . We introduce the global reflection coefficient  $R_{Uj}$  defined at the upper boundary of layer ( $j$ ),  $z = -d_{j-1}$ , as

$$R_{Uj} = \frac{B_j e^{|k_z| h_j}}{A_j e^{-|k_z| h_j}} \quad (10)$$

where  $h_j$  is the thickness of layer ( $j$ ). By imposing the boundary conditions at  $z = -d_{l-1}$ , we obtain the following recursive relation

$$R_{Ul} = \frac{R_{l(l-1)} + R_{U(l-1)} e^{-2|k_z| h_{l-1}}}{1 + R_{l(l-1)} R_{U(l-1)} e^{-2|k_z| h_{l-1}}}, \quad l = 2, \dots, N \quad (11)$$

and  $R_{U1} = R_{10}$ . Similarly, the global reflection coefficient  $R_{\cap j}$  is defined at the lower boundary of layer ( $j$ ),  $z = -d_j$ , as

$$R_{\cap j} = \frac{A_j}{B_j}. \quad (12)$$

By imposing the boundary condition at  $z = -d_l$ , we obtain

$$R_{\cap l} = \frac{R_{l(l+1)} + R_{\cap(l+1)} e^{-2|k_z| h_{l+1}}}{1 + R_{l(l+1)} R_{\cap(l+1)} e^{-2|k_z| h_{l+1}}}, \quad l = N-1, \dots, 0 \quad (13)$$

and  $R_{\cap N} = -1$ .

With the use of the above reflection coefficients, the expression of the scalar Green's function in a layered medium can be obtained in a simple way. For the case where both the line charge and the observation point are located in the upper half-space, that is layer (0), we have

$$g_{00}(\bar{r}, \bar{r}') = \frac{1}{4\pi\epsilon_0} \int_{-\infty}^{\infty} dk_z \frac{e^{ik_z(z-z')}}{|k_z|} \left[ e^{-|k_z||z_0-z'_0|} + R_{\cap 0} e^{-|k_z|(z_0+z'_0)} \right] \quad (14)$$

where  $z_0 = z + d_0$ ,  $z'_0 = z' + d_0$ , the uniform line charge of unit amplitude is located at  $\bar{r}' = (x', z'_0)$ , and the observation point is located at  $\bar{r} = (x, z_0)$ . The first term inside the brackets is the direct term, and the second term can be interpreted as due to the reflection from the lower boundary at  $z = -d_0$ .

For the case when both the line charge and the observation point are both located in an arbitrary layer ( $l$ ) with  $l \neq 0$ , the Green's function can be expressed as

$$g_{ll}(\bar{r}, \bar{r}') = \frac{1}{4\pi\epsilon_l} \int_{-\infty}^{\infty} dk_x \frac{e^{ik_x(z-z')}}{|k_x|} \left[ e^{-|k_x||z_l-z'_l|} + A(k_x)e^{-|k_x|z_l} + B(k_x)e^{|k_x|z_l} \right] \quad (15)$$

where  $z_l = z + d_l$ ,  $z'_l = z' + d_l$ ,  $A(k_x)$  and  $B(k_x)$  are the unknowns to be determined. From the definition of  $R_{ul}$  and  $R_{\cap l}$ , we have

$$R_{ul} \left[ e^{-|k_x|(z_l-z'_l)} + A(k_x)e^{-|k_x|z_l} \right] = B(k_x)e^{|k_x|z_l}, \quad z_l = h_l \quad (16a)$$

$$R_{\cap l} \left[ e^{-|k_x|(z'_l-z_l)} + B(k_x)e^{|k_x|z_l} \right] = A(k_x)e^{-|k_x|z_l}, \quad z_l = 0 \quad (16b)$$

By solving (16), we get

$$A(k_x) = \frac{R_{\cap l}e^{-|k_x|z'_l} + R_{ul}R_{\cap l}e^{-|k_x|(2h_l-z'_l)}}{1 - R_{ul}R_{\cap l}e^{-2|k_x|h_l}} \quad (17a)$$

$$B(k_x) = \frac{R_{ul}e^{-|k_x|(2h_l-z'_l)} + R_{ul}R_{\cap l}e^{-|k_x|(2h_l+z'_l)}}{1 - R_{ul}R_{\cap l}e^{-2|k_x|h_l}} \quad (17b)$$

Substituting (17) into (15), we obtain the explicit form of the Green's function  $g_{ll}(\bar{r}, \bar{r}')$  in the layer ( $l$ ) as

$$g_{ll}(\bar{r}, \bar{r}') = \frac{1}{4\pi\epsilon_l} \int_{-\infty}^{\infty} dk_x \frac{e^{ik_x(z-z')}}{|k_x|} \left\{ e^{-|k_x||z_l-z'_l|} + \frac{1}{1 - R_{ul}R_{\cap l}e^{-2|k_x|h_l}} \right. \\ \left. \left[ R_{ul}e^{-|k_x|(2h_l-z_l-z'_l)} + R_{\cap l}e^{-|k_x|(z_l+z'_l)} \right. \right. \\ \left. \left. + R_{ul}R_{\cap l}e^{-|k_x|(z_l-z'_l+2h_l)} + R_{ul}R_{\cap l}e^{-|k_x|(-z_l+z'_l+2h_l)} \right] \right\} \quad (18)$$

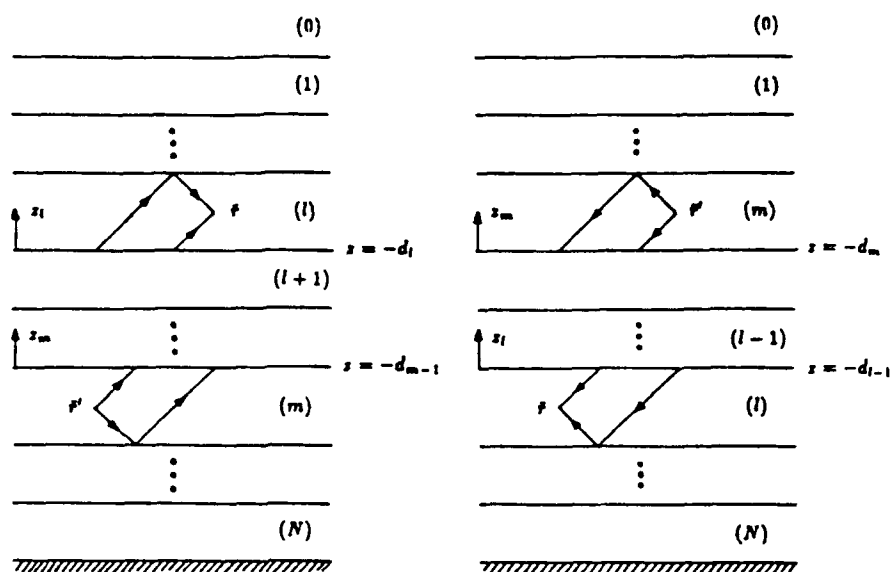


Figure 3.4 Determination of the scalar Green's function where the source is in a layer (m) and the observation point is in the layer (l). (a) Layer (l) is above layer (m). (b) Layer (l) is below layer (m).

The first term inside the brace is the direct term, the other terms are the summation of the multiple reflections between the two boundaries at  $z = -d_{l-1}$  and  $z = -d_l$ . It is observed that (14) is a special case of (18) with  $l = 0$  and  $R_{ul} = 0$ .

Next, we consider the case when the source and the observation points are in different layers. As shown in Fig. 3.4(a), the source is in a layer (m) and the observation point is in a layer (l) which is above layer (m). We assume that each spectral field component is transmitted upward from the source layer (m) to the layer (l) with the upward transmission coefficient  $X_{ul,m}$ . The Green's function can thus be expressed as

$$g_{lm}(\bar{r}', \bar{r}'') = \frac{1}{4\pi\epsilon_m} \int_{-\infty}^{\infty} dk_x \frac{e^{ik_x(z-z')}}{|k_x|} X_{ul,m} \left[ e^{-|k_x|z_l} + R_{ul} e^{-|k_x|(2h_l-z_l)} \right] \frac{e^{|k_x|z'_m} + R_{um} e^{-|k_x|(2h_m+z'_m)}}{1 - R_{um}R_{um} e^{-2|k_x|h_m}} \quad (19)$$



where  $z_l$  and  $z'_m$  are the local coordinates defined as  $z_l = z + d_l$  and  $z'_m = z' + d_{m-1}$ , respectively. Similarly, when the observation point is located in the layer  $(l+1)$ , we have

$$g_{(l+1)m}(\bar{r}_>, \bar{r}'_<) = \frac{1}{4\pi\epsilon_m} \int_{-\infty}^{\infty} dk_z \frac{e^{ik_z(z-z')}}{|k_z|} X_{U(l+1),m} \left[ e^{-|k_z|z_{l+1}} + R_{U(l+1)} e^{-|k_z|(2h_{l+1}-z_{l+1})} \right] \frac{e^{|k_z|z'_m} + R_{Um} e^{-|k_z|(2h_m+z'_m)}}{1 - R_{Um}R_{Um} e^{-2|k_z|h_m}} \quad (20)$$

where  $z_{l+1} = z + d_{l+1}$ . Imposing the boundary conditions at the interface  $z = -d_l$ , we get

$$X_{U,l,m} = X_{U(l+1),m} e^{-|k_z|h_{l+1}} \frac{1 + R_{U(l+1)}}{1 + R_{Ul} e^{-2|k_z|h_l}}, \quad l = m-2, \dots, 0 \quad (21)$$

and for  $l = m-1$ , we have

$$X_{U(m-1),m} = \frac{1 + R_{Um}}{1 + R_{U(m-1)} e^{-2|k_z|h_{m-1}}} \quad (22)$$

For the case when the layer  $(m)$  is above layer  $(l)$  as shown in Fig. 3.4(b), the Green's function may be expressed as

$$g_{lm}(\bar{r}_<, \bar{r}'_>) = \frac{1}{4\pi\epsilon_m} \int_{-\infty}^{\infty} dk_z \frac{e^{ik_z(z-z')}}{|k_z|} X_{Ul,m} \left[ e^{|k_z|z_l} + R_{Ul} e^{-|k_z|(2h_l+z_l)} \right] \frac{e^{-|k_z|z'_m} + R_{Um} e^{-|k_z|(2h_m-z'_m)}}{1 - R_{Um}R_{Um} e^{-2|k_z|h_m}} \quad (23)$$

where  $X_{Ul,m}$  is the downward transmission coefficient,  $z_l$  and  $z'_m$  are the local coordinates defined as  $z_l = z + d_{l-1}$  and  $z'_m = z' + d_m$ , respectively. Similarly, when the observation point is located in the layer  $(l-1)$ , we have

$$g_{(l-1)m}(\bar{r}_<, \bar{r}'_>) = \frac{1}{4\pi\epsilon_m} \int_{-\infty}^{\infty} dk_z \frac{e^{ik_z(z-z')}}{|k_z|} X_{U(l-1),m} \left[ e^{|k_z|z_{l-1}} + R_{U(l-1)} e^{-|k_z|(2h_{l-1}+z_{l-1})} \right] \frac{e^{-|k_z|z'_m} + R_{Um} e^{-|k_z|(2h_m-z'_m)}}{1 - R_{Um}R_{Um} e^{-2|k_z|h_m}} \quad (24)$$

where  $z_{l-1} = z + d_{l-2}$ . Imposing the boundary conditions at the interface  $z = -d_{l-1}$ , we have

$$X_{\cap l, m} = X_{\cap(l-1), m} e^{-|k_z| h_{l-1}} \frac{1 + R_{\cap(l-1)}}{1 + R_{\cap l} e^{-2|k_z| h_l}}, \quad l = m + 2, \dots, N \quad (25)$$

and for  $l = m + 1$ , we have

$$X_{\cap(m+1), m} = \frac{1 + R_{\cap m}}{1 + R_{\cap(m+1)} e^{-2|k_z| h_{m+1}}} \quad (26)$$

Next, consider  $M$  microstrip lines embedded in arbitrary layers of an isotropic stratified medium as shown in Fig. 3.1. All the conductor strips are of finite thickness, the permittivity of layer  $(j)$  is  $\epsilon_j$ , and a ground plane is put at  $z = -d_N$  as the potential reference.

Using the scalar Green's function, the potential in layer  $(l)$  can be represented as

$$V_l(\bar{r}) = \sum_{p=1}^M \int_{\Gamma_p} d\bar{r}' g_{lL(p)}(\bar{r}, \bar{r}') \rho_p(\bar{r}') \quad (27)$$

where  $\Gamma_p$  is the cross section contour of the  $p$ th microstrip line,  $\rho_p(\bar{r}')$  is the charge density on the  $p$ th microstrip surface,  $L(p)$  is the layer where the  $p$ th microstrip line is embedded. The cross section of the microstrip lines can be arbitrary in general. For practical applications, only the rectangular cross sections are considered.

The potential distribution in (27) satisfies all the boundary conditions that the potential and the normal electric flux density are continuous across the interfaces between adjacent dielectric layers. To obtain the charge distribution on each microstrip surface, we impose the boundary condition that the potential on each microstrip is equal to the impressed voltage. Thus we have

$$\sum_{p=1}^M \int_{\Gamma_p} d\bar{r}' g_{L(q)L(p)}(\bar{r}, \bar{r}') \rho_p(\bar{r}') = V_q, \quad \bar{r} \text{ on } \Gamma_q \quad (28)$$

where  $q = 1, \dots, M$ .

In the next section, the method of moments is applied to solve (28) for the charge distributions.

### 3.3 Numerical Solution of Charge Distribution

By applying the method of moments to solve (28), we first choose a set of pulse basis functions for the surface charge density, hence

$$\rho_p(\bar{r}') = \sum_{i=1}^{N_p} a_{pi} P_{pi}(\bar{r}'), \quad p = 1, \dots, M \quad (29)$$

where  $a_{pi}$  and  $P_{pi}(\bar{r}')$  are, respectively, the expansion coefficients and the basis functions on the  $i$ th section of the  $p$ th microstrip surface; and  $N_p$  is the total number of basis functions on the  $p$ th microstrip surface. The pulse function is defined as

$$P_{pi}(\bar{r}) = \begin{cases} 1, & \bar{r} \text{ on } \Gamma_{pi} \\ 0, & \text{elsewhere} \end{cases} \quad (30)$$

where  $\Gamma_{pi}$  is the  $i$ th section on the  $p$ th microstrip surface.

Substituting (29) into (28), we have

$$\sum_{p=1}^M \sum_{i=1}^{N_p} a_{pi} \int_{\Gamma_{pi}} d\bar{r}' g_{L(q)L(p)}(\bar{r}, \bar{r}') P_{pi}(\bar{r}') = V_q, \quad \bar{r} \text{ on } \Gamma_q \quad (31)$$

where  $q = 1, \dots, M$ .

Next, we choose the center point at each pulse basis as the testing point to test (31), thus we have

$$\sum_{p=1}^M \sum_{i=1}^{N_p} Z_{qj,pi} a_{pi} = \beta_{qj}, \quad 1 \leq q \leq M, 1 \leq j \leq N_q \quad (32)$$

where

$$Z_{qj,pi} = \int_{\Gamma_{pi}} d\bar{r}' g_{L(q)L(p)}(\bar{r}_{qj}, \bar{r}') P_{pi}(\bar{r}') \quad (33)$$

$$\beta_{qj} = V_q \quad (34)$$

and  $\bar{r}_{qj} = (x_{qj}, z_{qj})$  is the center coordinate of  $\Gamma_{qj}$ . By solving (32) for  $a_{pi}$ 's, the charge density can be obtained.

The capacitance matrix  $\bar{\bar{C}}$  of  $M$  microstrip lines can be obtained by solving (28)  $M$  times. For the  $n$ th time, all the microstrip lines are

grounded except that one volt is imposed on the  $n$ th line. By solving (32), the charge distribution is obtained. The total surface charge per unit length on the  $m$ th microstrip line is equal to the  $mn$ th element of the capacitance matrix,  $C_{mn}$ . This can be observed from the definition of the capacitance matrix

$$\sum_{p=1}^M C_{qp} V_p = Q_q, \quad 1 \leq q \leq M \quad (35)$$

By setting  $V_p = \delta_{p,n}$ , we have  $Q_q^{(n)} = C_{qn}$  with  $1 \leq q \leq M$ . Here,  $\delta_{p,n}$  is the Kronecker's delta function and the superscript  $(n)$  in  $Q_q^{(n)}$  is the index of the microstrip where one volt is imposed.

### 3.4 Magnetostatic Dual Problem

In this section, we briefly review the magnetostatic dual problem. For nonmagnetic materials, the magnetostatic problem for the geometrical configuration shown in Fig. 3.1 is equivalent to the one where all the dielectric media are replaced by the free space. The magnetostatic potential  $\psi(\bar{r})$  due to a uniform line current at  $\bar{r}'$  can be derived in a way similar to that in Section 2 as

$$\sum_{p=1}^M \int_{\Gamma_p} ds' g_{L(q)L(p)}^M(\bar{r}, \bar{r}') J_p(\bar{r}') = \psi_q, \quad \bar{r} \text{ on } \Gamma_q \quad (36)$$

where  $q = 1, \dots, M$ ;  $g_{L(q)L(p)}^M(\bar{r}, \bar{r}')$  is the scalar Green's function;  $J_p(\bar{r}')$  is the surface current on the  $p$ th microstrip surface; and  $\psi_q$  is the magnetostatic potential measured on the  $q$ th microstrip surface with respect to the ground plane, which is equal to the magnetic flux linkage between the  $q$ th microstrip line and the ground plane per unit length.

Instead of solving (36) directly, a dual electrostatic problem for the same geometrical configuration in free space is solved. It can be shown that

$$g^M(\bar{r}, \bar{r}') = \mu_0 \epsilon_0 g^E(\bar{r}, \bar{r}') \quad (37)$$

where  $g^E(\bar{r}, \bar{r}')$  is the scalar Green's function derived in Section 2 with all  $\epsilon_l$ 's replaced by the dielectric constant in the free space.

Imposing the same boundary conditions that  $V_q = \psi_q$  for  $1 \leq q \leq M$ , we have

$$J_p^{(k)}(\bar{r}) = \frac{\rho_p^{(k)}(\bar{r})}{\mu_0 \epsilon_0}, \quad 1 \leq p, k \leq M \quad (38)$$

where  $\rho_p^{(k)}(\bar{r})$  is the surface charge distribution on the  $p$ th microstrip surface when we impose one volt on the  $k$ th strip, and zero volt on the other strips;  $J_p^{(k)}(\bar{r})$  is the surface current distribution on the  $p$ th microstrip surface when we impose one tesla-m on the  $k$ th strip, and zero tesla-m on the other strips.

In general, the surface current on the  $p$ th microstrip surface can be expressed as

$$J_p(\bar{r}) = \sum_{k=1}^M \psi_k J_p^{(k)}(\bar{r}) = \frac{1}{\mu_0 \epsilon_0} \sum_{k=1}^M \psi_k \rho_p^{(k)}(\bar{r}) \quad (39)$$

Integrating (39) over one unit length on the  $p$ th microstrip surface, we have

$$I_p = \frac{1}{\mu_0 \epsilon_0} \sum_{k=1}^M C_{0,pk} \psi_k \quad (40)$$

where  $I_p$  is the surface current on the  $p$ th microstrip line, and  $C_{0,pk}$  is the  $pk$ th element of the capacitance matrix  $\overline{\overline{C}}_0$  with all the dielectrics replaced by free space. Hence, we obtain the conventional result that the inductance matrix  $\overline{\overline{L}}$  is proportional to the inverse of the capacitance matrix in free space as

$$\overline{\overline{L}} = \mu_0 \epsilon_0 \overline{\overline{C}}_0^{-1} \quad (41)$$

### 3.5 Calculation of $\overline{\overline{G}}$ and $\overline{\overline{R}}$

In this section, the dielectric loss and conductor loss are considered. The transmission line equations for  $M$  coupled microstrip lines are

$$-\frac{\partial \bar{I}}{\partial y} = [\overline{\overline{G}} - i\omega \overline{\overline{C}}] \cdot \bar{V} \quad (42a)$$

$$-\frac{\partial \bar{V}}{\partial y} = [\overline{\overline{R}} - i\omega \overline{\overline{L}}] \cdot \bar{I} \quad (42b)$$

where the conductance matrix  $\overline{\overline{G}}$  accounts for the dielectric loss, and the resistance matrix  $\overline{\overline{R}}$  accounts for the conductor loss.

The  $n$ th eigen solution to (42) can be represented as

$$\overline{I} = \overline{I}_n e^{-\gamma_n y} \quad (43a)$$

$$\overline{V} = \overline{V}_n e^{-\gamma_n y} \quad (43b)$$

where  $\gamma_n$  is the eigenvalue of the  $n$ th mode; and  $\overline{I}_n$  and  $\overline{V}_n$  are the corresponding eigenvectors. Substituting (43) into (42), we have

$$\gamma_n \overline{I}_n = [\overline{\overline{G}} - i\omega \overline{\overline{C}}] \cdot \overline{V}_n \quad (44a)$$

$$\gamma_n \overline{V}_n = [\overline{\overline{R}} - i\omega \overline{\overline{L}}] \cdot \overline{I}_n \quad (44b)$$

and hence

$$\gamma_n^2 \overline{I}_n = [\overline{\overline{G}} - i\omega \overline{\overline{C}}] \cdot [\overline{\overline{R}} - i\omega \overline{\overline{L}}] \cdot \overline{I}_n \quad (45a)$$

$$\gamma_n^2 \overline{V}_n = [\overline{\overline{R}} - i\omega \overline{\overline{L}}] \cdot [\overline{\overline{G}} - i\omega \overline{\overline{C}}] \cdot \overline{V}_n \quad (45b)$$

There are in general  $M$  eigen solutions to the above equations. The eigenvalues solved from (45a) and (45b) are the same; and the eigenvectors  $\overline{I}_n$ 's and  $\overline{V}_n$ 's are related by (44).

For the  $n$ th eigenmode, the time-average Poynting's power  $P_{nT}$  can be represented as

$$P_{nT} = \frac{1}{2} \text{Re} [\overline{I}_n^\dagger \cdot \overline{V}_n] \quad (46)$$

where  $\overline{I}_n^\dagger$  is the transposed, complex conjugate of  $\overline{I}_n$ . The time-average power loss per unit length  $P_{nL}$  along the transmission lines can be calculated as

$$P_{nL} = P_{nC} + P_{nD} = 2\alpha_{nT} P_{nT} \quad (47)$$

where

$$P_{nC} = (1/2) \overline{I}_n^\dagger \cdot \overline{\overline{R}} \cdot \overline{I}_n = 2\alpha_{nC} P_{nT} \quad (48a)$$

$$P_{nD} = (1/2) \overline{V}_n^\dagger \cdot \overline{\overline{G}} \cdot \overline{V}_n = 2\alpha_{nD} P_{nT} \quad (48b)$$

where  $P_{nC}$  and  $P_{nD}$  are the time-average conductor loss and dielectric loss per unit length, respectively;  $\alpha_{nT}$ ,  $\alpha_{nC}$ , and  $\alpha_{nD}$  are the corresponding attenuation constants for the  $n$ th mode.

To calculate the conductance matrix which accounts for the dielectric loss, we make use of the duality between the electrostatic problem and the current field problem. Assume that the geometrical configuration of the current field problem is the same as in Fig. 3.1, and the conductivity in layer ( $l$ ) is designated by  $\sigma_l$  with  $0 \leq l \leq N$ . If the conductivities in the current field problem and the dielectric constants in the electrostatic problem satisfy the following relation

$$\frac{\sigma_0}{\epsilon_0} = \frac{\sigma_1}{\epsilon_1} = \dots = \frac{\sigma_N}{\epsilon_N} = \alpha \quad (49)$$

then, we have

$$\bar{\bar{G}} = \alpha \bar{\bar{C}} \quad (50)$$

The perturbation method is used to solve for the attenuation constants  $\alpha_{nC}$  and the resistance matrix  $\bar{\bar{R}}$ . We start from the lossless eigenvalue equations :

$$\begin{aligned} \bar{\bar{C}} \cdot \bar{\bar{L}} \cdot \bar{I}_{0n} &= \frac{1}{v_n^2} \bar{I}_{0n} \\ \bar{\bar{L}} \cdot \bar{\bar{C}} \cdot \bar{V}_{0n} &= \frac{1}{v_n^2} \bar{V}_{0n} \end{aligned} \quad (51)$$

where  $\gamma_n = -i\beta_n$ ;  $v_n = \omega/\beta_n$  is the phase velocity for the  $n$ th mode; and  $\bar{\bar{C}}$  is the capacitance matrix with all materials lossfree. The time-average guided power can be approximated by the power guided along lossless lines as

$$P_{nT} \approx \frac{1}{2} \text{Re} [\bar{I}_{0n}^\dagger \cdot \bar{V}_{0n}] \quad (52)$$

The power loss per unit length of the  $n$ th mode due to imperfect conductor can be calculated by using the surface current obtained for the perfect conductor lines. Thus, we have

$$P_{nC} = \frac{1}{2} \sum_{k=1}^{M'} R_{kS} \int_{\Gamma_k} |J_{nk}(\bar{r})|^2 d\bar{r} \quad (53)$$

where  $R_{kS}$  is the surface resistance per unit area on the  $k$ th microstrip surface,  $J_{nk}(\bar{r})$  is the surface current distribution of the  $n$ th

mode on the  $k$ th microstrip surface. Here  $M'$  is the total number of conductors including the ground planes. As defined in (29),  $\rho_k^{(i)}(\bar{r})$  can be expanded in terms of the pulse basis functions as

$$\rho_k^{(i)}(\bar{r}) = \sum_{m=1}^{N_k} a_{km}^{(i)} P_{km}(\bar{r}) \quad (54)$$

where  $P_{km}(\bar{r})$  is the basis function defined in (30). By using (39), the surface current on the  $k$ th microstrip surface can be represented as

$$J_k(\bar{r}) = \frac{1}{\mu_0 \epsilon_0} \sum_{i=1}^M \psi_i \sum_{m=1}^{N_k} a_{km}^{(i)} P_{km}(\bar{r}) \quad (55)$$

where  $\psi_i$  is obtained by solving

$$\psi_i = \sum_{j=1}^M L_{ij} I_{0n,j} \quad (56)$$

where  $L_{ij}$  is the  $ij$ th element of the inductance matrix  $\bar{\bar{L}}$ ,  $I_{0n,j}$  is the  $j$ th element of the eigenvector  $\bar{I}_{0n}$ . The conductor loss can then be calculated as

$$P_{nC} = \frac{1}{2} \sum_{k=1}^M R_{kS} (\mu_0 \epsilon_0)^{-2} \sum_{m=1}^{N_k} \left| \sum_{i=1}^M \psi_i a_{km}^{(i)} \right|^2 \int_{\Gamma_{km}} |P_{km}(\bar{r})|^2 d\bar{r} + P_G \quad (57)$$

where  $P_G$  is the conductor loss due to the ground planes. To calculate  $P_G$ , we first solve for the magnetic field  $H_z$  as

$$H_z(\bar{r}) = \sum_{k=1}^M \sum_{m=1}^{N_k} \left[ \sum_{i=1}^M \psi_i a_{km}^{(i)} \right] \int_{\Gamma_{km}} P_{km}(\bar{r}') d\bar{r}' \int_{-\infty}^{\infty} dk_x e^{ik_x(z-z')} \left[ -\frac{1}{\mu_0} \frac{\partial \bar{g}^E(k_x, z, z')}{\partial z} \right] \quad (58)$$

where  $\bar{g}^E(k_x, z, z')$  is the Fourier transform with respect to  $z$  of  $g^E(\bar{r}, \bar{r}')$  as defined in (37). Thus, we have

$$P_G = 2\pi R_S \sum_{k=1}^M \sum_{m=1}^{N_k} \sum_{k'=1}^M \sum_{m'=1}^{N_{k'}} \left[ \sum_{i=1}^M \psi_i a_{km}^{(i)} \right]^* \left[ \sum_{i'=1}^M \psi_{i'} a_{k'm'}^{(i')} \right]$$



$$\int_{\Gamma_{k,m}} d\vec{r}' P_{km}(\vec{r}') \int_{\Gamma_{k',m'}} d\vec{r}'' P_{k'm'}(\vec{r}'') \int_0^\infty dk_z \cos[k_z(x' - x'')] \left[ -\frac{1}{\mu_0} \frac{\partial \bar{g}^E(k_z, z_G, z')}{\partial z} \right]^* \left[ -\frac{1}{\mu_0} \frac{\partial \bar{g}^E(k_z, z_G, z'')}{\partial z} \right] \quad (59)$$

where  $R_S$  is the surface resistance per unit area of the ground planes,  $z_G$  is the  $z$  coordinate of the ground planes.

Now, set  $\bar{G} = 0$  in (45b), we have

$$(\alpha_{nC} - i\beta_n)^2 \bar{V}_n = [\bar{R} - i\omega \bar{L}] \cdot [-i\omega \bar{C}] \cdot \bar{V}_n \quad (60)$$

Making the approximation that  $\beta_n \approx \beta_{0n}$ ,  $\bar{V}_n \approx \bar{V}_{0n}$ , and utilizing the relation (44) with  $\bar{G} = 0$ , the imaginary part of (60) becomes

$$2\alpha_{nC} V_{0n,m} = \sum_{k=1}^M R_{mk} I_{0n,k}, \quad 1 \leq n, m \leq M \quad (61)$$

where  $I_{0n,k}$  is the  $k$ th element of  $\bar{I}_{0n}$ ; and  $V_{0n,m}$  is the  $m$ th element of  $\bar{V}_{0n}$ . The elements of  $\bar{R}$  can be obtained by solving (61).

After obtaining the matrices  $\bar{C}$ ,  $\bar{L}$ ,  $\bar{G}$ , and  $\bar{R}$ ; the matrix equations (44) and (45) can be solved for the eigenvalues and eigenvectors.

### 3.6 Transmission Line Analysis

The voltage and current along the transmission lines can be represented in terms of the eigenvectors obtained in the last section as

$$\begin{aligned} \bar{V}(y) &= \sum_{n=1}^M a_n \bar{V}_n e^{-\gamma_n y} + \sum_{n=1}^M b_n \bar{V}_n e^{\gamma_n y} \\ &= \bar{S}_V \cdot \bar{\Lambda}(y) \cdot \bar{A} + \bar{S}_V \cdot \bar{\Lambda}(-y) \cdot \bar{B} \end{aligned} \quad (62a)$$

$$\begin{aligned} \bar{I}(y) &= \sum_{n=1}^M a_n \bar{I}_n e^{-\gamma_n y} - \sum_{n=1}^M b_n \bar{I}_n e^{\gamma_n y} \\ &= \bar{S}_I \cdot \bar{\Lambda}(y) \cdot \bar{A} - \bar{S}_I \cdot \bar{\Lambda}(-y) \cdot \bar{B} \end{aligned} \quad (62b)$$

where  $\bar{S}_V$  is the matrix with the eigenvector  $\bar{V}_n$  as its  $n$ th column;  $\bar{S}_I$  is the matrix with the eigenvector  $\bar{I}_n$  as its  $n$ th column;  $\bar{A}$  and  $\bar{B}$  are the mode coefficient vectors in the forward and backward directions, respectively;  $\bar{\Lambda}(y)$  is a diagonal matrix with  $\exp(-\gamma_n y)$  as its  $n$ th element; namely,

$$\bar{A} = (a_1, a_2, \dots, a_M)^T \quad (63a)$$

$$\bar{B} = (b_1, b_2, \dots, b_M)^T \quad (63b)$$

$$\bar{\Lambda}(y) = \text{diag.} \{e^{-\gamma_1 y}, e^{-\gamma_2 y}, \dots, e^{-\gamma_M y}\} \quad (63c)$$

where the superscript  $T$  represents the transpose of a row vector.

The characteristic impedance matrix can be defined as

$$\bar{Z}_C = \bar{S}_V \cdot \bar{S}_I^{-1} \quad (64)$$

From (62), the mode coefficients  $\bar{A}$  and  $\bar{B}$  can be represented in terms of the line voltages  $\bar{V}(0)$  and line currents  $\bar{I}(0)$  as

$$\bar{A} = \frac{1}{2} [\bar{S}_V^{-1} \cdot \bar{V}(0) + \bar{S}_I^{-1} \cdot \bar{I}(0)] \quad (65a)$$

$$\bar{B} = \frac{1}{2} [\bar{S}_V^{-1} \cdot \bar{V}(0) - \bar{S}_I^{-1} \cdot \bar{I}(0)] \quad (65b)$$

Next, the line voltages  $\bar{V}(l)$  and the line currents  $\bar{I}(l)$  can be expressed in terms of  $\bar{V}(0)$  and  $\bar{I}(0)$  through (65) as

$$\begin{bmatrix} \bar{V}(l) \\ \bar{I}(l) \end{bmatrix} = \begin{bmatrix} \bar{A}_{VV}(l) & \bar{A}_{VI}(l) \\ \bar{A}_{IV}(l) & \bar{A}_{II}(l) \end{bmatrix} \cdot \begin{bmatrix} \bar{V}(0) \\ \bar{I}(0) \end{bmatrix} = \bar{A}(l) \cdot \begin{bmatrix} \bar{V}(0) \\ \bar{I}(0) \end{bmatrix} \quad (66)$$

where  $\bar{A}(l)$  is called the transfer matrix for the uniform transmission lines of length  $l$ ; and the explicit form of the submatrices of  $\bar{A}(l)$  are

$$\bar{A}_{VV}(l) = \frac{1}{2} \bar{S}_V \cdot [\bar{\Lambda}(l) + \bar{\Lambda}(-l)] \cdot \bar{S}_V^{-1} \quad (67a)$$

$$\bar{A}_{VI}(l) = \frac{1}{2} \bar{S}_V \cdot [\bar{\Lambda}(l) - \bar{\Lambda}(-l)] \cdot \bar{S}_I^{-1} \quad (67b)$$

$$\bar{A}_{IV}(l) = \frac{1}{2} \bar{S}_I \cdot [\bar{\Lambda}(l) - \bar{\Lambda}(-l)] \cdot \bar{S}_V^{-1} \quad (67c)$$

$$\bar{A}_{II}(l) = \frac{1}{2} \bar{S}_I \cdot [\bar{\Lambda}(l) + \bar{\Lambda}(-l)] \cdot \bar{S}_I^{-1} \quad (67d)$$

If more than one transmission line section with different characteristics are cascaded, the transfer matrix of each section is multiplied to obtain the overall transfer matrix.

Imposing a voltage source  $\bar{V}_S$  in series with an impedance matrix  $\bar{Z}_S$  at  $y = 0$ , and imposing a voltage source  $\bar{V}_L$  in series with an impedance matrix  $\bar{Z}_L$  at  $y = l$ , we have

$$\bar{V}(0) = \bar{V}_S - \bar{Z}_S \cdot \bar{I}(0) \quad (68a)$$

$$\bar{V}(l) = \bar{V}_L + \bar{Z}_L \cdot \bar{I}(l) \quad (68b)$$

The line voltages at all ports can thus be calculated as

$$\begin{aligned} & \begin{bmatrix} \bar{I} & \bar{A}_{VI}(l) \cdot \bar{Z}_S^{-1} - \bar{A}_{VV}(l) \\ \bar{Z}_L^{-1} & \bar{A}_{II}(l) \cdot \bar{Z}_S^{-1} - \bar{A}_{IV}(l) \end{bmatrix} \cdot \begin{bmatrix} \bar{V}(l) \\ \bar{V}(0) \end{bmatrix} \\ &= \begin{bmatrix} \bar{A}_{VI}(l) \cdot \bar{Z}_S^{-1} \cdot \bar{V}_S \\ \bar{A}_{II}(l) \cdot \bar{Z}_S^{-1} \cdot \bar{V}_S + \bar{Z}_L^{-1} \cdot \bar{V}_L \end{bmatrix} \end{aligned} \quad (69)$$

The transient response can be obtained by using Fourier transform.

For the case of a single microstrip line, we first solve for the capacitance and the inductance per unit length  $C$  and  $L$ , respectively. Next, solving the eigenvalue equations in the lossless medium, we have

$$\gamma^2 = -\beta^2 = -\omega^2 LC \quad (70a)$$

$$I_0 = 1 \quad (70b)$$

$$V_0 = \sqrt{L/C} \quad (70c)$$

The magnetic flux linkage is  $\psi = LI_0 = L$ , the time-average power is  $P_T = (1/2)\sqrt{L/C}$ ; and the conductor loss per unit length can be calculated by (57) and (59), hence we have  $\alpha_C = P_C/2P_T$ . Using (61), we have  $R = 2\alpha_C\sqrt{L/C}$ . The conductance per unit length can be calculated by using (50). With  $L$ ,  $C$ ,  $R$ , and  $G$ , the eigenvalue and the eigenvector can be solved from (44) and (45) as

$$\gamma = \sqrt{(G - i\omega C)(R - i\omega L)} \quad (71a)$$

$$I = 1 \quad (71b)$$

$$V = Z_C I = \sqrt{\frac{R - i\omega L}{G - i\omega C}} \quad (71c)$$

The transfer matrix  $\bar{\bar{A}}(l)$  for a transmission line of length  $l$  can be obtained from (67) as

$$\bar{\bar{A}}(l) = \begin{bmatrix} \cosh \gamma l & -Z_C \sinh \gamma l \\ -Z_C^{-1} \sinh \gamma l & \cosh \gamma l \end{bmatrix} \quad (72)$$

For the case of two symmetric microstrip lines, we first solve the eigenvalue equations in the lossless medium for the even and the odd modes, respectively. Thus we have

$$\gamma_e^2 = -\beta_e^2 = -\omega^2(L_{11} + L_{12})(C_{11} + C_{12}) \quad (73a)$$

$$\bar{I}_{e0} = \begin{bmatrix} 1 \\ 1 \end{bmatrix}, \bar{V}_{e0} = \sqrt{\frac{L_{11} + L_{12}}{C_{11} + C_{12}}} \begin{bmatrix} 1 \\ 1 \end{bmatrix} = \sqrt{\frac{L_{11} + L_{12}}{C_{11} + C_{12}}} \bar{I}_{e0} \quad (73b)$$

$$\gamma_o^2 = -\beta_o^2 = -\omega^2(L_{11} - L_{12})(C_{11} - C_{12}) \quad (73c)$$

$$\bar{I}_{o0} = \begin{bmatrix} 1 \\ -1 \end{bmatrix}, \bar{V}_{o0} = \sqrt{\frac{L_{11} - L_{12}}{C_{11} - C_{12}}} \begin{bmatrix} 1 \\ -1 \end{bmatrix} = \sqrt{\frac{L_{11} - L_{12}}{C_{11} - C_{12}}} \bar{I}_{o0} \quad (73d)$$

The magnetic flux linkage and the time-average power can be calculated as

$$\bar{\psi}_e = \bar{\bar{L}} \cdot \bar{I}_{e0} = (L_{11} + L_{12}) \bar{I}_{e0} \quad (74a)$$

$$P_{eT} = \sqrt{\frac{L_{11} + L_{12}}{C_{11} + C_{12}}} \quad (74b)$$

$$\bar{\psi}_o = \bar{\bar{L}} \cdot \bar{I}_{o0} = (L_{11} - L_{12}) \bar{I}_{o0} \quad (74c)$$

$$P_{oT} = \sqrt{\frac{L_{11} - L_{12}}{C_{11} - C_{12}}} \quad (74d)$$

The conductor loss per unit length can be obtained by using (57) and (59), thus we have

$$\alpha_{eC} = P_{eC}/2P_{eT}, \quad \alpha_{oC} = P_{oC}/2P_{oT} \quad (75)$$

The resistance matrix can be solved from (61) as

$$R_{11} = \alpha_{eC} \sqrt{\frac{L_{11} + L_{12}}{C_{11} + C_{12}}} + \alpha_{oC} \sqrt{\frac{L_{11} - L_{12}}{C_{11} - C_{12}}} \quad (76a)$$

$$R_{12} = \alpha_{eC} \sqrt{\frac{L_{11} + L_{12}}{C_{11} + C_{12}}} - \alpha_{oC} \sqrt{\frac{L_{11} - L_{12}}{C_{11} - C_{12}}} \quad (76b)$$

The conductance matrix per unit length can be calculated by using (50). Substituting these  $\bar{L}$ ,  $\bar{C}$ ,  $\bar{R}$ , and  $\bar{G}$  into (44) and (45), we obtain the eigenvalues and eigenvectors for the even and the odd modes as

$$\gamma_e^2 = (y_{11} + y_{12})(z_{11} + z_{12}) \quad (77a)$$

$$\bar{I}_e = \begin{bmatrix} 1 \\ 1 \end{bmatrix}, \quad \bar{V}_e = Z_e \bar{I}_e \quad (77b)$$

$$\gamma_o^2 = (y_{11} - y_{12})(z_{11} - z_{12}) \quad (77c)$$

$$\bar{I}_o = \begin{bmatrix} 1 \\ -1 \end{bmatrix}, \quad \bar{V}_o = Z_o \bar{I}_o \quad (77d)$$

where

$$Z_e = \sqrt{\frac{z_{11} + z_{12}}{y_{11} + y_{12}}}, \quad Z_o = \sqrt{\frac{z_{11} - z_{12}}{y_{11} - y_{12}}} \quad (78)$$

$$\begin{aligned} y_{11} &= G_{11} - i\omega C_{11}, & y_{12} &= G_{12} - i\omega C_{12} \\ z_{11} &= R_{11} - i\omega L_{11}, & z_{12} &= R_{12} - i\omega L_{12}. \end{aligned} \quad (79)$$

The characteristic impedance matrix can be obtained from (64) as

$$\bar{\bar{Z}}_C = \bar{\bar{S}}_V \cdot \bar{\bar{S}}_I^{-1} = \begin{bmatrix} (Z_e + Z_o)/2 & (Z_e - Z_o)/2 \\ (Z_e - Z_o)/2 & (Z_e + Z_o)/2 \end{bmatrix} \quad (80)$$

The transfer matrix of length  $l$  can be calculated from (67) as

$$\bar{\bar{A}}_{VV}(l) = \frac{1}{2} \begin{bmatrix} \cosh \gamma_e l + \cosh \gamma_o l & \cosh \gamma_e l - \cosh \gamma_o l \\ \cosh \gamma_e l - \cosh \gamma_o l & \cosh \gamma_e l + \cosh \gamma_o l \end{bmatrix} \quad (81a)$$

$$\begin{aligned} \bar{\bar{A}}_{VI}(l) &= \frac{1}{2} \\ &\begin{bmatrix} -Z_e \sinh \gamma_e l - Z_o \sinh \gamma_o l & -Z_e \sinh \gamma_e l + Z_o \sinh \gamma_o l \\ -Z_e \sinh \gamma_e l + Z_o \sinh \gamma_o l & -Z_e \sinh \gamma_e l - Z_o \sinh \gamma_o l \end{bmatrix} \end{aligned} \quad (81b)$$

$$\begin{aligned} \bar{\bar{A}}_{VI}(l) &= \frac{1}{2} \\ &\begin{bmatrix} -Z_e^{-1} \sinh \gamma_e l - Z_o^{-1} \sinh \gamma_o l & -Z_e^{-1} \sinh \gamma_e l + Z_o^{-1} \sinh \gamma_o l \\ -Z_e^{-1} \sinh \gamma_e l + Z_o^{-1} \sinh \gamma_o l & -Z_e^{-1} \sinh \gamma_e l - Z_o^{-1} \sinh \gamma_o l \end{bmatrix} \end{aligned} \quad (81c)$$

$$\bar{\bar{A}}_{II}(l) = \frac{1}{2} \begin{bmatrix} \cosh \gamma_e l + \cosh \gamma_o l & \cosh \gamma_e l - \cosh \gamma_o l \\ \cosh \gamma_e l - \cosh \gamma_o l & \cosh \gamma_e l + \cosh \gamma_o l \end{bmatrix} \quad (81d)$$

In the next section, we demonstrate how the transfer matrix is applied to solve the coupled transmission line problems.

### 3.7 Results and Discussions

First, we check the results of our method in calculating the capacitance matrix using the spectral domain Green's function and compare it with other methods using the spatial domain Green's function. In Tables 3.1 to 3.4, we present the results of capacitance matrix for different microstrip line configurations. In Table 3.1, the difference between our results and those in [9] is about 1% for the self-capacitance, and is about 0.03% for the mutual capacitance. The difference from those in [10] is about 0.1% for the self-capacitance, and about 1% for the mutual capacitance.

In Table 3.2, the difference between our results and those in [9] is less than 0.7% for the self-capacitance, and is less than 4% for the mutual capacitance. The difference between our results and those in [10] is about 0.01% for the self-capacitance, and is less than 0.4% for the mutual capacitance.

The capacitance matrix for two microstrip lines embedded in the same and different layers of a two-layered medium are presented in Tables 3.3 and 4, respectively. The difference between our results and those in [9] is about 3% for the self-capacitance and about 1% for the mutual capacitance.

In Fig. 3.5, we present the charge distributions on the broad sides of a microstrip line with  $t/h = 0.02$  and  $w/h = 0.1, 1.0, 2.0$ . We use 24 pulses on each broad side, and 2 pulses on each narrow side. It is observed that the charge density on the bottom side of the microstrip

Comparison of Capacitance Matrix Elements (F/m).			
element	present work	[9]	[10]
$C_{11}$	$0.6301 \times 10^{-10}$	$0.6233 \times 10^{-10}$	$0.6307 \times 10^{-10}$
$C_{12}$	$-0.5929 \times 10^{-11}$	$-0.5931 \times 10^{-11}$	$-0.5866 \times 10^{-11}$
$C_{22}$	$0.6301 \times 10^{-10}$	$0.6233 \times 10^{-10}$	$0.6307 \times 10^{-10}$

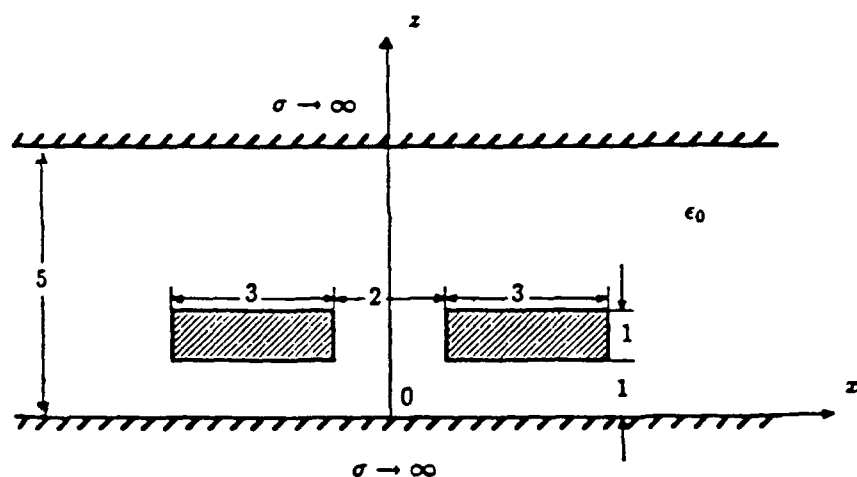


Table 3.1 Comparison of capacitance matrix for two symmetrical strip-lines of finite thickness.

is about an order larger than that on the top side because the electric field between the microstrip and the ground plane is stronger than the electric field above the microstrip. Also, as the width of the microstrip increases, the edge effect becomes less significant.

In Table 3.5, we present the results of resistance calculation for a microstrip line compared with those in [12]. The discrepancy is 7.6% for  $w/h = 0.1$ , and 3.4% for  $w/h = 2.0$ . The calculation of the resistance depends on the square of the charge density distribution which possesses edge effect as shown in Fig. 3.5. Hence, even when two different methods can predict close capacitance results, it is possible that the resistance results can deviate by a higher percentage.

Next, we present the frequency response and the transient response

Comparison of Capacitance Matrix Elements (F/m).			
element	present work	[9]	[10]
$C_{11}$	$0.9225 \times 10^{-10}$	$0.9165 \times 10^{-10}$	$0.9224 \times 10^{-10}$
$C_{12}$	$-0.8539 \times 10^{-11}$	$-0.8220 \times 10^{-11}$	$-0.8504 \times 10^{-11}$
$C_{22}$	$0.9225 \times 10^{-10}$	$0.9165 \times 10^{-10}$	$0.9224 \times 10^{-10}$

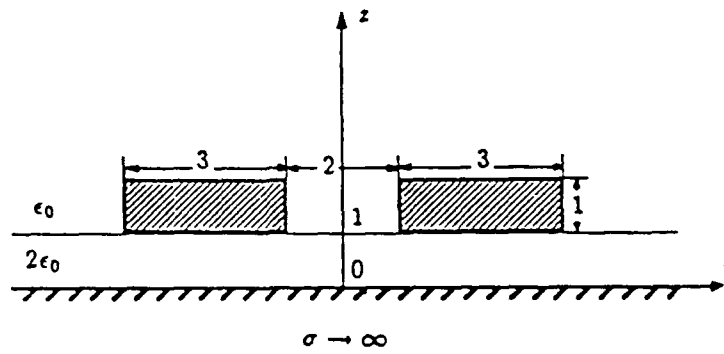


Table 3.2 Comparison of capacitance matrix for two symmetrical microstrip lines of finite thickness.

of two symmetrical microstrip lines. The driving voltage is assumed to have a sinusoidal pulse waveform  $V_1(t)$  with duration  $\tau = 200$  pico seconds as

$$V_1(t) = \begin{cases} (1/2)[1 - \cos(2\pi t/\tau)], & 0 \leq t \leq \tau \\ 0, & \text{elsewhere} \end{cases} \quad (82)$$

The frequency response and the transient response are presented in Fig. 3.6(a) and Fig. 3.6(b), respectively, with all the four load impedances equal to the characteristic impedance of the even mode  $Z_{e0}$ . In Fig. 3.6(a),  $V_1(0)$  is the voltage at  $z = 0$  along line 1,  $V_1(l)$  is the voltage at the receiving port,  $V_2(0)$  is the near-end coupling, and  $V_2(l)$  is the far-end coupling. The increase of  $V_2(l)$  with frequency shows that the high frequency components are responsible for the far-end coupling[16].



Comparison of Capacitance Matrix Elements (F/m).		
element	present work	[9]
$C_{11}$	$0.3827 \times 10^{-10}$	$0.3720 \times 10^{-10}$
$C_{12}$	$-0.6884 \times 10^{-11}$	$-0.6889 \times 10^{-11}$
$C_{22}$	$0.2245 \times 10^{-10}$	$0.2169 \times 10^{-10}$

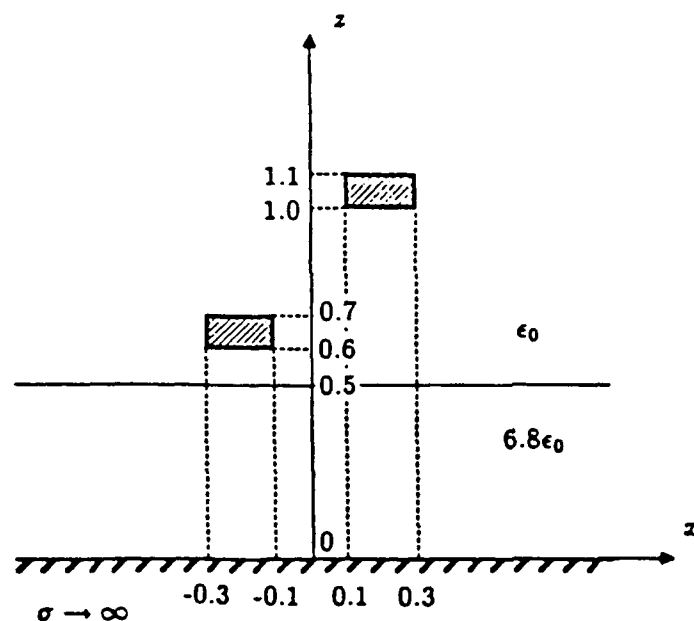


Table 3.3 Comparison of capacitance matrix for two microstrip lines of finite thickness embedded in the same layer of a two-layered medium.

In Fig. 3.6(b), the even and the odd modes propagate in different velocities, and the odd mode propagates faster than the even mode. Hence, the waveform  $V_1(l)$  becomes broader than  $V_1(0)$ , and  $V_2(l)$  shows the split of the odd and the even modes. The waveforms  $V_1(0)$  and  $V_2(0)$  after  $t = 800$  ps are due to the reflections by the load impedances at  $y = l$ . Since the load impedances are chosen to be the same as the characteristic impedance of the even mode, only the odd mode is reflected.

In Fig. 3.7, the transient response is presented with all the four

Comparison of Capacitance Matrix Elements (F/m).		
element	present work	[9]
$C_{11}$	$0.3772 \times 10^{-10}$	$0.3651 \times 10^{-10}$
$C_{12}$	$-0.1583 \times 10^{-11}$	$-0.1562 \times 10^{-11}$
$C_{22}$	$0.2152 \times 10^{-10}$	$0.2099 \times 10^{-10}$

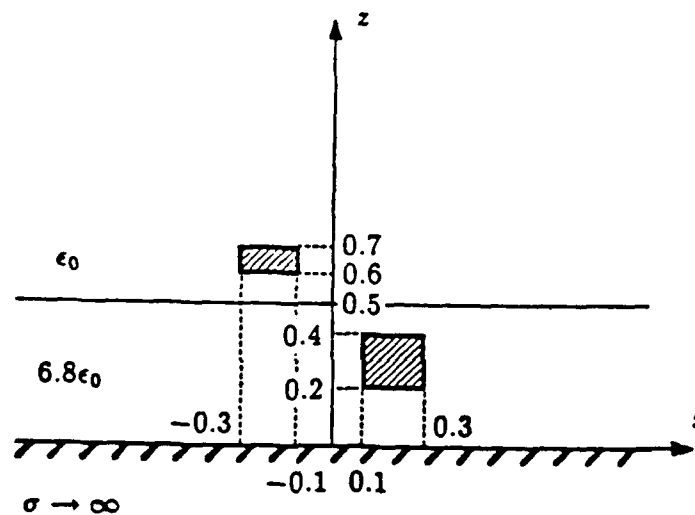


Table 3.4 Comparison of capacitance matrix for two microstrip lines of finite thickness embedded in different layers of a two-layered medium.

load impedances equal to the characteristic impedance of the odd mode  $Z_{oo}$ . The split of the odd and the even modes is observed again. The waveforms  $V_1(0)$  and  $V_2(0)$  after  $t = 800$  ps show that only the even mode is reflected, and the reflected signal arrives later than that in Fig. 3.6(b) because the velocity of the even mode is slower than that of the odd mode.

In Fig. 3.8 and Fig. 3.9, we present the transient responses of two symmetrical microstrip lines with  $s = 0.25$  mm and  $s = 0.375$  mm, respectively. The load impedances are chosen the same as the characteristic impedance of the even mode. Compared with Fig. 3.6(b), it is observed that the coupling signals  $V_2(0)$  and  $V_2(t)$  become weaker

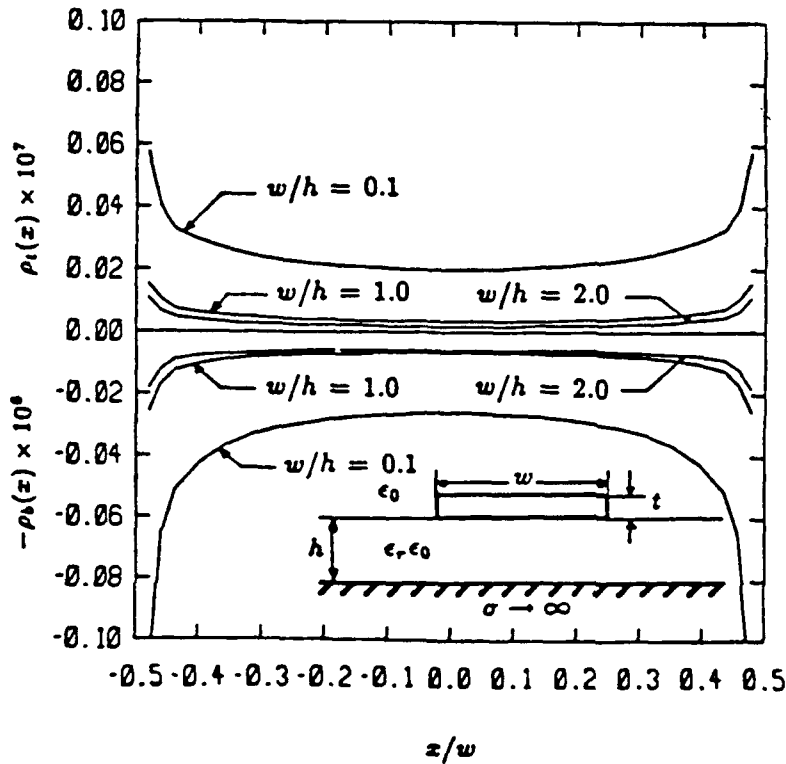


Figure 3.5 The charge distribution on the broad sides of a microstrip line with finite thickness,  $\epsilon_r = 11.7$ ,  $h = 2\text{cm}$ ,  $t/h = 0.02$ , potential on the microstrip surface is 1 volt, 24 pulses per broad side, and 2 pulses per narrow side.

as the separation  $s$  is increased.

In Fig. 3.10, the transient responses with a complex dielectric constant  $\epsilon_r = 10 + i0.1$  are presented. The signal amplitudes are smaller than those in Fig. 3.6(b) due to the dielectric loss. In Fig. 3.11, the transient responses with copper as the conductor material are presented. The surface resistance is assumed to be  $2.61 \times 10^{-7} \sqrt{f}$  ohms. The signal amplitudes are slightly different from those with a perfect conductor because the copper itself is good conductor.

Comparison of Conductor Loss Parameters.				
$w/h$	$R(\Omega/m)$	$R(\Omega/m)$ [12]	$\alpha Z_0 h/R_s$ (dB)	$\alpha Z_0 h/R_s$ (dB) [12]
0.1	0.07125	0.06605	23.713	21.981
0.2	0.04477	0.03993	14.899	13.289
0.3	0.03398	0.02986	11.309	9.937
0.4	0.02795	0.02400	9.303	8.120
0.6	0.02124	0.01848	7.069	6.150
1.0	0.01492	0.01315	4.967	4.376
1.2	0.01308	0.01173	4.353	3.904
1.4	0.01165	0.01063	3.876	3.538
2.0	0.00872	0.00843	2.901	2.807

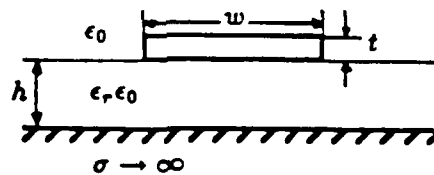


Table 3.5. Comparison of the conductor loss parameters for a microstrip line of finite thickness.

### Conclusions

The spectral domain scalar Green's function in a lossy isotropic stratified medium is derived. A rigorous integral equation formulation for the charge distribution on the surfaces of the microstrip lines with finite thickness embedded in arbitrary layers of an isotropic stratified medium is derived. Using the spectral domain Green's function, a multiconductor transmission line analysis is formulated to investigate the propagation properties of coupled lossy microstrip lines. Both the frequency and the transient responses of coupled lines with different load conditions can be obtained. An efficient algorithm is devised based on this approach.

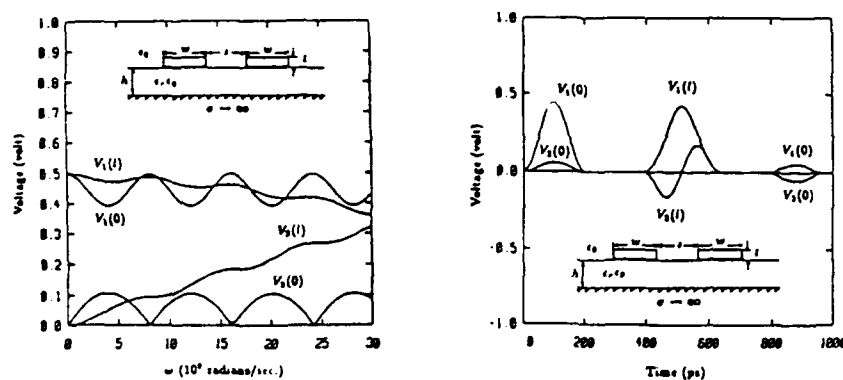


Figure 3.6 Response of two symmetric microstrip lines,  $h = 0.2\text{mm}$ ,  $w = 0.125\text{mm}$ ,  $t = 5\mu\text{m}$ ,  $s = 0.125\text{mm}$ ,  $l = 5\text{cm}$ ,  $\epsilon_r = 10$ , all conductors are perfect,  $Z_1 = Z_2 = Z_3 = Z_4 = Z_{e0} \approx 72.270\Omega$ . (a) Frequency response. (b) Transient response.

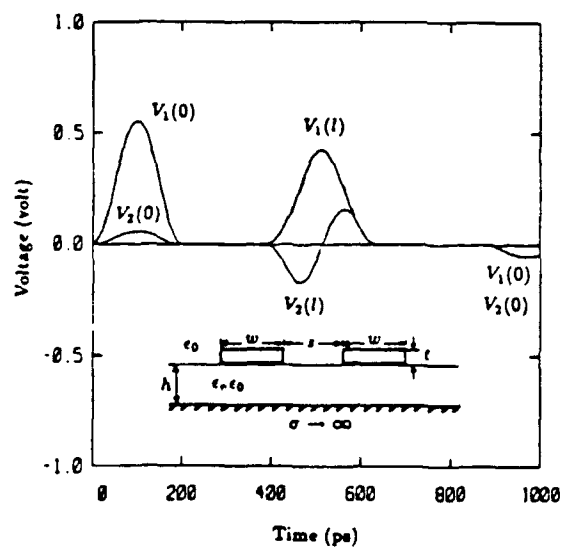


Figure 3.7 Transient response of two symmetric microstrip lines,  $h = 0.2\text{mm}$ ,  $w = 0.125\text{mm}$ ,  $t = 5\mu\text{m}$ ,  $s = 0.125\text{mm}$ ,  $l = 5\text{cm}$ ,  $\epsilon_r = 10$ , all conductors are perfect,  $Z_1 = Z_2 = Z_3 = Z_4 = Z_{e0} \approx 45.862\Omega$ .

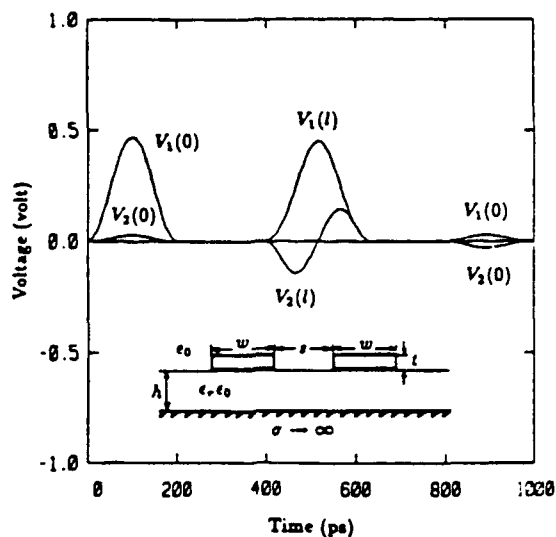


Figure 3.8 Transient response of two symmetric microstrip lines  $h = 0.2\text{mm}$ ,  $w = 0.125\text{mm}$ ,  $t = 5\mu\text{m}$ ,  $s = 0.25\text{mm}$ ,  $l = 5\text{cm}$ ,  $\epsilon_r = 10$ , all conductors are perfect,  $Z_1 = Z_2 = Z_3 = Z_4 = Z_{e0} \approx 66.345\Omega$ .

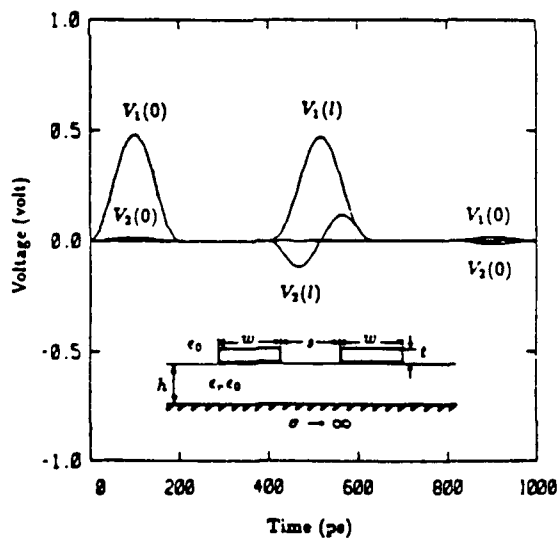


Figure 3.9 Transient response of two symmetric microstrip lines,  $h = 0.2\text{mm}$ ,  $w = 0.125\text{mm}$ ,  $t = 5\mu\text{m}$ ,  $s = 0.375\text{mm}$ ,  $l = 5\text{cm}$ ,  $\epsilon_r = 10$ , all conductors are perfect,  $Z_1 = Z_2 = Z_3 = Z_4 = Z_{e0} \approx 63.567\Omega$ .

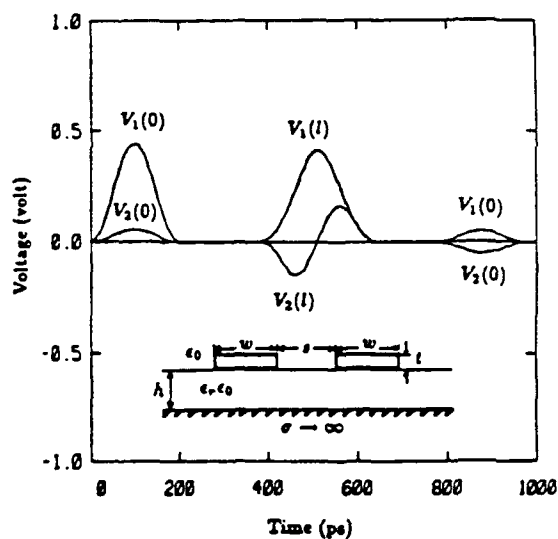


Figure 3.10 Transient response of two symmetric microstrip lines,  $h = 0.2\text{mm}$ ,  $w = 0.125\text{mm}$ ,  $t = 5\mu\text{m}$ ,  $s = 0.125\text{mm}$ ,  $l = 5\text{cm}$ ,  $\epsilon_r = 10 + i0.1$ , all conductors are perfect,  $Z_1 = Z_2 = Z_3 = Z_4 = Z_{e0} \approx 72.270\Omega$ .

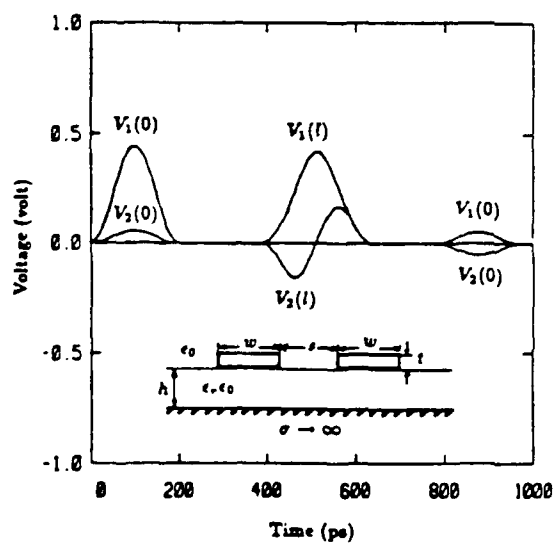


Figure 3.11 Transient response of two symmetric microstrip lines,  $h = 0.2\text{mm}$ ,  $w = 0.125\text{mm}$ ,  $t = 5\mu\text{m}$ ,  $s = 0.125\text{mm}$ ,  $l = 5\text{cm}$ ,  $\epsilon_r = 10$ , all conductors are copper,  $Z_1 = Z_2 = Z_3 = Z_4 = Z_{e0} \approx 72.270\Omega$ .

## References

- [1] Tripathi, V. K., "Asymmetric coupled transmission lines in an inhomogeneous medium," *IEEE Trans. Microwave Theory Tech.*, MTT-23, No. 9, 734-739, September 1975.
- [2] Marx, K. D., "Propagation modes, equivalent circuits, and characteristic terminations for multiconductor transmission lines with inhomogeneous dielectrics," *IEEE Trans. Microwave Theory Tech.*, MTT-21, 450-457, July 1973.
- [3] Djordjevic, A. R., T. K. Sarkar, and R. F. Harrington, "Time-domain response of multiconductor transmission lines," *Proc. IEEE*, No. 6, 743-764, June 1987.
- [4] Seki, S. and H. Hasegawa, "Analysis of crosstalk in very high-speed LSI/VLSI's using a coupled multiconductor MIS microstrip line model," *IEEE Trans. Microwave Theory Tech.*, MTT-32, No. 12, 1715-1720, December 1984.
- [5] Chilo, J. and T. Arnaud, "Coupling effects in the time domain for an interconnecting bus in high-speed GaAs logic circuits," *IEEE Trans. Electron Devices*, ED-31, No. 3, 347-352, March 1984.
- [6] Yuan, H. T., Y. T. Lin, and S. Y. Chiang, "Properties of interconnection on silicon, sapphire, and semi-insulating gallium arsenide substrates," *IEEE J. Solid-State Circuits*, SC-17, No. 2, 269-274, April 1982.
- [7] Medina, F. and M. Horno, "Determination of Green's function matrix for multiconductor and anisotropic multielectric planar transmission lines : a variational approach," *IEEE Trans. Microwave Theory Tech.*, MTT-33, No. 10, 933-940, October 1985.
- [8] Koul, S. K. and B. Bhat, "Generalized analysis of microstrip-like transmission lines and coplanar strips with anisotropic substrates for MIC, electro-optic modulator, and SAW application," *IEEE Trans. Microwave Theory Tech.*, MTT-31, No. 12, 1051-1058, December 1983.
- [9] Wei, C., R. F. Harrington, J. R. Mautz, and T. K. Sarkar, "Multiconductor transmission lines in multilayered dielectric media," *IEEE Trans. Microwave Theory Tech.*, MTT-32, No. 4, 439-449, April 1984.



- [10] Weeks, W. T., "Calculation of coefficients of capacitance of multiconductor transmission lines in the presence of a dielectric interface," *IEEE Trans. Microwave Theory Tech.*, MTT-18, No. 1, 35-43, January 1970.
- [11] Pucel, R. A., D. J. Masse, and C. P. Hartwig, "Losses in microstrip," *IEEE Trans. Microwave Theory Tech.*, MTT-16, No. 6, 342-350, June 1968.
- [12] Harrington, R. F. and C. Wei, "Losses on multiconductor transmission lines in multilayered dielectric media," *IEEE Trans. Microwave Theory Tech.*, MTT-32, No. 7, 705-710, July 1984.
- [13] Syahkal, D. M. and J. B. Davies, "Accurate solution of microstrip and coplanar structures for dispersion and for dielectric and conductor losses," *IEEE Trans. Microwave Theory Tech.*, MTT-27, No. 7, 694-699, July 1979.
- [14] Kong, J. A., *Electromagnetic Waves Theory*, Wiley-Interscience, New York, 1986.
- [15] Ali, S. M., T. M. Habashy, and J. A. Kong, "Dyadic Green's function for anisotropic multilayered media," submitted for publication.
- [16] Fukuoka Y., Q. Zhang, D. P. Neikirk, and T. Itoh, "Analysis of multilayer interconnection lines for a high-speed digital integrated circuit," *IEEE Trans. Microwave Theory Tech.*, MTT-33, No. 6, 527-532, June 1985.

# A Hybrid Method for the Calculation of the Resistance and Inductance of Transmission Lines with Arbitrary Cross Sections

Michael J. Tsuk, *Member, IEEE*, and Jin Au Kong, *Fellow, IEEE*

**Abstract**—The frequency-dependent resistance and inductance of uniform transmission lines are calculated with a hybrid technique that combines a cross-section coupled circuit method with a surface integral equation approach. The coupled circuit approach is most applicable for low-frequency calculations, while the integral equation approach is best for high frequencies. The low-frequency method consists in subdividing the cross section of each conductor into triangular filaments, each with an assumed uniform current distribution. The resistance and mutual inductance between the filaments are calculated, and a matrix is inverted to give the overall resistance and inductance of the conductors. The high-frequency method expresses the resistance and inductance of each conductor in terms of the current at the surface of that conductor and the derivative of that current normal to the surface. A coupled integral equation is then derived to relate these quantities through the diffusion equation inside the conductors and Laplace's equation outside. The method of moments with pulse basis functions is used to solve the integral equations. An interpolation between the results of these two methods gives very good results over the entire frequency range, even when few basis functions are used. Results for a variety of configurations are shown and are compared with experimental data and other numerical techniques.

## I. INTRODUCTION

WITH the ever-increasing speed and density of modern integrated circuits, the need for electromagnetic wave analysis of phenomena such as the propagation of transient signals, especially the distortion of signal pulses, becomes crucial. One of the most important causes of pulse distortion is the frequency dependence of conductor loss, which can be incorporated into circuit models for transmission lines as frequency-dependent resistance and inductance per unit length. Experimental work measuring the resistance and inductance of conductors has concentrated on circular and rectangular cross sections. Kennelly *et al.* [1] did a thorough experimental study,

which was extended to higher frequencies by Kennelly and Affel [2]. Haefner's 1937 paper [3] represents the most extensive experimental data on the resistance of rectangular conductors with a wide variety of width-to-thickness ratios. More recently, Weeks *et al.* [4] did similar work as part of a theoretical treatment of the problem.

In terms of theoretical work, the circular conductor was the first case considered, since it allows an analytical solution. Maxwell [5] examined nonperiodic current; Kelvin [6] solved the periodic case. Carson [7] gave a series solution for the two-wire proximity effect. Cockcroft [8] used the Schwarz-Christoffel transformation to obtain a high-frequency approximation to the skin effect which was expressed in terms of elliptic integrals. Wheeler [9] discussed the "incremental inductance" rule, which is a high-frequency estimate of both the skin and proximity effects. More recently, Casimir and Ubbink [10], [11] presented an overview and summary of the basics of the skin effect, with formulas for the high-frequency limits of simple cases.

In the "filament technique," the conductor (usually rectangular) is divided into a large number of rectangular filaments, which are considered to have uniform current distribution within them. Graneau [12] uses a power-series approach in frequency, which Weeks *et al.* [4] dispensed with. Silvester expands the current in a flat conductor [13] in a series of eigenmodes and the current in a conductor of arbitrary shape [14] in filaments. In both cases he ignores the effect of the placement of the return current, or, in other words, the proximity effect. While these filament methods tend to be very good for low frequencies, since the current density is then almost uniform, they do not model singularities of the current density at high frequencies well.

The other class of methods involves solving the magnetic vector potential integral equation [15]–[21]. The boundary condition is usually on the tangential magnetic field, specified on a closed contour some distance from the conductor. The integral equation is solved by traditional matrix methods, either by expanding the current in a series of orthogonal eigenfunctions [15]–[18] or by dividing the current into subdomain basis functions [19]–[21]. This method is limited in that it requires knowledge of the magnetic field outside the conductor somewhere to

Manuscript received November 21, 1990; revised April 2, 1991. This work was supported by International Business Machines, the Digital Equipment Corporation, RADC under Contract F19628-88-K-0013; the ARO under Contract DAAL03-88-J-0057, the Joint Services Electronics Program under Contract DAAL03-89-C-000, the ONR under Contract N00014-90-J-1002, and the NSF under Grant 8620029-ECS.

M. J. Tsuk is with the Digital Equipment Corporation, Andover, MA 01810.

J. A. Kong is with the Department of Electrical Engineering and Computer Science, Massachusetts Institute of Technology, Cambridge, MA 02139.

IEEE Log Number 9101028.

calculate the current distribution inside but does not give any general way to determine that field. The more recent work of Cangellaris [22] applies the boundary conditions developed in the filament approaches to the magnetic vector potential integral equation, thus removing one of the principal difficulties of that method; however, it still requires modeling of the current throughout the cross section.

In recent years, new methods have been developed which require modeling the current distribution only on the surface of the wires, rather than throughout the cross section. Djordjević *et al.* [23] assumed a nonphysical distribution of current along the propagation direction, which led to an excess resistance at high frequencies. Their work was modified by Wu and Yang [24] to allow appropriate quasi-TEM propagation. However, since both of these methods depend on the calculation of the normal derivative of the current density, they have numerical difficulties at low frequencies, when the current is almost uniform and the normal derivative is small.

The technique presented in this paper is hybrid cross-section coupled circuit/surface integral equation approach. For low frequencies, a filament method based on the work of Weeks *et al.* is used, except with triangular rather than rectangular patches. For high frequencies, a surface integral equation method is used. However, in contrast to previous work, the calculation of resistance and inductance is based on power dissipation and stored magnetic energy, rather than on impedance ratios. It will therefore be more easily extended to structures where nonuniform propagation can occur. In the middle range of frequency, an interpolation is made between the results of the two methods. Since this is a frequency-domain method, we will assume an  $e^{-i\omega t}$  dependence to all quantities.

## II. CROSS-SECTION COUPLED CIRCUIT METHOD

For low frequencies, we use a two-dimensional cross-section coupled circuit method to find the resistance and inductance matrices for multiple transmission lines with uniform cross sections. We assume that these transmission lines consist of signal lines over a common return path or "ground plane." The matrices  $\bar{R}$  and  $\bar{L}$  are defined by

$$\frac{dV}{dz} = (i\omega\bar{L} - \bar{R}) \cdot I \quad (1)$$

where  $V$  is the column vector of the voltage differences between the wires and a reference wire (ground plane or return conductor), and  $I$  is the column vector of currents flowing in the wires.

Here is an overview of the cross-section coupled circuit method. Each conductor is divided into triangular patches and one of the patches from the return conductor is chosen to be the reference. The current is assumed uniform on the cross section of each patch; in other words, a piecewise-constant approximation to the actual current

distribution is used. The resistance and inductance matrices for the patches ( $\bar{r}$  and  $\bar{l}$ ) are then calculated, where these matrices are defined by

$$\frac{dv}{dz} = (i\omega\bar{l} - \bar{r}) \cdot \iota \quad (2)$$

where  $v$  is the column vector of the voltage differences between the patches and the reference patch, and  $\iota$  is the column vector of currents flowing in the  $\hat{z}$  direction through the patches. There are two conditions on the system: first, that the total current in each wire be the sum of the currents in the patches and, second, that the voltage on each patch in a wire be the same, since no transverse currents are allowed under the quasi-TEM assumption. Using these conditions, the matrices for the patches can be reduced to the matrices for the wires.

For the calculation of  $\bar{r}$  and  $\bar{l}$ , we follow [4] quite closely. The elements of the resistance matrix of the patches are

$$r_{jk,jk} = \frac{1}{\sigma A_{jk}} + \frac{1}{\sigma A_{00}} \\ r_{jk,mn} = \frac{1}{\sigma A_{00}}, \quad j \neq m, \quad k \neq n \quad (3)$$

where the first subscript indicates the wire, the second the patch within the wire;  $A_{jk}$  is the cross-sectional area of patch  $k$  on wire  $j$ , and patch 0 on wire 0 is the reference of voltage. Also following [4], the elements of the inductance matrix can be written as the sum of partial inductances:

$$l_{jk,mn} = l_{jk,mn}^{(p)} - l_{jk,00}^{(p)} - l_{00,mn}^{(p)} + l_{00,00}^{(p)} \quad (4)$$

where the partial inductances are given by

$$l_{jk,mn}^{(p)} = -\frac{\mu}{4\pi A_{jk} A_{mn}} \iint dS_{jk} \iint dS'_{mn} \\ \cdot \ln[(x-x')^2 + (y-y')^2] \quad (5)$$

where  $x$  and  $y$  are coordinates on patch  $jk$ , and  $x'$  and  $y'$  are coordinates on patch  $mn$ .

In the Weeks method, the patches over which the integrals in (5) are done are rectangles, and the quadruple integral is done quite easily in closed form. However, it is also possible to evaluate the quadruple integral in closed form for any polygonal shapes; the details are rather complex and are left for the Appendix. We therefore use triangular patches as the most flexible means of modeling conductors with arbitrary cross sections; polygons are covered exactly, and we are able to model quite closely other shapes, such as circles.

Once the resistance and inductance matrices for the patches have been obtained, we proceed in the following manner. Taking

$$\frac{dv}{dz} = [i\omega\bar{l} - \bar{r}] \cdot \iota \equiv -\bar{z} \cdot \iota \quad (6)$$

The matrix  $\bar{z}$  is inverted, and  $\bar{y} = \bar{z}^{-1}$ . Writing out the

elements of the matrix,

$$I_{jk} = - \sum_{m=0}^N \sum_{n=1}^{N_m} y_{jk,mn} \frac{dV_{mn}}{dz} \quad (7)$$

where  $N$  is the number of wires and  $N_m$  is the number of patches on wire  $m$ . The conditions on  $v$  and  $u$  discussed above are applied, to give

$$I_j = - \sum_{m=1}^N Y_{jm} \frac{dV_m}{dz} \quad (8)$$

where  $V$  and  $I$  are the voltage and current column vectors for the wires and where

$$Y_{jm} = \sum_{k=1}^{N_j} \sum_{n=1}^{N_m} y_{jk,mn} \quad (9)$$

Inverting  $\bar{Y}$  gives

$$\bar{Y}^{-1} = \bar{R} - i\omega\bar{L}. \quad (10)$$

Thus, the frequency-dependent resistance and inductance matrices for the wires have been obtained.

In [4], the distribution of patches was a function of frequency; as the frequency increased, the patches were concentrated at the edges, where the current is. However, as shall be shown, it is more efficient to switch to a surface integral equation technique for high frequencies; in this paper the distribution of triangular patches is not altered as the frequency is increased. This has the advantage that, since the resistance and inductance matrices of the patches are independent of frequency,  $\bar{R}$  and  $\bar{L}$  need be calculated only once, no matter for how many frequencies we wish to calculate  $\bar{R}$  and  $\bar{L}$ .

### III. DIFFERENTIAL EQUATIONS AND BOUNDARY CONDITIONS

In this section, the basic equations and boundary conditions which will be used in the surface-integral equation method will be derived. The coordinate system used is shown in Fig. 1. We will rely heavily on quasi-TEM assumptions. First, outside the wires, we assume that the fields are transverse, and that they obey Laplace's equation. In other words, Maxwell's equations outside the wires become

$$\nabla \times H = 0 \quad (11)$$

$$\nabla \cdot H = 0 \quad (12)$$

where  $\nabla$  here is only the transverse operator,  $\hat{x}\partial/\partial x + \hat{y}\partial/\partial y$ . The vector magnetic potential,  $A$ , is defined such that  $\mu H = \nabla \times A$ . By the quasi-TEM assumption,  $J = \hat{z}J_z$  and  $A = \hat{z}A_z$ , and it can be shown that

$$\nabla^2 A_z = 0. \quad (13)$$

Also, inside the conductors, the displacement current is ignored; Maxwell's equations become

$$\nabla \times E = i\omega\mu H \quad (14)$$

$$\nabla \times H = J \quad (15)$$

$$\nabla \cdot H = 0. \quad (16)$$

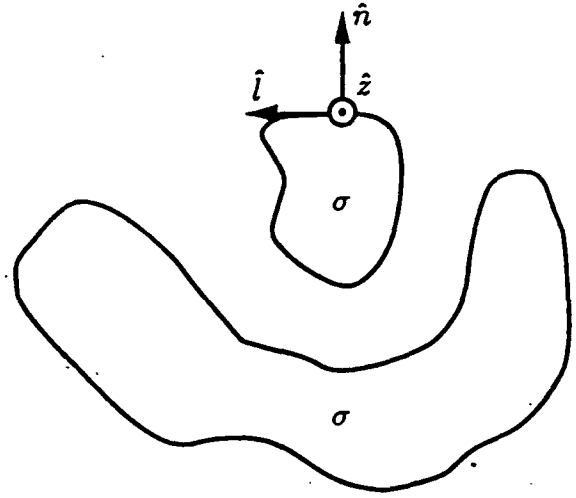


Fig. 1. Coordinate system for surface integral equation method.

Using  $J = \sigma E$ , this reduces to

$$\nabla^2 J_z + i\omega\mu\sigma J_z = 0. \quad (17)$$

There are two boundary conditions at the interface of the conductors and free space: the continuity of tangential  $H$  and of normal  $B = \mu H$ . If  $H$  outside is expressed in terms of  $A_z$ , and  $H$  inside in terms of  $J_z$ , the condition on  $H$  reduces to

$$\frac{\partial J_z}{\partial n} = i\omega\sigma \frac{\partial A_z}{\partial n} \quad (18)$$

which is satisfied along all the conductor-free space interfaces. The boundary condition on normal  $B$  is more difficult. Assuming that all the materials have the same permeability,

$$\frac{\partial J_z}{\partial l} = i\omega\sigma \frac{\partial A_z}{\partial l}. \quad (19)$$

If the derivatives of two quantities along a line are equal, then those quantities must be equal, to within a constant:

$$J_z = i\omega\sigma [A_z - A_q]. \quad (20)$$

$A_q$  is constant over a single conductor, but can vary from conductor to conductor.

Finally, it is necessary to be able to specify the total current flowing on a wire. Using Green's first identity,

$$\iint dS (\phi \nabla^2 \psi + \nabla \phi \cdot \nabla \psi) = \oint dl \phi \frac{\partial \psi}{\partial n} \quad (21)$$

where  $dS$  is a two-dimensional integral over a cross-sectional area, and  $dl$  is a one-dimensional integral along the closed contour bounding that area. Also, the normals are defined as pointing out from the region of interest. With  $\psi = J_z$  and  $\phi = 1$ , and considering (17),

$$I = \iint dS J_z = \frac{i}{\omega\mu\sigma} \iint dS \nabla^2 J_z = \frac{i}{\omega\mu\sigma} \oint dl \frac{\partial J_z}{\partial n} \quad (22)$$

which is an expression for the total current flowing in a

wire in the  $\hat{z}$  direction in terms of quantities on the surface.

#### IV. DETERMINATION OF CIRCUIT PARAMETERS

Eventually, the quantities of interest are the resistance and inductance per unit length of these conductors. It turns out that it is possible to express these quantities in terms of the current and its normal derivative on the surface of the wires. This is useful, because it means that the problem can be formulated in terms of a set of coupled integral equations involving only these surface quantities, allowing a great savings in computation. The resistances and inductances will be derived through power and energy considerations.

For the resistance, consider a case with a current  $I$  flowing in a signal wire and returning in a reference, for example a ground plane. Starting with the power definition of resistance,

$$R = \frac{2P_d}{|I|^2} = \frac{\iint dS E_z J_z^*}{\iint dS J_z J_z^*} = \frac{1}{\sigma} \frac{\iint dS |J_z|^2}{\iint dS J_z J_z^*} \quad (23)$$

where the integration in the numerator is over all wires, while that in the denominator is only over the signal wire. The numerator can be put in a more useful form, using (21) with  $\phi = J_z$  and  $\psi = J_z^*$ , and its complex conjugate, together with (17) to get

$$\begin{aligned} \iint dS |J_z|^2 &= \iint dS J_z J_z^* \\ &= \frac{1}{2} \frac{i}{\omega \mu \sigma} \iint dS [J_z^* \nabla^2 J_z - J_z \nabla^2 J_z^*] \\ &= \frac{1}{2} \frac{i}{\omega \mu \sigma} \oint dl \left[ J_z^* \frac{\partial J_z}{\partial n} - J_z \frac{\partial J_z^*}{\partial n} \right] \\ &= \frac{1}{\omega \mu \sigma} \oint dl \operatorname{Im} \left\{ J_z \frac{\partial J_z^*}{\partial n} \right\}. \end{aligned} \quad (24)$$

Including the total current squared,  $|I|^2$ , from (22),

$$R = \omega \mu \frac{\oint_{\text{all wires}} dl \operatorname{Im} \left\{ J_z \frac{\partial J_z^*}{\partial n} \right\}}{\left| \oint_{\text{signal wire}} dl \frac{\partial J_z}{\partial n} \right|^2}. \quad (25)$$

Similarly, starting with a magnetic stored energy definition of inductance per unit length,  $L$ :

$$L = \frac{4W_m}{|I|^2} = \mu \frac{\iint dS \mathbf{H} \cdot \mathbf{H}^*}{|I|^2} \quad (26)$$

where the range of integration for the numerator is over all space. Using a technique similar to that for (25), combining the contributions from regions inside and out-

side the wires,

$$L = -\mu \frac{\oint_{\text{all wires}} dl \operatorname{Re} \left\{ i \omega \sigma A_z \frac{\partial J_z^*}{\partial n} \right\}}{\left| \oint_{\text{signal wire}} dl \frac{\partial J_z}{\partial n} \right|^2}. \quad (27)$$

The mutual resistance and inductance are calculated from energy considerations, and from the self terms calculated above. If we specify a current  $I_x$  to flow on line  $i$ , and  $-I_x$  to flow on line  $j$ , we can calculate the power dissipated,  $P_d$ , and the stored magnetic energy,  $W_m$ , very easily by the above technique. This gives

$$R_{ij} = \frac{1}{2} (R_{ii} + R_{jj} - 4P_d / I_x^2) \quad (28)$$

and

$$L_{ij} = \frac{1}{2} (L_{ii} + L_{jj} - 8W_m / I_x^2). \quad (29)$$

#### V. DERIVATION OF COUPLED INTEGRAL EQUATIONS

In order to complete the formulation, integral equations are required which relate  $A_z$  to  $\partial A_z / \partial n$  outside the wires and  $J_z$  to  $\partial J_z / \partial n$  inside the wires. Starting from Green's theorem:

$$\iint dS' (\phi \nabla^2 \psi - \psi \nabla^2 \phi) = \oint dl' \left( \phi \frac{\partial \psi}{\partial n'} - \psi \frac{\partial \phi}{\partial n'} \right) \quad (30)$$

where the integral  $dS'$  is over a cross-sectional region, the integral  $dl'$  is over the contour bounding that region, and the normals point out from the region of interest. In general, let  $\Psi(\rho)$  be either  $A_z$  or  $J_z$ , where  $\rho$  is position in the two-dimensional cross section. Since  $\Psi(\rho)$  satisfies  $\nabla^2 \Psi + C\Psi = 0$ , where  $C = 0$  for Laplace's equation and  $C = i\omega\mu\sigma$  for the diffusion equation, a Green's function,  $G(\rho, \rho')$ , can be found which satisfies  $\nabla^2 G + CG = -\delta(\rho - \rho')$ . Substituting  $\Psi$  for  $\psi$  and  $G$  for  $\phi$  in (30),

$$\begin{aligned} \iint dS' \Psi(\rho') \delta(\rho - \rho') \\ = \oint dl' \left[ G(\rho, \rho') \frac{\partial \Psi(\rho')}{\partial n'} - \Psi(\rho') \frac{\partial G(\rho, \rho')}{\partial n'} \right]. \end{aligned} \quad (31)$$

The integral equation will be formulated on the surface, so both  $\rho$  and  $\rho'$  are on the surface. This places  $\delta(\rho - \rho')$  just on the boundary of the  $dS'$  integration, and this must be treated carefully. The most straightforward method is that integrating a delta function that lies on the edge of the range of integration gives  $1/2$ . With this,

$$\begin{aligned} \oint dl' G(l, l') \frac{\partial \Psi(l')}{\partial n'} \\ = \oint dl' \Psi(l') \left[ \frac{\partial G(l, l')}{\partial n'} + \frac{1}{2} \delta(l - l') \right]. \end{aligned} \quad (32)$$

Integral equations for both  $A_z$  and  $J_z$  can now be

obtained. For the outer equation (13),

$$\oint_{\text{all wires}} dl' G_o(l, l') \frac{\partial A_z(l')}{\partial n'} = \oint_{\text{all wires}} dl' A_z(l') \left[ \frac{\partial G_o(l, l')}{\partial n'} - \frac{1}{2} \delta(l - l') \right] \quad (33)$$

where

$$G_o(\rho, \rho') = -\frac{1}{2\pi} \ln \left[ \sqrt{(x - x')^2 + (y - y')^2} \right] \quad (34)$$

and where the sign change in (33) is due to the normals pointing into the region of interest. The range of integration is over the boundary of the free-space region, in other words, over the surface of every wire.

Similarly, for the inner equation (17), for each wire,

$$\oint_{\text{wire } q} dl' G_i(l, l') \frac{\partial J_z(l')}{\partial n'} = \oint_{\text{wire } q} dl' J_z(l') \left[ \frac{\partial G_i(l, l')}{\partial n'} + \frac{1}{2} \delta(l - l') \right] \quad (35)$$

where

$$\begin{aligned} G_i(\rho, \rho') &= \frac{i}{4} H_0^{(1)} \left( e^{i\pi/4} \sqrt{\omega\mu\sigma} \sqrt{(x - x')^2 + (y - y')^2} \right) \\ &= \frac{1}{2\pi} \left[ \ker \sqrt{\omega\mu\sigma} \sqrt{(x - x')^2 + (y - y')^2} \right. \\ &\quad \left. - i \operatorname{kei} \sqrt{\omega\mu\sigma} \sqrt{(x - x')^2 + (y - y')^2} \right] \quad (36) \end{aligned}$$

where "ker" and "kei" are the real and imaginary Kelvin functions. This equation applies to each wire separately; the range of integration is over the surface of that wire.

Using the boundary conditions (18) and (20) to eliminate  $A_z$  from the integral equation for the outside fields and add the condition on the total currents from (22),

$$\oint_{\text{all wires}} dl' G_o(l, l') \frac{\partial J_z(l')}{\partial n'} = \oint_{\text{all wires}} dl' \left[ J_z(l') + i\omega\sigma A_q \right] \left[ \frac{\partial G_o(l, l')}{\partial n'} - \frac{1}{2} \delta(l - l') \right] \quad (37)$$

$$\oint_{\text{wire } q} dl' G_i(l, l') \frac{\partial J_z(l')}{\partial n'} = \oint_{\text{wire } q} dl' J_z(l') \left[ \frac{\partial G_i(l, l')}{\partial n'} + \frac{1}{2} \delta(l - l') \right] \quad (38)$$

$$\oint_{\text{wire } q} dl' \frac{\partial J_z}{\partial n} = -\omega\mu\sigma I_q \quad (39)$$

There is one important thing to note about these integral equations. Contrary to simpler electrostatic problems, the boundary conditions are neither Dirichlet nor Neumann; both  $G$  and  $\partial G/\partial n'$  must be kept in the equations. Because of this, the formulation is in terms of the free-space Green's functions for Laplace's equation

and the diffusion equation, (34) and (36). All information about the boundaries is contained in the paths of integration.

## VI. SOLUTION OF COUPLED INTEGRAL EQUATIONS

We solve these coupled integral equations, (37), (38), and (39), by the method of moments with subdomain basis functions. Expanding the unknown functions  $J_z$  and  $\partial J_z/\partial n$  as the sum of known functions times unknown coefficients,

$$J_z = \sum_m j_m B_m(l) \quad (40)$$

$$\frac{\partial J_z}{\partial n} = \sum_m k_m B_m(l). \quad (41)$$

Simple pulse basis functions are used, normalized so that the integral is unity:

$$B_m(l) = \begin{cases} 1/\Delta_m & \text{if } l_m \leq l \leq l_m + \Delta_m \\ 0 & \text{otherwise.} \end{cases} \quad (42)$$

This gives a piecewise-constant approximation to the surface quantities. The same functions are used for testing, thereby implementing Galerkin's method.

It turns out that, for high frequencies, the current distribution on a wire is similar to the charge distribution on a perfect conductor. For polygonal wires, this means that the current will be concentrated at the corners. Therefore, we find it advantageous to concentrate the basis functions in the same way. For three basis functions on a side, for example, the two in the corners are each one eighth the length of the side; the center one, three quarters. These values were determined empirically, by seeing which division gave results closest to those for a large number of basis functions.

We can thus approximate the coupled integral equation as a matrix equation:

$$\begin{bmatrix} \bar{V}_o & \bar{W}_o & \bar{U}_o \\ \bar{S} & 0 & 0 \\ \bar{V}_i & 0 & \bar{U}_i \end{bmatrix} \begin{bmatrix} K \\ i\omega\sigma A_o \\ J \end{bmatrix} = \begin{bmatrix} 0 \\ -i\omega\mu\sigma I \\ 0 \end{bmatrix} \quad (43)$$

where  $J$  is the vector of the unknown  $j_m$ 's (current),  $K$  is the vector of the unknown  $k_m$ 's (normal derivative of the current), and  $A_o$  is the vector of the  $A_q$ 's (constants of vector potential). The total currents on each wire are specified by the vector  $I$ . The matrices  $\bar{V}_o$ ,  $\bar{W}_o$ ,  $\bar{U}_o$ ,  $\bar{S}$ ,  $\bar{V}_i$ , and  $\bar{U}_i$  arise from integrals of products of the Green's functions with the basis functions and are completely known. The solution of this matrix equation by LU decomposition provides us with an approximation for  $J_z$  and  $\partial J_z/\partial n$ , and through (25) and (27),  $R$  and  $L$ . Since the outer matrices  $\bar{V}_o$ ,  $\bar{W}_o$ , and  $\bar{S}$ , are independent of frequency, they only need to be calculated once. We can make use of this fact by LU-decomposing this part of the large matrix only once, completing the decomposition with the rest of the matrix for each value of frequency. For the pulse basis functions used, the outer matrices can

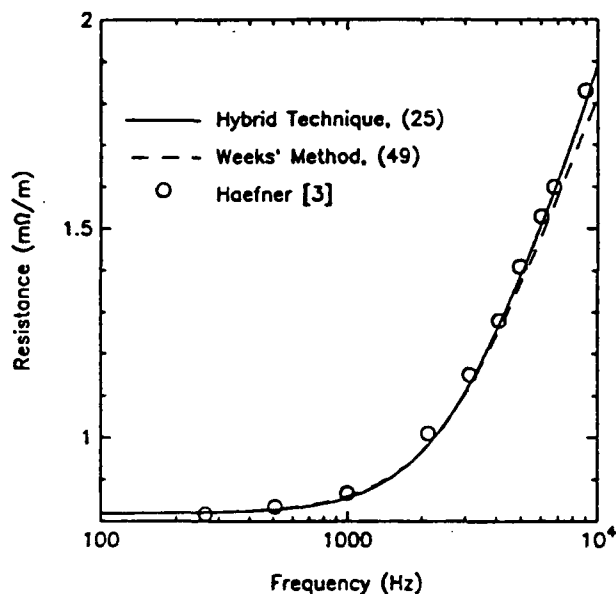


Fig. 2. Resistance of isolated square wire.

be expressed in closed form. The inner matrices,  $\bar{V}_i$  and  $\bar{U}_i$ , have, at worst, double numerical integrals, and for the case of the interaction between elements which lie on the same line, these can be expressed in closed form. Also, at high frequencies, owing to the highly local nature of the diffusion Green's function (36), which results from the rapidly decaying asymptotic nature of the Kelvin functions, only the neighboring patches have an appreciable interaction; those integrals can be calculated quite rapidly.

## VII. RESULTS

In these results, we will compare the hybrid method, described above, with experimental results, as well as with two other methods: the Weeks method [4], which models the current throughout the cross section, and the work of Djordjević *et al.* [23], which models an equivalent current only on the surface over all frequencies. As shall be seen, by using a hybrid method, we can avoid the weaknesses of both of these methods.

First, we consider the example of an isolated square conductor, 4.62 mm on a side, with conductivity  $\sigma = 5.72 \times 10^7 (\Omega \cdot \text{m})^{-1}$ . While the inductance per unit length is undefined, the hybrid method can be used to calculate the resistance per unit length and for comparison with the experimental results of Haefner [3] and the results obtained by using the Weeks method [4]. As can be seen (Fig. 2), the fit for the new method is quite good. In this example, only 12 basis functions (25 unknowns) were used, three on a side. By comparison, the Weeks method with 49 basis functions does not give as good a result.

The next example is that of two parallel circular wires,  $\sigma = 5.84 \times 10^7 (\Omega \cdot \text{m})^{-1}$ . The wires have a diameter of 11.68 mm, and a separation of 0.3 mm and 8 mm for the two cases. Here, the circles were modeled as  $n$ -sided polygons having the same cross-sectional area. In Figs. 3

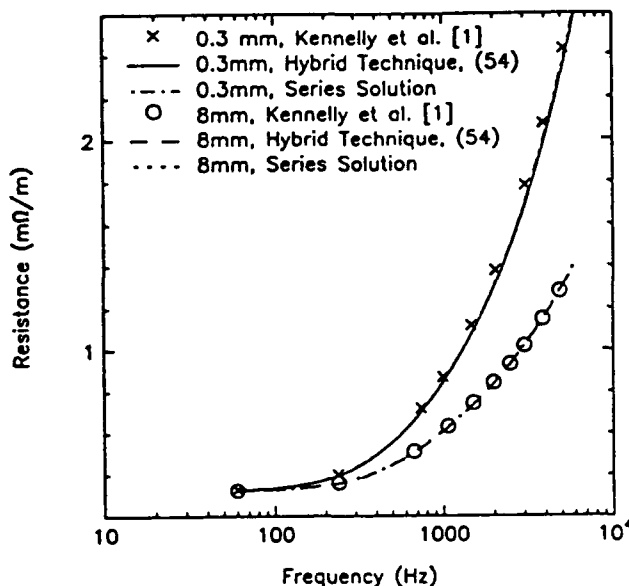


Fig. 3. Resistance of two circular wires.

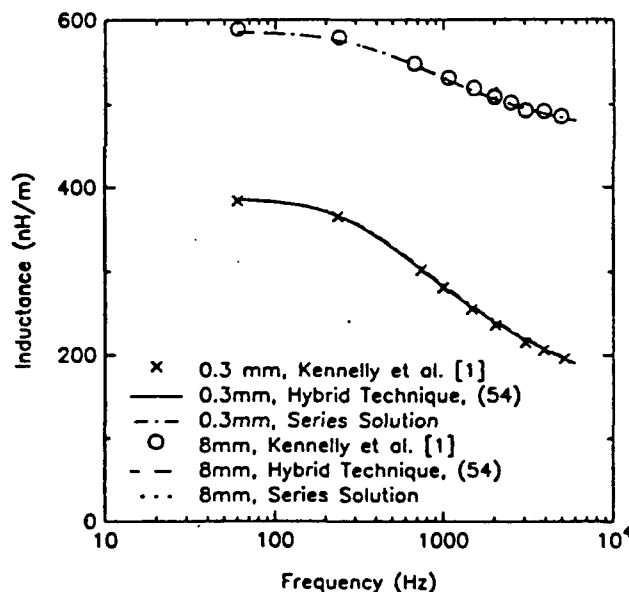


Fig. 4. Inductance of two circular wires.

and 4, the results for 13 basis functions per circle (54 unknowns) are shown, compared with the experimental results of Kennelly *et al.* [1]. The fit is again quite good with the experimental results. Since the Weeks method is limited to rectangular elements, it is not capable of handling this case.

Next, we take the example of two parallel rectangular wires,  $\sigma = 5.6 \times 10^7 (\Omega \cdot \text{m})^{-1}$ ; the configuration is shown in Fig. 5. In Figs. 6 and 7, we compare the hybrid method, the Weeks method, and the results from [23] calculated from a purely surface integral equation approach. It can be seen that the hybrid method agrees with each of the others in its range of validity. Also, the numerical instability of purely surface-integral equation methods in calcu-

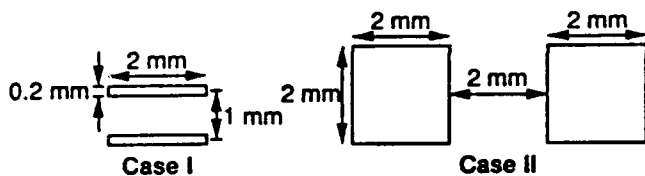


Fig. 5. Two rectangular wires.

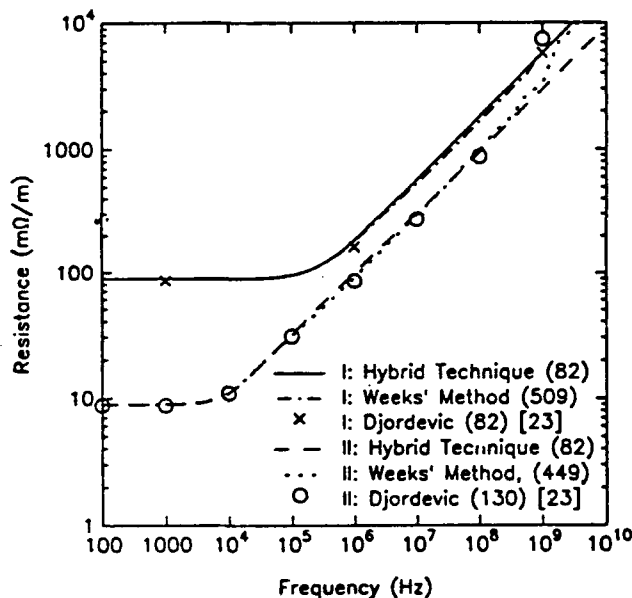


Fig. 6. Resistance of two rectangular wires.

lating the low-frequency inductance can be observed. It is also clear that the hybrid method in general requires fewer basis functions, and thus less computation time, than the Weeks method. In fact, as the frequency increases and the conductors become many skin depths across, even a large number of basis functions in the Weeks method leaves us with a significant error. This is due to the inability of the Weeks method to correctly model the distribution of current along the surface, which is crucial to the calculation of resistance at such frequencies. Tables I and II compare the results of the hybrid method with the Weeks method for the case of two square wires, including CPU times, on a Digital Equipment Corporation VAXstation 3500, running VMS. As can be seen, the cost of the hybrid method in terms of CPU time is much lower than the Weeks method for anything more than a moderate number of basis functions, and especially for high frequencies.

Finally, we consider the case of three rectangular conductors over a ground plane,  $\sigma = 5.81 \times 10^7 \text{ } (\Omega \cdot \text{m})^{-1}$ . The configuration is shown in Fig. 8, the resistance of the first line in Fig. 9, and the self- and mutual inductances in Fig. 10. Since our method is not capable of modeling an infinite ground plane (since imaging is very difficult with an imperfect conductor), a very large conductor was used, 4 mm by 0.5 mm, in its place, with more basis functions concentrated in the area under the signal lines. We compare with the Weeks method and with a purely surface

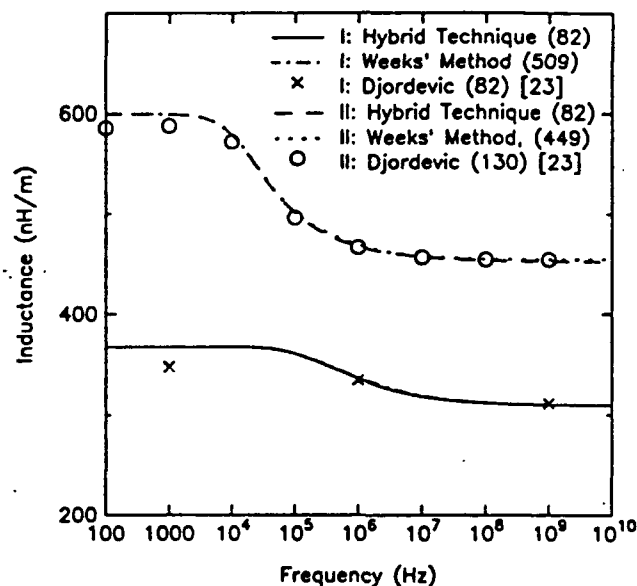


Fig. 7. Inductance of two rectangular wires.

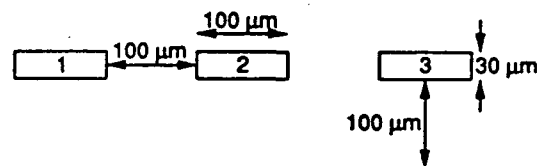


Fig. 8. Three rectangular wires over a ground plane.

integral equation result, both with a large number of basis functions. The same trend can be seen as in the previous case, but there is now a large error in the high-frequency inductance, as predicted by the Weeks method. This is due to the fact that the Weeks method does not model the concentration of the current on the ground plane under the signal lines, since at high frequencies most of the patches are concentrated at the corners of the ground plane, far away from the current. If one improves the Weeks method by restricting the majority of basis functions to be under the signal lines, one gets results which agree with the hybrid method quite closely.

## VIII. CONCLUSIONS

A technique has been developed to calculate the skin effect resistance and inductance of transmission lines with arbitrary cross sections. This technique provides accurate answers over a wide range of frequencies, including the range where neither low-frequency (direct current, uniform distribution) nor high-frequency (skin depth) approximations are valid. The technique is a hybridization of two distinct methods. The first is a cross-section coupled circuit approach, subdividing the wires into triangular patches which are assumed to have uniform current distribution. This method is best for low frequencies, when the physical current has very little variation across the cross section. The second method is in terms of a coupled integral equation, linking the current and its



TABLE I  
RESULTS AND CPU TIMES FOR TWO SQUARE WIRES WITH  
HYBRID METHOD

Basis Functions	Number of Unknowns	Frequency (Hz)	$R$ (m $\Omega$ /m)	$L$ (nH/m)	CPU Time (s)
3×3	50	(Preprocessing)			12.99
		$10^2$	8.929	599.5	1.35
		$10^4$	11.07	577.7	3.36
		$10^6$	94.76	466.6	1.24
7×7	114	(Preprocessing)			19.16
		$10^2$	8.929	599.5	1.37
		$10^4$	11.13	579.6	17.00
		$10^6$	98.54	466.5	6.77
15×15	242	(Preprocessing)			155.79
		$10^2$	8.929	599.5	33.44
		$10^4$	11.15	580.2	156.49
		$10^6$	98.84	466.9	50.06

TABLE II  
RESULTS AND CPU TIMES FOR TWO SQUARE WIRES WITH  
THE WEEKS METHOD

Basis Functions	Number of Unknowns	Frequency (Hz)	$R$ (m $\Omega$ /m)	$L$ (nH/m)	CPU Time (s)
3×3	17	$10^2$	8.929	599.5	0.76
		$10^4$	10.46	586.1	0.76
		$10^6$	118.8	466.9	0.75
7×7	97	$10^2$	8.929	599.5	50.14
		$10^4$	11.10	581.1	49.87
		$10^6$	92.60	468.5	49.43
15×15	449	$10^2$	8.929	599.5	3684.42
		$10^4$	11.22	580.1	3630.31
		$10^6$	91.80	468.1	3639.78

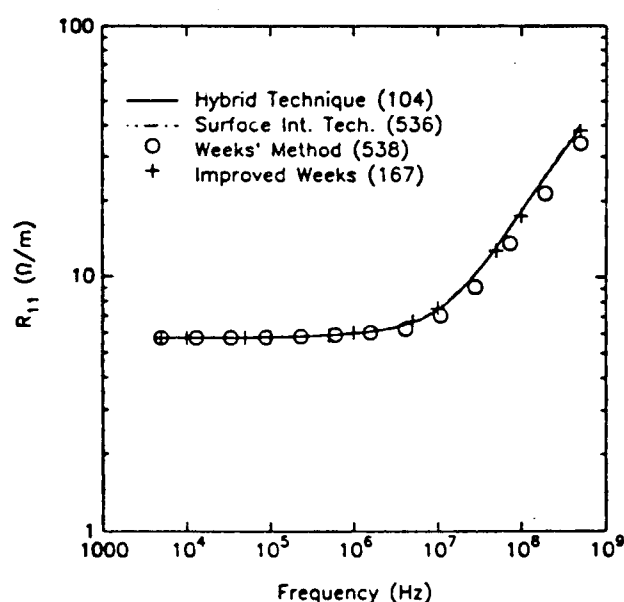


Fig. 9. Resistance of three rectangular wires over a ground plane.

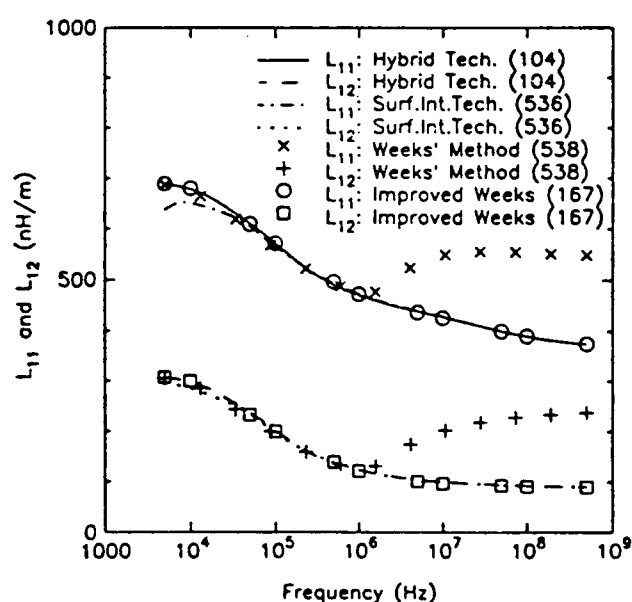


Fig. 10. Self- and mutual inductances of three rectangular wires over a ground plane.

normal derivative on the surface of each wire with the magnetic vector potential and its normal derivative on the same surfaces; the resistance and inductance are both expressed in terms of these surface quantities. This method is best for high frequencies, when the current is almost all confined to the surface, and the diffusion Green's function (eg. (36)) is very localized. For the

middle frequency range, an interpolation between the two results gives very good accuracy with few basis functions. The interpolation function was based on the average size of the conductors, measured in skin depths, and was of the form  $1/(1+0.16a^2/\delta^4)$ , where  $a$  is the average cross section of the conductors, and  $\delta$  is the skin depth. The optimization of the interpolation function is an area of

further research. By choosing triangular patches for the cross-section method and free-space Green's functions for the surface method, a single program is able to handle arbitrary conductors. The method is limited at present to infinite, uniform lines, although nothing theoretically prohibits extension to three-dimensional lines. The theory behind this method is not necessarily limited to configurations with uniform dielectrics, but problems in the definitions of resistance and inductance, stemming from difficulties with the extension of current and especially voltage to non-TEM lines, make such an extension of the method not immediately obvious. For most practical cases, however, the effects of nonuniform dielectrics on the resistance and inductance can be ignored, so that the method presented in this paper will give quick and accurate results.

#### APPENDIX

##### CLOSED-FORM EXPRESSION FOR PARTIAL INDUCTANCES

The problem is to evaluate the integral

$$I = \iint dS_{ij} \iint dS'_{km} \ln t \quad (A1)$$

where  $t \equiv (x - x')^2 + (y - y')^2$  and the areas of integration are the triangular patches ( $ij$ ) and ( $km$ ). Using the fact that  $\ln t = \nabla^2 \nabla'^2 t^2 (\ln t - 3)/64$ , and Green's first identity (21)

$$I = \frac{1}{64} \oint dl_{ij} \oint dl'_{km} \frac{\partial}{\partial n} \frac{\partial}{\partial n'} [t^2 (\ln t - 3)] \quad (A2)$$

where the integrals  $dl_{ij}$  and  $dl'_{km}$  are over the perimeters of patches ( $ij$ ) and ( $km$ ), respectively, and the normals point out from the patches. Using the chain rule,

$$I = \frac{1}{32} \oint dl_{ij} \oint dl'_{km} \left[ \frac{\partial^2 t}{\partial n \partial n'} t \left( \ln t - \frac{5}{2} \right) + \frac{\partial t}{\partial n} \frac{\partial t}{\partial n'} \left( \ln t - \frac{3}{2} \right) \right] \quad (A3)$$

If the patches are polygons, these integrals over the perimeters of the wires become just sums of integrals over pairs of line segments. Therefore, we need to be able to evaluate this integral where the paths of integration are arbitrarily oriented line segments. Without loss of generality, the coordinate system is chosen so that the  $dl$  segment is parallel to the  $x$  axis (Fig. 11). In this case, the various derivatives of  $t$  are

$$t = (u + x_u - x_v - \cos \phi v)^2 + (y_u - y_v - \sin \phi v)^2 \quad (A4)$$

$$\frac{\partial t}{\partial n} = -\frac{\partial t}{\partial y_u} = 2(y_v - y_u + \sin \phi v) \quad (A5)$$

$$\begin{aligned} \frac{\partial t}{\partial n'} &= -\cos \phi \frac{\partial t}{\partial y_v} + \sin \phi \frac{\partial t}{\partial x_v} \\ &= -2[\sin \phi (u - x_v + x_u) + \cos \phi (y_v - y_u)] \end{aligned} \quad (A6)$$

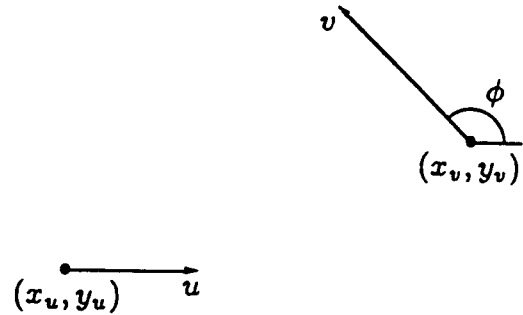


Fig. 11. Coordinate system for mutual inductance of triangular patches.

and

$$\frac{\partial^2 t}{\partial n \partial n'} = -\frac{\partial}{\partial y_u} \left( \frac{\partial t}{\partial n'} \right) = -2 \cos \phi. \quad (A7)$$

Letting  $x \equiv x_v - x_u$  and  $y \equiv y_v - y_u$ , the following double integral over the pair of line segments is obtained:

$$\begin{aligned} f(u, v) &= \frac{1}{32} \int du \int dv t (5 - 2 \ln t) \cos \phi \\ &\quad + (6 - 4 \ln t) (y + v \sin \phi) \\ &\quad \cdot ((u - x) \sin \phi + y \cos \phi) \end{aligned} \quad (A8)$$

where  $t = (u - x - \cos \phi v)^2 + (y + \sin \phi v)^2$ . These integrals can be done in closed form [25]. If the length of the  $dl$  segment is  $a$ , and that of the  $dl'$  segment is  $b$ , the contribution to (A1) from this pair of line segments is  $f(a, b) - f(a, 0) - f(0, b) + f(0, 0)$ . The total is thus the sum of the contributions from each pair of line segments, one from the ( $ij$ ) patch and the other from the ( $km$ ) patch.

#### REFERENCES

- [1] A. E. Kennelly, F. A. Laws, and P. H. Pierce, "Experimental researches on skin effect in conductors," *Trans. AIEE*, vol. 34-II, p. 1953, Sept. 1915.
- [2] A. E. Kennelly and Affel, "Skin-effect resistance measurements of conductors at radio-frequencies up to 100,000 cycles per second," *Proc. IRE*, vol. 4, pp. 523-574, Dec. 1916.
- [3] S. J. Haefner, "Alternating-current resistance of rectangular conductors," *Proc. IRE*, vol. 25, no. 4, pp. 434-447, Apr. 1937.
- [4] W. T. Weeks, L. L. Wu, M. F. McAllister, and A. Singh, "Resistive and inductive skin effect in rectangular conductors," *IBM J. Res. Develop.*, vol. 23, no. 6, pp. 652-660, Nov. 1979.
- [5] J. C. Maxwell, *A Treatise on Electricity and Magnetism*, vol. II, 1873, p. 291.
- [6] W. Thomson, Lord Kelvin, *Mathematical and Physical Papers*, vol. 3, no. 102, pp. 484-515, 1889-1890.
- [7] J. R. Carson, "Wave propagation over parallel wires: the proximity effect," *Phil. Mag.*, vol. 41, no. 24, pp. 607-633, Apr. 1921.
- [8] J. D. Cockcroft, "Skin effect in rectangular conductors at high frequencies," *Proc. Roy. Soc.*, vol. 122, no. A-790, pp. 533-542, Feb. 1929.
- [9] H. A. Wheeler, "Formulas for the skin-effect," *Proc. IRE*, vol. 30, pp. 412-424, Sept. 1942.
- [10] H. B. G. Casimir and J. Ubbink, "The skin effect, I. Introduction; the current distribution for various configurations," *Philips Tech. Rev.*, vol. 28, no. 9, pp. 271-283, 1967.
- [11] H. B. G. Casimir and J. Ubbink, "The skin effect, II. The skin effect at high frequencies," *Philips Tech. Rev.*, vol. 28, no. 10, pp. 300-315, 1967.
- [12] P. Graneau, "Alternating and transient conduction currents in straight conductors of any cross-section," *Int. J. Electron.*, vol. 19, pp. 41-59, 1965.

- [13] P. Silvester, "Modal network theory of skin effect in flat conductors," *Proc. IEEE*, vol. 54, no. 9, pp. 1147-1151, Sept. 1966.
- [14] P. Silvester, "The accurate calculation of skin effect of complicated shape," *IEEE Trans. Power App. Syst.*, vol. PAS-87, pp. 735-742, Mar. 1968.
- [15] A. Timotin, "Iteration method for study of the skin-effect in straight conductors," *Rev. Roum. Sci. Tech., Ser. Electrotech. Energ.*, vol. 10, no. 1, pp. 19-45, 1965.
- [16] B. D. Popović and Z. D. Popović, "Method of determining power-frequency current distribution in cylindrical conductors," *Proc. Inst. Elec. Eng.*, vol. 119, no. 5, pp. 569-574, May 1972.
- [17] P. Waldow and I. Wolff, "The skin-effect at high frequencies," *IEEE Trans. Microwave Theory Tech.*, vol. MTT-33, pp. 1076-1082, Oct. 1985.
- [18] P. Waldow and I. Wolff, "Dual bounds variational formulation of skin effect problems," in *IEEE MTT-S Int. Microwave Symp. Dig.*, 1987, pp. 333-336.
- [19] A. Konrad, "Integrodifferential finite element formulation of two-dimensional steady-state skin effect problems," *IEEE Trans. Magn.*, vol. MAG-18, pp. 284-292, Jan. 1982.
- [20] G. Costache, "Finite-element solution of steady-state skin-effect problems in straight flat conductors," *COMPEL-Int. J. Comput. and Math. in Elec. and Electron. Eng.*, vol. 2, no. 2, pp. 35-39, 1983.
- [21] G. Costache, "Finite element method applied to skin-effect problems in strip transmission lines," *IEEE Trans. Microwave Theory Tech.*, vol. MTT-35, pp. 1009-1013, Nov. 1987.
- [22] A. C. Cangellaris, "The importance of skin-effect in microstrip lines at high frequencies," in *IEEE MTT-S Int. Microwave Symp. Dig.*, 1988, pp. 197-198.
- [23] A. R. Djordjević, T. K. Sarkar, and S. M. Rao, "Analysis of finite conductivity cylindrical conductors excited by axially-independent TM electromagnetic field," *IEEE Trans. Microwave Theory Tech.*, vol. MTT-33, pp. 961-966, Oct. 1985.
- [24] R.-B. Wu and J.-C. Yang, "Boundary integral equation formulation of skin effect problems in multiconductor transmission lines," *IEEE Trans. Magn.*, vol. MAG-25, pp. 3013-3015, July 1989.
- [25] M. J. Tsuk, "Propagation and interference in lossy microelectronic integrated circuits," Ph. D. thesis, Department of Electrical Engineering and Computer Science, Massachusetts Institute of Technology, June 1990.



Michael J. Tsuk

He received the S.B., S.M., and Ph.D. degrees in electrical engineering from the Massachusetts Institute of Technology in 1984, 1986, and 1990, respectively.

Since 1990, he has been with the Physical Technology Group of the Digital Equipment Corporation, Andover, MA. He is an Assistant Editor for the *Journal of Electromagnetic Waves and Applications (JEWA)*. His research interests include time-domain electromagnetics and numerical methods for the design of high-performance integrated circuit packaging.



Jin Au Kong (S'65-M'69-SM'74-F'85) is Professor of Electrical Engineering and Chairman of Area IV and Energy and Electromagnetic Systems in the Department of Electrical Engineering and Computer Science at the Massachusetts Institute of Technology, Cambridge, MA. From 1977 to 1980 he served the United Nations as a High-Level Consultant to the Under-Secretary-General on Science and Technology, and as an Interregional Advisor on remote sensing technology for the Department of Technical Cooperation for Development. His research interests are in the area of electromagnetic wave theory and applications. He has published six books and more than 300 refereed journal and conference papers and has supervised more than 100 theses.

Dr. Kong is the Editor for the Wiley series on remote sensing, the Editor-in-chief of the *Journal of Electromagnetic Waves and Applications (JEWA)*, and the Chief Editor for the Elsevier book series on Progress in Electromagnetics Research (PIER).

Office of Naval Research

DISTRIBUTION LIST

Arthur K. Jordan  
Scientific Officer

3 copies

Code:1114SE  
Office of Naval Research  
800 North Quincy Street  
Arlington, VA 22217

Administrative Contracting Officer  
E19-628  
Massachusetts Institute of Technology  
Cambridge, MA 02139

1 copy

Director  
Naval Research Laboratory  
Washington, DC 20375  
Attn: Code 2627

1 copy

Defense Technical Information Center  
Bldg. 5, Cameron Station  
Alexandria, VA 22314

2 copies